CONF-9505204--
ORNL/FMP-95/1

U.S. Department of Energy
Fossil Energy
Advanced Research and Technology Development

Proceedings of the Ninth Annual Conference On Fossil Energy Materials

May 16-18, 1995
Oak Ridge, Tennessee

Fossil Energy AR&TD Materials Program

OAK RIDGE NATIONAL LABORATORY
MANAGED BY
LOCKHEED MARTIN ENERGY SYSTEMS, INC.
FOR THE
U.S. DEPARTMENT OF ENERGY
UNDER CONTRACT DE-AC05-84OR21400

Fossil Energy Program

CONF-9505204--
ORNL/FMP-95/1

U.S. Department of Energy
Fossil Energy
Advanced Research and Technology Development

Proceedings of the Ninth Annual Conference On Fossil Energy Materials

May 16-18, 1995
Oak Ridge, Tennessee

Fossil Energy AR&TD Materials Program

OAK RIDGE NATIONAL LABORATORY
MANAGED BY
LOCKHEED MARTIN ENERGY SYSTEMS, INC.
FOR THE
U.S. DEPARTMENT OF ENERGY
UNDER CONTRACT DE-AC05-84OR21400

Fossil Energy Program

CONF-9505204
ORNL/FMP-95/1

PROCEEDINGS OF THE NINTH ANNUAL CONFERENCE ON FOSSIL ENERGY MATERIALS

May 16-18, 1995
Oak Ridge, Tennessee

Compiled by
N. C. Cole and R. R. Judkins

Date Published: August 1995

Prepared by the
Department of Energy
Fossil Energy Office of Advanced Research
and
Oak Ridge Operations Office
AA 15 10 10 0

Prepared by the
OAK RIDGE NATIONAL LABORATORY
Oak Ridge, Tennessee 37831-6285
managed by
LOCKHEED MARTIN ENERGY SYSTEMS, INC.
for the
U.S. DEPARTMENT OF ENERGY
under Contract DE-AC05-84OR21400

PREFACE

The Ninth Annual Conference on Fossil Energy Materials was held in Oak Ridge, Tennessee, on May 16-18, 1995. The meeting was sponsored by the U.S. Department of Energy's (DOE) Office of Fossil Energy through the Advanced Research and Technology Development (AR&TD) Materials Program. The objective of the AR&TD Materials Program is to conduct research and development on materials for longer-term fossil energy applications as well as for generic needs of various fossil fuel technologies. The management of the program has been decentralized to the DOE Oak Ridge Operations Office with Oak Ridge National Laboratory (ORNL) as the technical support contractor. The research is performed by staff members at ORNL and by researchers at other national laboratories, universities, and in private industry. The work is divided into the following categories: (1) structural ceramics, (2) new alloys and coatings, (3) functional materials, and (4) technology assessment and transfer.

This conference is held each year to review the work on all of the projects of the Program. The final program for the meeting is given in Appendix A, and a list of attendees is presented in Appendix B.

These proceedings have been published from camera-ready masters supplied by the authors. All of the contributions have been checked for errors but have not been subjected to peer reviews. However, most of the papers have already undergone technical review within the individual organizations before submission to the Program Office.

The successful completion of the conference and publication of the proceedings has required help from several people. The organizers wish to thank Judy Fair for her superb coordination work; Gloria Donaldson for her assistance with preparations for the conference; Judy and Gloria for their excellent work at the registration desk; the ORNL Conference Office for their help in the many arrangements; and the numerous staff and support personnel associated with the conference. Finally, we express our sincere appreciation to the authors whose efforts are the very basis of the conference.

SESSION I - CERAMIC COMPOSITES

TABLE OF CONTENTS

PREFACE iii

SESSION I - CERAMIC COMPOSITES

Oxidation-Resistant Interfacial Coatings for Continuous Fiber Ceramic Composites
D. P. Stinton, T. M. Besmann and A. Bleir 1

Modeling of Fibrous Preforms for CVI Fabrication
T. L. Starr and D. Y. Chiang 13

Engineering-Scale Development of the Vapor-Liquid-Solid (VLS) Process for the Production of Silicon Carbide Fibrils and Linear Fibril Assemblies
M. A. Tenhover and J. J. Biernacki 19

Mechanical Properties of Ceramic Composite Tubes
W. A. Curtin, L. L. Olesksuk K. L. Reifsnider and D. P. Stinton 31

Joining of SiC Ceramics and SiC/SiC Composites
B. H. Rabin 41

Comparison of High Temperature Mechanical Properties of Two Monolithic SiC Ceramics and an Al_2O_3 SiC Composite
K. Breder 45

Factors Effecting the Corrosion Rates of Ceramics in Coal Combustion Systems
J. P. Hurley 57

Corrosion Performance of Materials for Advanced Combustion Systems
K. Natesan, M. Freeman and M. Mathur 71

Mullite Coatings for Corrosion Protection of Silicon Carbide
R. Mulpuri and V. Sarin 85

Mechanical Behavior of Ceramic Composite Hot-Gas Filters After Exposure to Severe Environments
D. J. Pysher, B. L. Weaver, R. G. Smith, J. H. Eaton, and J. L. Kahnke 97

Fracture Behavior of Advanced Ceramic Hot-Gas Filters
J. P. Singh, D. Singh, J. Smith and H. Volz 107

High Temperature Corrosion of Advanced Ceramics Material for Hot-Gas Filters and Heat Exchangers
E. R. Kupp, M. F. Trubelja, K. E. Spear and R. E. Tressler 117

Thermal and Structural Analysis of a Filter Vessel Ceramic Tubesheet
R. H. Mallett, R. W. Swindeman and J. F. Zievers 127

Processing of Silicon Nitride and Alumina Nanosize Powders
E. J. Gonzalez, G. Piermarini, B. Hockey and S. G. Malghan 133

SESSION II - CERAMICS AND NEW ALLOYS

Development of Nondestructive Evaluation Methods and Prediction of Effects of Flaws on the Fracture Behavior of Structural Ceramics
W. A. Ellingson. J. P. Singh, E. A. Sivers, J. B. Stuckey, D. Christopher, S. L. Dieckman and D. Singh 145

Fabrication of Fiber-Reinforced Composites by Chemical Vapor Infiltration
W. M. Matlin, D. P. Stinton and T. M. Besmann 157

Transport Properties of Ceramic Composites
T. L. Starr 167

Development of Materials for Microwave-Heated Diesel Particulate Filter
M. A. Janney and D. P. Stinton 175

High Temperature Inorganic Membranes for Separating Hydrogen
D. E. Fain and G. E. Roettger 185

Mixed Oxygen Ion/Electron-Conducting Ceramics for Oxygen Separation
J. W. Stevenson, B. L. Armstrong, T. R. Armstrong, J. L. Bates, L. R. Pederson and W. J. Weber 195

Proton Conducting Cerate Ceramics
G. W. Coffey, L. R. Pederson, T. R. Srmstrong, J. L. Bates and W. J. Weber . . . 205

Synthesis of Silicon Nitride Powders in Pulsed Rf Plasmas
R. J. Buss, S. V. Babu and P. Ho 215

Mechanically Reliable Surface Oxides for High-Temperature Corrosion Resistance
K. Natesan, B. W. Veal, M. Grimsditch, D. Renusch and A. P. Paulikas 225

Plasma Synthesis of Aluminia Films on Metal and Ceramic Substrates
I. Brown and Z. Wang 239

Mechanically Reliable Scales and Coatings
P. F. Tortorelli and K. B. Alexander 247

Welding and Mechanical Properties of Cast FAPY (Fe-16 at. % Al-Based) Alloy Slabs
V. K. Sikka, G. M. Goodwin, D. J. Alexander and C. R. Howell 257

The Influence of Processing on Microstructure and Properties of Iron Aluminides
R. N. Wright and J. K. Wright 271

Weld Overlay Cladding with Iron Aluminides
G. M. Goodwin 281

High-Temperature Corrosion Behavior of Iron-Aluminide Alloys and Coatings
P. F. Tortorelli, J. H. DeVan, B. A. Pint and I. G. Wright 289

Effect of Surface Condition on the Aqueous Corrosion Behavior of Iron Aluminides
R. A. Buchanan and R. L. Perrin 301

Pack Cementation Cr-Al Coating of Steels and Ge-Doped Silicide Coating of Cr-Nb alloy,
Y. R. He, M. H. Zheng and R. A. Rapp 311

Microstructure Characterization and Weldability Evaluation of the Weld Heat Affected Zone (HAZ) in 310 HCbN Tubing
C. D. Lundin and C. Y. P. Qiao 325

The Effects of Microstructural Control on the Mechanical Behavior of Cr_2Nb-Based Alloys
J. A. Cook, P. K. Liaw and C. T. Liu 335

SESSION III - WORKSHOP ON MATERIALS CHALLENGES IN ADVANCED FOSSIL FUELED POWER SYSTEMS

SESSION IV - NEW ALLOYS AND FUNCTIONAL MATERIALS

ODS Iron Aluminides
I. G. Wright, C. G. McKamey and B. A. Pint 355

Effect of Composition and Heat Treatment at 1150°C on Creep-Rupture Properties of Fe_3Al-Based Alloys
C. G. McKamey, P. J. Maziasz and Y. Marrero-Santos 369

Environmental Embrittlement of Iron Aluminides Under Cyclic Loading Conditions
A. Castagna, D. A. Alven and N. S. Stoloff 377

The Effect of Alloying and Grain Refinement on the Room-Temperature Ductility of of As-Cast Fe_3Al-Based Alloys
S. Viswanathan, C. G. McKamey and P. J. Maziasz 387

Weldability of Polycrystalline Aluminides
A. A. Fasching, G. R. Edwards, R. P. Burt and S. A. David 397

Electro-Spark Deposited Coatings for Protection of Materials
R. N. Johnson 407

Cr_2 Nb-Based Alloy Development
C. T. Liu, P. F. Tortorelli, J. A. Horton, D. S. Easton, J. H. Schneibel, L. Heatherly, C. A. Carmichael, M. Howell and J. L. Wright 415

Investigation of Austenitic Alloys for Advanced Heat Recovery and Hot-Gas Cleanup Systems
R. W. Swindeman and W. Ren 427

Fireside Corrosion Testing of Candidate Superheater Tube Alloys, Coatings, and Claddings - Phase II
J. B. Blough, M. T. Krawchuk and S. F. Van Weele 435

A Novel Carbon Fiber-Based Porous Carbon Monolith
T. D. Burchell, J. W. Klett and C. E. Weaver 447

Carbon-Fiber Composite Molecular Sieves for Gas Separation
M. Jagtoyen, F. Derbyshire, G. Kimber and Y. Q. Fei 457

Stability of Solid Oxide Fuel Cell Materials
T. R. Armstrong, L. R. Pederson, J. W. Stevenson and P. E. Raney 467

Ceramic Catalyst Materials
A. G. Sault and T. J. Gardner 477

APPENDIX A. FINAL PROGRAM FOR THE NINTH ANNUAL CONFERENCE ON FOSSIL ENERGY MATERIALS 489

APPENDIX B. LIST OF ATTENDEES 495

OXIDATION-RESISTANT INTERFACIAL COATINGS FOR CONTINUOUS FIBER CERAMIC COMPOSITES

D. P. Stinton, T. M. Besmann and A. Bleier
Oak Ridge National Laboratory, Oak Ridge, TN 37831-6063

S. Shanmugham and P. K. Liaw
University of Tennessee, Knoxville, TN 37996-2200

ABSTRACT

Continuous fiber ceramic composites mechanical behavior are influenced by the bonding characteristics between the fiber and the matrix. Finite modeling studies suggest that a low-modulus interfacial coating material will be effective in reducing the residual thermal stresses that are generated upon cooling from processing temperatures. Nicalon^{TM}/SiC composites with carbon, alumina and mullite interfacial coatings were fabricated with the SiC matrix deposited using a forced-flow, thermal gradient chemical vapor infiltration process. Composites with mullite interfacial coatings exhibited considerable fiber pull-out even after oxidation and have potential as a composite system

INTRODUCTION

Continuous fiber ceramic composites (CFCCs) are being developed for high temperature structural applications, many of which are in oxidative environments.[1,2] Such composites are attractive since they are light-weight and possess the desired mechanical properties at elevated temperature and in aggressive environments. The most significant advantage is their toughness and their non-catastrophic failure behavior.[3,4]

The mechanical properties of CFCCs have been characteristically linked with the nature of the interfacial bond between the fibers and the matrix.[5,6] Weakly bonded fiber-matrix interfaces allow an impinging matrix crack to be deflected such that the fracture process occurs through several stages: Crack deflection, debonding at the interface, fiber slip and pull-out, and ultimately fiber failure.[7] Such a composite will fail in a graceful manner and exhibit substantial fracture toughness. Currently, carbon interface coatings

are used to appropriately tailor interface properties, however their poor oxidation resistance has required a search of an appropriate replacment.

Generally, metal oxides are inherently stable to oxidation and possess thermal expansion coefficients relatively close to those of Nicalon^{TM} (Ceramic Grade Nicalon, Nippon Carbon Company, Tokyo, Japan) nd SiC. However, the metal oxides must also be chemically compatible with the fiber and matrix. If the fiber/interface/matrix system is chemically compatible, then the interfacial bonding stress is influenced by the thermal residual stresses that are generated as the composite is cooled from processing to room temperature. In the current work, thermomechanical computational results were obtained from a finite element model (FEM) for calculating the thermal residual stresses.[8] This was followed by experimental evaluation of Nicalon^{TM}/SiC composites with carbon, alumina, and mullite interfacial coatings.

DISCUSSION OF CURRENT ACTIVITIES

Finite Element Modeling

A finite element model has been developed in order to understand the effect of interfacial coating materials on the profile of thermal residual stresses. The elementary cell comprises a fiber (radius =7 μm) surrounded by an interfacial coating, the matrix (radius = 11 μm) and the bulk material (Fig. 1). The bulk material is represented as having the average properties of the composite determined from the rule of mixtures. The fiber volume fraction is 40% and the interfacial and the matrix volume fraction varies with interfacial coating thickness.

The model is based on an axisymmetric system and the meshing was done with two dimensional elements (rectangular with eight nodes) in a plane. The boundary conditions are the following: 1. Displacement is permissible only along the axis of

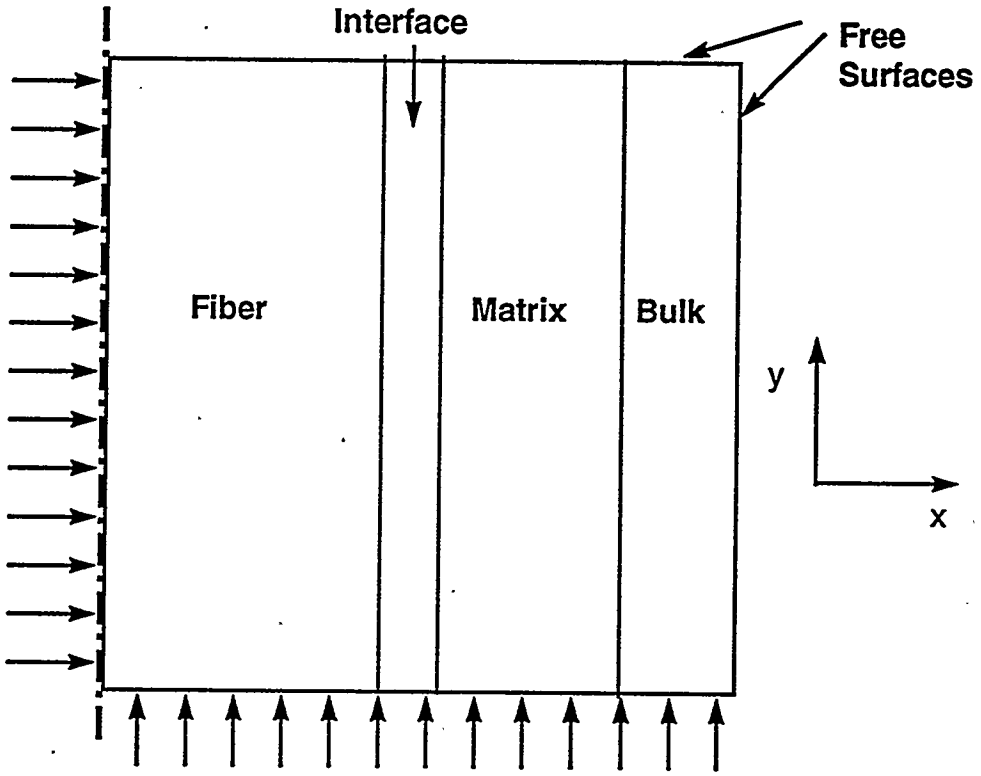

Fig. 1 Schematic of an elementary cell in the finite element model

symmetry, 2. the bottom of the cell can not be displaced in the direction of the axis of symmetry and the bulk cannot rotate around this axis and has its outer surface free, and 3. a temperature differential of 1175 K is assumed due to cooling from the maximum processing temperature of 1473 K.

A variety of potential interfacial coating materials (carbon, aluminum titanate, barium zirconium phospate silicate or BaZPS, alumina and mullite) which represent a wide range of mechanical properties (Young's modulus, coefficient of thermal expansion, and Poisson's ratio) were considered. The properties of Nicalon^{TM}, SiC matrix, and the interfacial coating materials are summarized in Table 1. The finite element model was used to compute the effect of carbon coating thickness on the radial thermal residual stresses (σ_x) at the fiber-coating interface and the coating-matrix interface (Fig. 2). The residual radi-

al stress for the fiber-matrix interface in the absence of any coating is based on Hsueh's[10] model. With a thin coating (0.1 μm), the residual radial stresses at both of the interfaces are compressive, although they become tensile with increasing coating thickness. The effect of alternative coating materials with a thickness of 0.5 μm on the radial stresses developed at the interfaces are shown in Fig. 3 and compared with that for 0.1 μm carbon.

Table 1. Material properties utilized in the FEM analysis [9]

Material	Young's modulus E (GPa)			Coefficient of thermal expansion ($\times 10^{-6}$/K)			Poisson's ratio v		
	E_x	E_y	E_z	α_x	α_y	α_z	υ_x	υ_y	υ_z
Nicalon	200	200	200	3	3	3	.12	.12	.12
SiC	350	350	350	4.6	4.6	4.6	.2	.2	.2
Carbon	12	40	40	28	2	2	.4	.12	.12
Alumina	380	380	380	8.3	8.3	8.3	.22	.22	.22
Mullite	220	220	220	5	5	5	.27	.27	.27
BaZPS with x=0.25	50	50	50	1	1	1	.2	.2	.2
Al_2TiO_5	11	11	11	1	1	1	.22	.22	.22

Based on the FEM results, among the three parameters, Young's modulus, coefficient of thermal expansion and Poisson's ratio, the Young's modulus plays a more

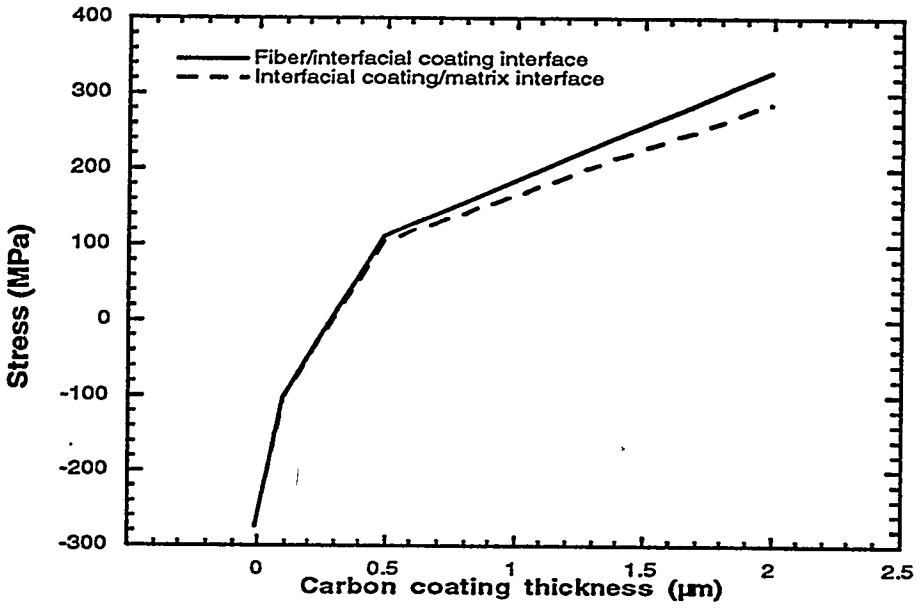

Fig. 2 Effect of carbon coating thickness on the calculated residual radial thermal stresses derived from the finite element model

dominant role. For example, as the modulus of the coating is decreased (e.g., from alumina to aluminum titanate) the difference in residual stresses that are generated at the fiber/interfacial coating and interfacial coating/matrix interfaces are reduced (Fig. 3). Further, the materials with low Young's modulus (e.g., aluminum titanate) cause a reduction in compressive thermal residual stresses similar to that for the 0.1 μm thick carbon coating.

Moreover, for interfacial materials with the same modulus, a material with a higher thermal expansion coefficient than that of the fiber and matrix is more effective in reducing radial stresses than is a material with a lower or similar thermal expansion. Trends similar to those reported here were observed with Hsueh's[10] model as well.

Experimental Results

Nicalon^{TM} (Ceramic Grade Nicalon, Nippon Carbon Company, Tokyo, Japan) fibrous preforms were prepared by stacking multiple layers of plain weave cloth in a 0±30

sequence within the cavity of a graphite holder. The preform was compressed by hand

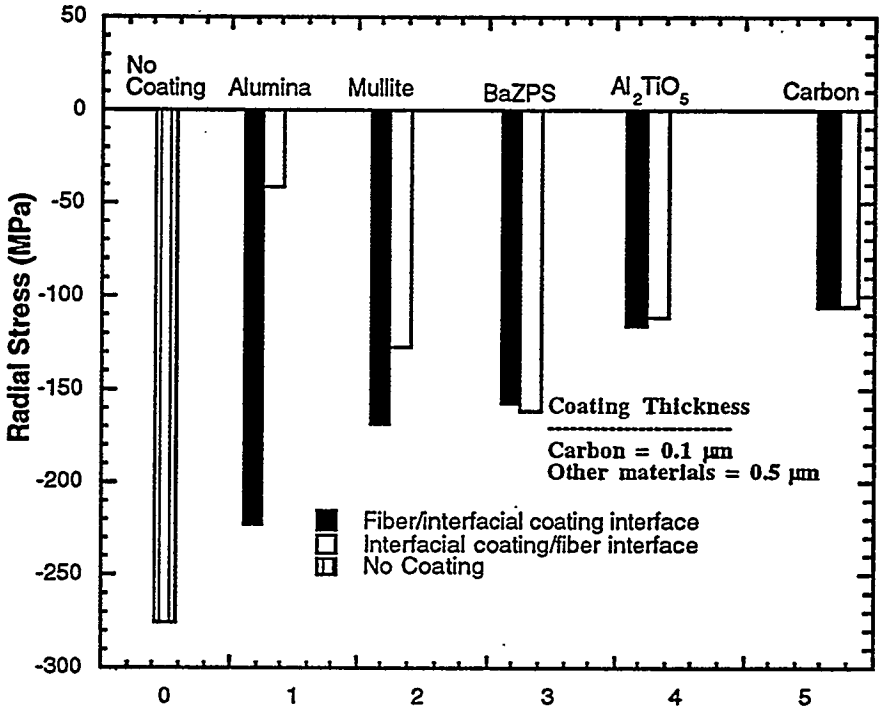

Fig. 3 Finite element computations indicate that low modulus interfacial coatings reduce compressive radial stresses

and held within the graphite holder with a graphite lid. The cloth sizing was removed by heat treatment at 973 K in argon for 2 h. The average fiber content of the resulting fiber preforms was 40 vol% with sample dimensions of 45 mm in diameter and 12.25 mm in thickness.

The carbon interfacial coating was deposited from a dilute argon/propylene mixture at 1373 K and 3 kPa pressure. The alumina (Grade RCHP-DBM, Reynolds Aluminum,) and mullite (Baikowski International Corporation, North Carolina) interfacial coatings were applied starting from powders using a novel colloidal process developed at Oak Ridge National Laboratory. Preforms with alumina and mullite interfacial coatings were then sintered in argon at 1373 K for 2 h.

The coated preforms were infiltrated with SiC matrix using the forced-flow, thermal-gradient chemical vapor infiltration (FCVI) process.[2] The SiC matrix was deposited from the decomposition of methyltrichlorosilane (MTS) in hydrogen. The process parameters are as follows: Hot surface temperature of 1473 K; MTS flow of 0.307 g/min; hydrogen flow of 500 cm^3/min; and exhaust pressure of 101 kPa. Typically, the matrix infiltration was completed within 20 hours.

The infiltrated Nicalon^{TM}/SiC composites were cut into twenty-four flexural bars of average size 2.5 x 3.0 x 40 mm. The dimensions of the cut flexural bars were measured and they were weighed to determine densities. Half of the flexure bars were then heat treated at 1273 K for 24 h in air to determine their oxidation behavior. The bars were loaded perpendicular to the layers of the cloth and the fracture surfaces were examined by scanning electron microscopy.

Fracture surface examination of composites with carbon interfacial coatings showed considerable fiber pull-out before oxidation (Fig. 4a). However, after oxidation they exhibited brittle fracture with very little fiber pull-out (Fig. 4b) due to the oxidation of the carbon interlayer and the subsequent formation of silica that bonded the fibers to the matrix.[5,11] The fracture surface of a composite with an alumina interfacial coating also showed very little fiber pull-out after oxidation (Fig. 5) and Langley et al.[12] reported that the tensile strength of Nicalon^{TM} fibers coated with alumina by plasma CVD were reduced by 30-40% compared to fibers similarly coated with carbon. The fiber damage was attributed to either chemical reaction or mechanical damage resulting from the thermal expansion mismatch between fiber and coating, or a combination of both. Walukas[13] observed that sol-gel derived alumina interfacial coating reacted with silica in the Nicalon^{TM} fiber during composite densification to form mullite. The fracture surface of the composite with a mullite interfacial coating, however, displayed considerable fiber

pull-out before and after oxidation (Fig. 6), however, the non-uniformity of the coating is a problem, and regions with considerable fiber-pull out are adjacent to regions of brittle fracture (Fig. 7). The accumulation of coating material around the fibers in certain areas also resulted in the lack of matrix in those areas. Preliminary thermodynamic calculations indicate that mullite coatings are likely to be stable with the Nicalon^{TM}/SiC system.

In order to overcome the non-uniformity problem a sol-gel approach is being pursued to deposit mullite coatings. Mullite sols with yield of the oxides ranging from 1-5% were used for coating Nicalon^{TM} fabric. The sizing on the Nicalon^{TM} was removed by heat treatment at 600°C for 1 h. The Nicalon was coated just after the removal of the sizing and pretreatment with methanol as well. The fabric was dipped into the mullite sol and dried either in air or in the presence of saturated methanol solution. Several combinations were tried and it was found that mullite sols with 1 wt% yield and dried in the presence of a saturated methanol atmosphere produced the best coatings. Figures 8a and 8b show the mullite coating on untreated Nicalon^{TM} fabric after 1 and 3 dips, respectively and dried in air. Figure 9 shows the mullite coating on a Nicalon fabric pretreated in alcohol and dried in the presence of a saturated methanol atmosphere. Coatings obtained under controlled drying conditions (Fig. 9) exhibited better uniformity than the coatings dried in air (Fig. 8).

Conclusions

FEM analysis revealed that a low modulus interfacial coating may be effective in reducing radial residual stresses that result from cooling from processing temperatures. Further, for the interfacial materials with the same modulus, a material with a higher thermal expansion coefficient than that of the fiber and matrix is more effective in reduc-

ing the radial stresses than is a material with a lower or similar thermal expansion coefficient.

Composites with carbon and alumina interfacial coatings exhibited brittle fracture after oxidation. However, a composite with a mullite interfacial coating retained considerable fiber pull-out, suggesting that it may be a desirable interfacial coating. Colloidal coating application, however, resulted in non-uniform mullite coatings. Potentially, the use of sol-gel methods may result in coatings with much better uniformity.

REFERENCES

1. N. Chawla, P. K. Liaw, E. Lara-Curzio, R. A. Lowden and M. K. Ferber, Symposium on "High Performance Composites," TMS, Warrendale, PA, K. K. Chawla, P. K. Liaw and S. G. Fishman, eds., 291, 1994.
2. T. M. Besmann, B. W. Sheldon, R. A. Lowden, and D. P. Stinton, Science, 253, 1104, 1991.
3. D. P. Stinton, A. J. Caputo, and R. A. Lowden, Am. Ceram. Soc. Bull., 65 (2), 347, 1986. 4. K. M. Prewo and J. J. Brennan, J. Mater. Sci., 15, 463, 1980.
5. A. G. Evans and D. B. Marshall, in Fiber Reinforced Ceramic Composites: Materials, Processing and Technology, ed. by K. S. Mazdiyasni, Noyes Publications, Park Ridge, NJ, 1, 1990.
6. D. B. Marshall and A. G. Evans, J. Amer. Ceram. Soc., 68 (5), 225, 1985.
7. R. W. Rice, Ceram. Eng. Sc. Proc., 2 (7-8), 661, 1981.
8. F. Rebillat, Unpublished work
9. Engineered Materials Handbook, Vol. 4, Ceramics and Glasses, ASM International, 1991.
10. C. H. Hsueh, P. F. Becher, and P. Angelini, J. Am. Ceram. Soc., 71 (11), 929, 1988.
11. B. A. Bender et al., Ceramic Eng. Sci. Proc., 5 (7-8), 614, 1984.
12. N. R. Langley et al., in Metal Matrix, Carbon and Ceramic matrix Composites,, ed. by J. D. Buckley, 1987.
13. D. M. Walukus, A Study of the Mechanical Properties and Oxidation Resistance of Nicalon-SiC composites With Sol-Gel-Derived Oxide Interfacial Coatings, M. S. Thesis, University of Tennessee, May 1993.

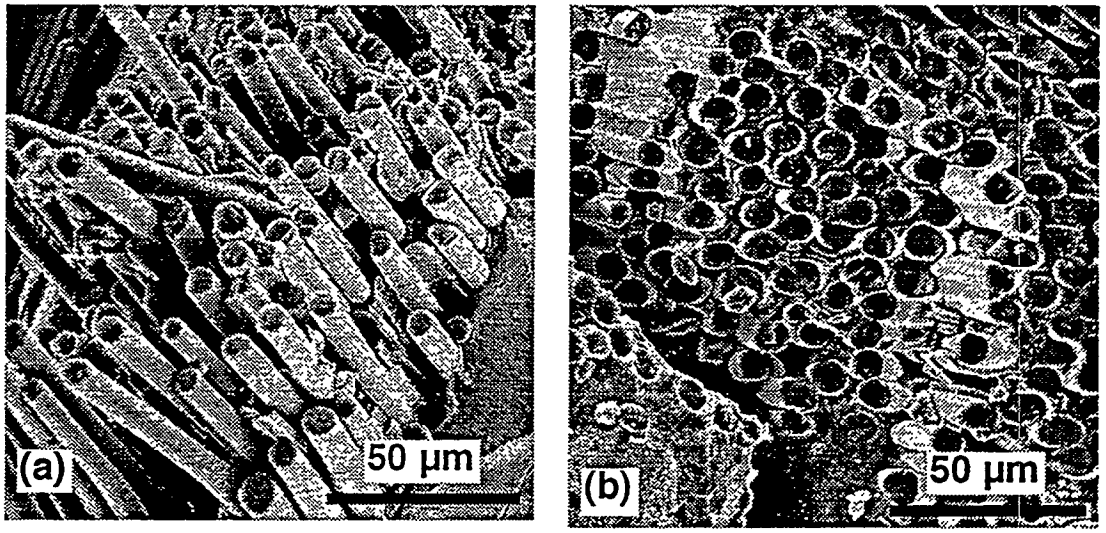

Fig. 4 Fracture surface of a composite with carbon interfacial coating
(a) before oxidation and (b) after oxidation in air for 24 h at 1273 K

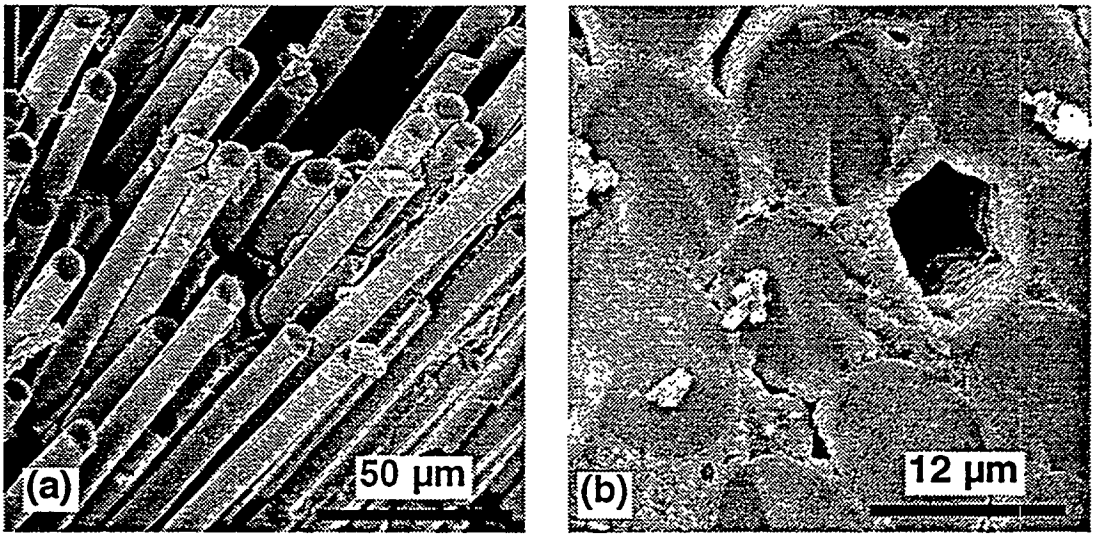

Fig. 5 Fracture surface of a composite with an alumina interfacial coating
(a) before oxidation and (b) after oxidation in air for 24 h at 1273 K

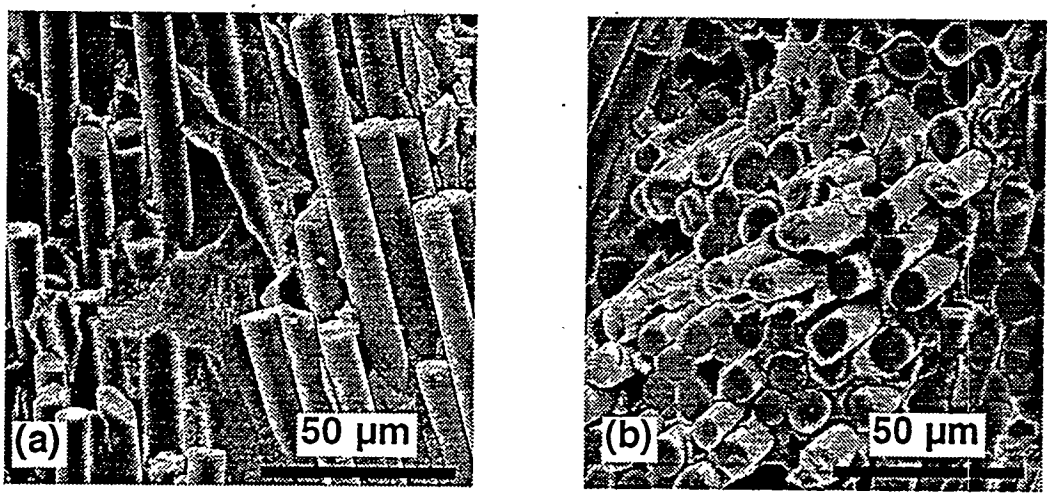

Fig. 6 Fracture surface of a composite with a mullite interfacial coating (a) before oxidation and (b) after oxidation in air for 24 h at 1273 K

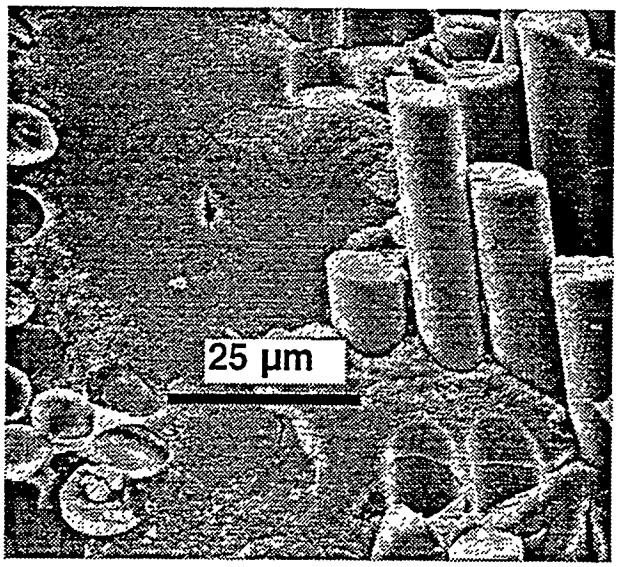

Fig. 7 Non-uniformity of the mullite interfacial coating resulted in fiber pull-out in certain regions and brittle fracture in other areas

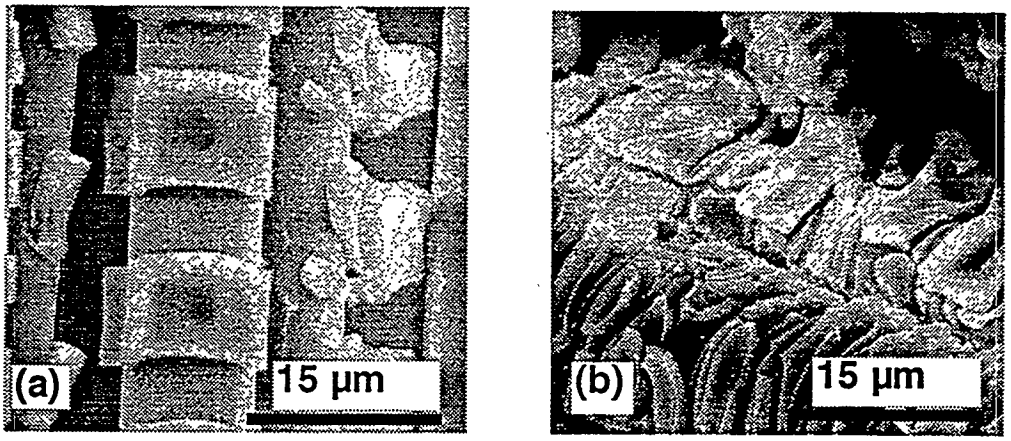

Fig. 8 Mullite coating on the untreated Nicalon fabric (a) after 1 dip and (b) after 3 dips

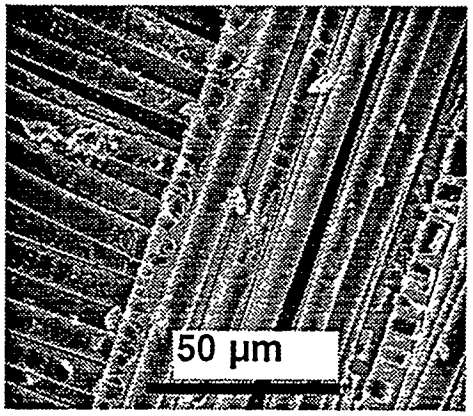

Fig.9 Mullite coating on Nicalon fabric after pretreatment with methanol and dried in the presence of a saturated methanol atmosphere

MODELING OF FIBROUS PREFORMS FOR CVI FABRICATION

T.L. Starr and D.Y. Chiang

School of Materials Science and Engineering
Georgia Institute of Technology
Atlanta, Georgia 30332-0245

This program involves modeling the chemical vapor infiltration (CVI) of tube shapes in support of experimental process development at Oak Ridge National Laboratory (ORNL). The previously developed tube model, including radiative heat transfer, has been modified to match the new, larger reactor at ORNL. For infiltrating tubes 4" OD and 12-18" L, higher reactant flow rate is needed for rapid densification.

Two new processing schemes are being investigated. In the first, the processing parameters - temperature, flow rate, etc. - are varied through the run in order to maintain optimum densification performance. In the second, processing conditions near the end of the run are adjusted to close residual porosity and to produce a gas-tight tube. For each of these, model runs will identify process schedules prior to experimental runs at ORNL.

INTRODUCTION

Chemical vapor infiltration is an effective method for fabrication of tube shapes for fossil energy applications. Equipment design and process conditions are significantly different than for disk-shaped components fabricated previously. A new, larger tube infiltration system has been installed at ORNL. Our previously developed process model is being modified to match this new reactor. Initial model runs have focused on the temperature profile in the system and its effect on infiltration performance. In the future, the model will be used to identify variable condition runs for reduction of densification time and hybrid processing for production of gas-tight tubes.

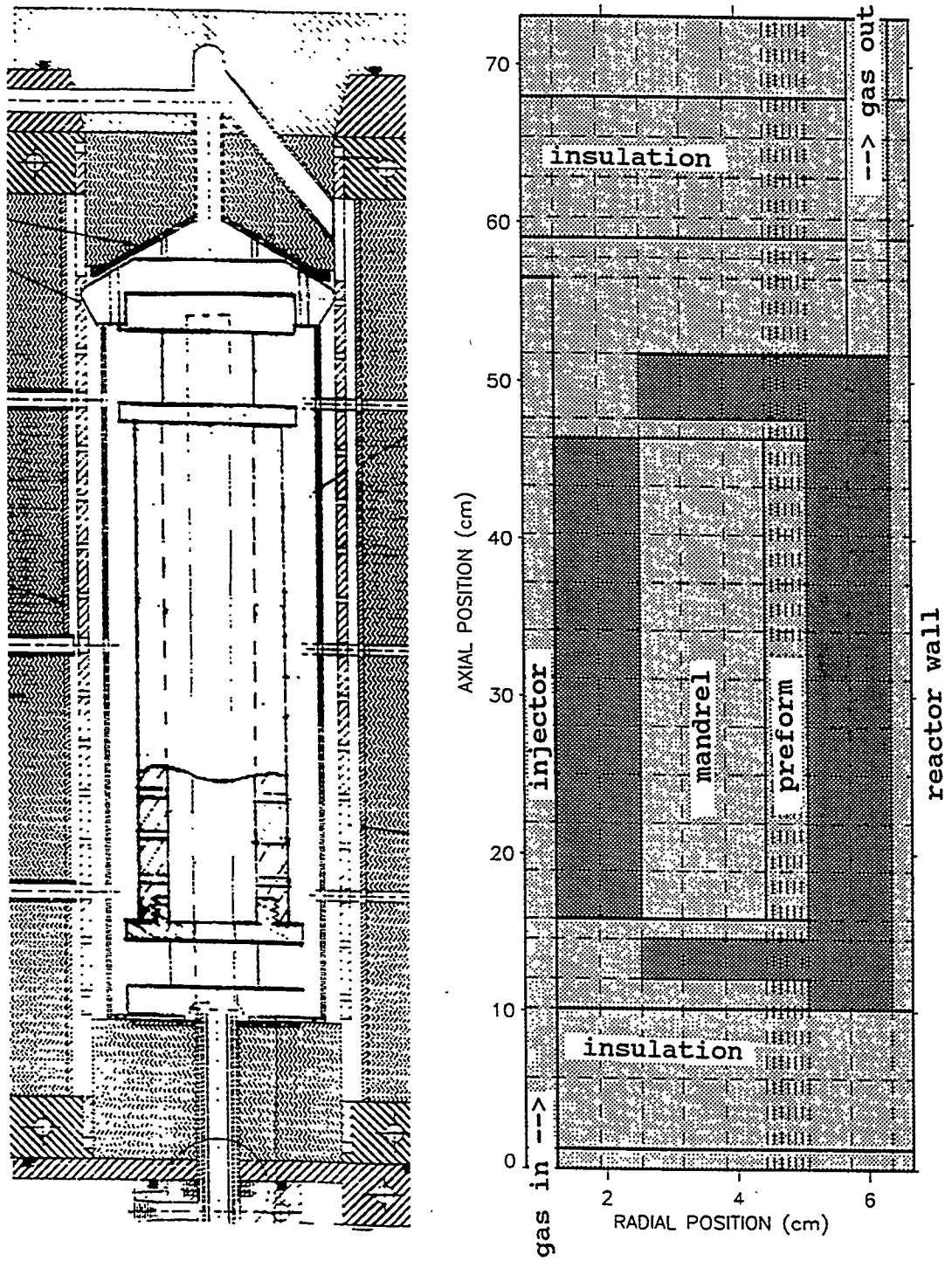

Figure 1. The new tube CVI system at Oak Ridge National Laboratory (left) is modeled using a 15x26 volume element grid (right). (Note that the radial and axial scales are different.)

as our model predictions are compared to actual temperature profiles measured at ORNL.

Table I. Thermal conductivity for materials in ORNL tube infiltration system.

MATERIAL	LOCATION	THERMAL CONDUCTIVITY (W/cmK)
graphite H451	Mandrel, endcap	$73.7xT^{-2/3}$ (0.87@500°C)
aluminum	furnace enclosure	2.3
carbon-carbon composite	reactor wall	$73.7xT^{-2/3}$ (0.87@500°C)
carbon fiber insulation	ends of reactor	$7.37xT^{-2/3}$ (0.087@500°C)
stainless steel	gas injector	0.30
Nicalon fiber cloth layup	preform - radial - axial	.00708/(1.012-ρ) .0539/(1.077-ρ) ρ=fraction dense

Using these values the CVI model predicts the temperature profile shown in Figure 2 for a reactor wall temperature of 1300°C. The ends of the preform are significantly cooler than the center of the tube. In the end regions there is good thermal contact to the cool injector through the high thermal conductivity H451 graphite. In the tube middle the thermal contact relies on radiation across the gas space which is inefficient at the temperature involved.

The temperature profile through the preform is plotted in Figure 3 for three different wall temperatures and for the middle and ends of the tube. Overall the temperature difference between the cool and hot side of the preform is in the range 300-450°C. The cool side temperature at the tube end nearest the gas inlet is approximately 170°C lower than in the middle, while the other end of the tube is 150°C cooler than the

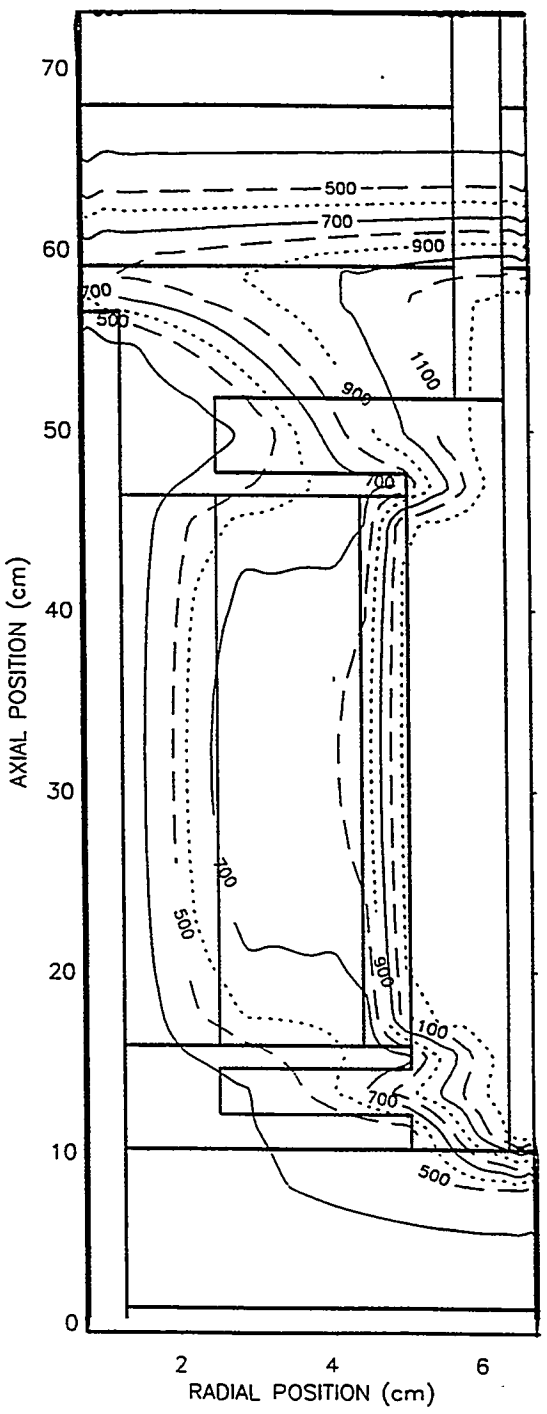

Figure 2. Model predicts the above temperature profile for a reactor wall temperature of 1300°C. Ends of preform are significantly cooler than the middle.

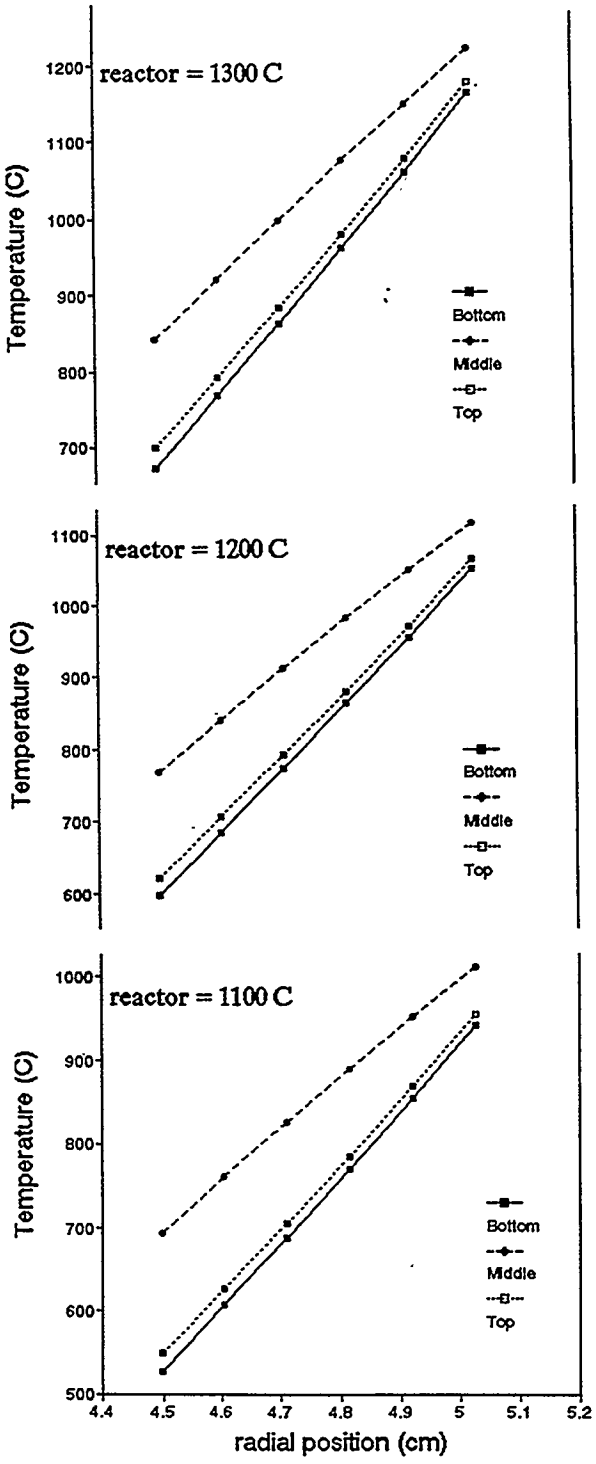

Figure 3. Temperature profile through preform depends on reactor wall temperature and on position along tube length.

middle. This suggests that densification may be significantly slower in these regions although the gas flow pattern also will influence densification behavior.

PROCESS OPTIMIZATION

Once the model is verified by comparison to experimental results, it will be used to "optimize" the tube densification process. This optimization has two objectives: reduce the processing time and produce gas-tight tubes. Achieving these goals will require two distinct approaches.

Optimized processing conditions for reduced process time will involve adjustment of the furnace temperature, reactant concentration, and gas flow rates throughout the run according to the changing physical properties of the preform. Processing using these variable conditions is expected to result in significantly reduced infiltration times as compared to current practice where process conditions are held constant for the duration of the run. In particular, we have seen previously that the preform temperature drops during a run as the composite becomes denser, with a higher thermal conductivity, and provides better thermal contact to the cool injector. We will devise an increasing reactor temperature schedule to counteract this effect and maintain the preform at the highest temperature consistent with fiber stability and uniform densification.

Secondly, we plan to reduce the overall gas flow rate near the end of the run as the composite becomes less permeable. This will allow continued infiltration for some period of time beyond the normal process endpoint.

While this optimized processing will produce tubes with less than 10% porosity, "hybrid" processing techniques will be identified that utilize diffusion-driven CVI to further reduce permeability. At the point where forced flow can no longer be maintained, the process will be adjusted to allow diffusion of reagent from the cool side into the preform. This one-sided infiltration is capable of producing true, gas-

tight materials. The model will be used to identify suitable conditions for this process.

SUMMARY

Initial modeling of the new ORNL tube infiltration system has been completed. Comparison of model predictions with experimental temperature profile and densification performance will be made.

The verified process model will be used to identify process conditions for reduction of densification time and for production of gas-tight tubes.

REFERENCES

1. T.L. Starr and A.W. Smith, "Modeling of Forced Flow/Thermal Gradient Chemical Vapor Infiltration", Oak Ridge National Laboratory Report ORNL/sub/85-55901/03 (September 1993).

ENGINEERING SCALE DEVELOPMENT OF THE VAPOR-LIQUID-SOLID (VLS) PROCESS FOR THE PRODUCTION OF SILICON CARBIDE FIBRILS AND LINEAR FIBRIL ASSEMBLIES

Michael Tenhover and Joseph Biernacki

The Carborundum Company
Technology Division, P.O. Box 832
Niagara Falls, NY 14320

Kathleen Schatz and Frank Ko

Advanced Product Development, Inc.
2500 Pearl Buck Road
Bristol, PA 19007

ABSTRACT

In order to exploit the superior thermomechanical properties of the VLS fibril, the feasibility of scaled-up production of the SiC fibril is demonstrated in this study. Through time series study and computer simulation, the parameters affecting the growth process and properties of the fibrils were examined. To facilitate translation of the superior mechanical properties into higher level preform structures, conventional and unconventional processing methods were evaluated. As revealed by scanning electron microscopic examination and X-ray diffractometry, high level alignment of the fibrils was achieved by the wet-laid process.

INTRODUCTION

The development of high-temperature ceramic composite reinforcement materials is critical for the continued development of fracture-resistant, high-temperature ceramic composite materials for high-temperature applications in DOE Fossil Energy programs. The VLS SiC fibrils, being single-crystal SiC, have unmatched high-temperature tensile strength, modulus, and creep resistance compared to other ceramic composite reinforcement materials. The SiC fibrils could be a critical, enabling reinforcement for DOE Fossil Energy program applications requiring high-temperature (>2400°F) ceramic composite materials.

In order to develop a reliable supply source for the VLS SiC fibril, the feasibility of scale-up of the VLS process for producing SiC fibrils was examined through time series growth experiments and a computer simulation model. Laboratory scale post processing methods have been developed to facilitate fibril harvesting and beneficiation of medium and short length fibrils as well as reducing the undesirable small diameter fibrils.

In order to maximize the translation of fibril properties to the composite and facilitate the ceramic composite manufacturing process conventional and unconventional textile fiber processing methods were evaluated for the processing of the fibrils. It was concluded that a fluid-based (wet)

process will provide the most gentle media for the dispersion, alignment, and integration of the fibrils. A manual batch process was established to produce linear fibrous assemblies through dispersion and subsequent alignment of the fibrils by fluid flow. The inter-fibril cohesion was provided both by the use of chemical binders and different auxiliary sheath techniques. As illustrated by SEM observations and X-ray diffractometry, a high level of fibril alignment was achieved by the wet process. These aligned fibril linear assemblies will be fabricated into a ceramic matrix composite by the CVI process for preliminary characterization of the properties of the ceramic composite system.

THE VLS SiC FIBRIL GROWTH PROCESS

The chemistry of the VLS process for producing SiC fibrils has been described elsewhere. [1,2] The Carborundum development reactor incorporates many features of the Los Alamos National Laboratory (LANL) reactor design.[2,3] Figure 1 shows the reactor design concept. The critical difference between the Carborundum and LANL reactor is its vertical dimension. The Carborundum reactor is 30.5 cm high (two times the height of the LANL reactor), which allows for the determination of critical scale-up parameters in the vertical dimension. It was expected that vertical scale-up of the process would produce the highest risk in increasing the reactor dimensions, and subsequent process development experiments have confirmed this assumption.[4]

Carborundum has explored the key process factors in the macroscopic growth process and has identified the effect of critical process and scale-up parameters. Delivery of both SiO and CH_4 control the fibril growth rate. The SiO and CH_4 concentration profiles exhibit different behavior as a function of reactor position, resulting in a continuous variation in the chemical conditions in the reactor. Despite this continuous variation, acceptable fibril morphologies can be grown throughout the reactor height. (Figure 1.)

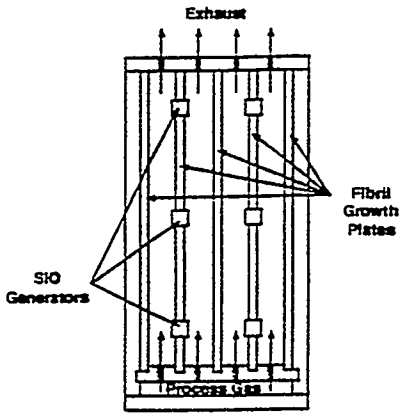

Figure 1. Carborundum development reactor.

Kinetic data obtained in development experiments have been incorporated in a simulation model. Three reactions control the fibril growth process -- SiO supply, CH_4 decomposition and the SiC fibril formation reaction. Taken together, these reactions interact to produce varying growth rates at different process conditions. The simulation model can predict critical trends in the SiO generation. CH_4 delivery and SiC fibril formation using kinetic constants derived from experimental data. Figure 2 shows the effect of processing condition on fibril growth rate profile.

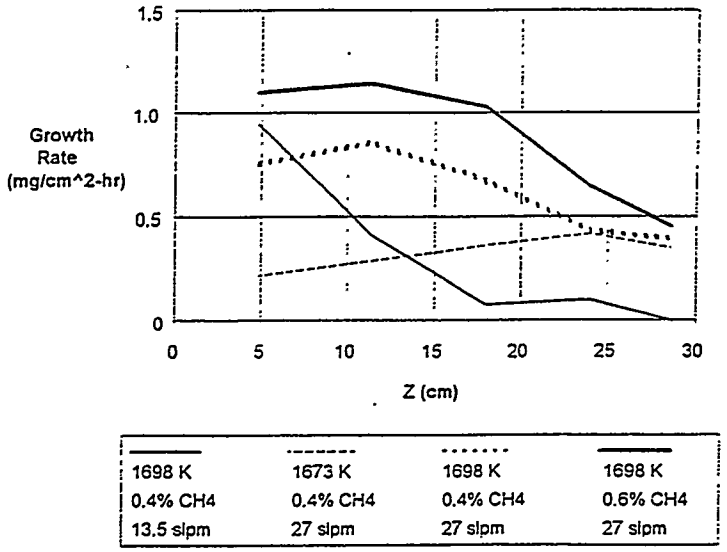

Figure 2. Effect of synthesis process conditions on fibril growth rate profiles.

Both the fibril post-processing and process gas recycle portions of the process are important to the viability of the process. Harvesting/beneficiation has focused on identifying process steps to remove residual catalyst and product beneficiation to remove undesirable by-products. The beneficiation step needs to be tied to the desired fibril product characteristics, since this process step can modify the product characteristics.

PROPERTIES OF SiC FIBRILS

VLS SiC fibrils have a number of attractive properties, which are the result of their single crystal structure. Table 1 summarizes different areas of fibril characterization and highlights some of the attractive features of the VLS SiC fibril.

Characteristic	Examples	Attractive Fibril Features
Physical	Morphology Length Diameter	Single crystal B-SiC Length: to 7 cm Diameter: 5 - 10 μm
Chemical	Bulk Chemistry Trace impurities	High purity
Mechanical	Tensile strength	Tensile strength ≥ 6 GPa
Thermal	Creep resistance Oxidation resistance	Creep resistance better than other SiC reinforcements

Table 1. Important areas of VLS SiC fibril characterization and attractive fibril features.

Diameter Analysis

Fibril diameter has important ramifications on the commercial viability of the VLS SiC fibril process. The diameter and its distribution may affect composite performance. The potential health hazard associated with fine diameter fibrils is a concern. This has promoted efforts to improve control of the product diameter. To guide these efforts, a quantitative measurement technique based on optical microscopy combined with automated image analysis was used.

This technique involves the preparation of a dilute sample of shortened fibrils on an optical microscope slide. The slide was scanned across the viewing area at a magnification of 1250x and 100 diameter data points were accumulated. The diameter was measured using image analysis software and the diameter distribution was calculated by this software.

MECHANICAL PROPERTIES OF VLS SIC FIBRILS

The attractiveness of VLS SiC fibrils can be attributed to their high strength and unmatched thermal resistance, which results from the single crystal structure of the fibrils. VLS SiC fibril mechanical properties have been reported in other studies. [5,6] These results are summarized in Table 2.

Property	Measured By	Result
Tensile strength	Single fiber tensile testing - LANL [7]	8.5 GPa (1200 ksi)
Elastic modulus	Single fiber tensile testing - LANL [7]	580 GPa (85000 ksi)
Creep resistance	Bend stress relaxation - NASA-LRC [2]	m = 1 @ 1673 K for 1 hour

Table 2. Mechanical and thermal resistance properties of VLS SiC fibrils from the literature.

To avoid potential inaccuracies associated with this methodology, Carborundum is evaluating the feasibility of using single fiber composite testing (SFC) techniques to evaluate the fibrils strength. [7] This technique has been used to obtain useful strength data of materials down to very small gauge lengths without the potential artifacts introduced by the single fiber tensile testing technique. [8] The test involves imbedding a single fibril in an epoxy matrix and stressing the matrix. By measuring the number and location of the fibril breaks as a function of the stress on the sample, the fibril strength and the statistical analysis of the strength can be obtained. This preliminary work has been performed by Anil Netravali at Cornell University. The preliminary tests indicated fibril strengths of 6 - 9 GPa at a 2.54 cm gauge length, with a Weibull modulus of 3 - 3.5.

Another attractive property of the VLS SiC fibril is its unmatched creep resistance relative to other SiC reinforcements. An article describing a simple technique of measuring creep resistance and it application to the evaluation of fiber reinforcements has been published. [5] In testing at temperatures of 1673 K for 1 hour, the VLS SiC fibril exhibited the highest degree of creep resistance relative to any other SiC reinforcement. No creep was noted, leading to an m value of 1.

DEVELOPMENT OF LINEAR FIBRIL ASSEMBLIES

Preform fiber architecture has been demonstrated to play an important role in facilitating the processing and enhancing the toughness of ceramic matrix composites.[9] In order to exploit fully the superior strength, modulus and thermal stability of the SiC fibril produced by Carborundum considerable effort has been devoted in the industry to convert the fibrils to linear fibrous assemblies. [9,10] As illustrated in Figure 3 plotting critical fiber diameter as a function of tensile modulus, the SiC fibril (which has a modulus of approximately 600 GPa and diameter of 5 ± 3 μm) is on the fringe of being processable as a textile fiber because its fine diameter could compensate for its high modulus.

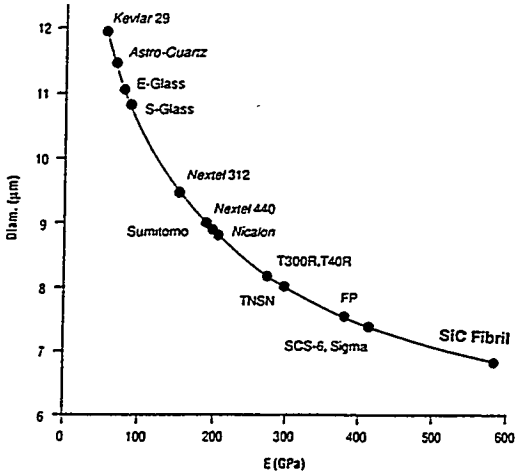

Figure 3. Critical fiber diameter for successful textile processing.

In order to assess the feasibility of converting the SiC fibril to fibrous assemblies, the key technical issues in the processing of SiC fibrils were examined. It was identified that, similar to conventional textile yarn processing, dispersion, alignment and integration of the fibril assemblies are the essential ingredients for the successful conversion of the fibril to a textile-like linear fibrous assembly. In this program, the feasibility of the conventional textile yarn processes were first examined followed by an evaluation of alternate unconventional processes. A summary of the operations corresponding to the conventional and unconventional processing methods is shown in Table 3.

	Conventional Textile Processing	Adhesive Tape Processing	Wet-Laid Processing
1) Separation	Opening, Carding	Aligning on growth Plate	Dispersion in liquid medium
2) Alignment	Carding	Aligning on growth Plate	Alignment in flow of dispersion medium
3) Attenuation or other control of linear density of fibrils	Drafting	None; Dependent on fibril growth density and length	Accumulation
4) Integration	Spinning Twist insertion or Fiber entanglement	Adhesive Tape Application	Binder and auxiliary tape substrate

Table 3. Basic processing steps in conventional and unconventional methods.

CONVENTIONAL PROCESSES

The conventional yarn spinning process which converts short fibers into continuous yarns consists of four steps: separation, alignment, attenuation, and integration. In traditional yarn manufacturing, separation and alignment steps are achieved by carding, producing a web of fiber. This web is condensed into a thick untwisted rope which is attenuated and further aligned through a drafting process. Spinning re-entangles the well aligned fibers in a controlled manner through a twisting process to give the yarn strength. With a focus on achieving fibril alignment and creating structural integrity our research was focused on the carding and spinning process.

Carding

Carding is a well established process for the orientation of textile fibers wherein the fibers are subjected to the opposing action of metallic wires as shown in Figure 5. Due to the limited availability and the high modulus nature of the SiC fibril, a model SiC fiber Nicalon (which has 50% lower modulus than the fibril) was used to test a laboratory scale carding machine constructed for this study. It was founded that , besides the formation of fiber clusters, a great deal of damage was done to the Nicalon fibers and the yield was extremely low. Accordingly, it was concluded that the carding process is

unsuitable for processing fibers such as Nicalon even with the aid of a carrier fiber. Therefore, no further trial was attempted to align the fibril with the carding process.

Air Vortex Spinning

In order to minimize the contact of fibrils with mechanical surfaces in traditional spinning operations, a laboratory scale air vortex spinning apparatus (Figure 6) was constructed to align and integrate the fibril into a linear assembly. It was found that a great deal of carrier fibers would be needed even with the Nicalon model fiber in order to obtain a linear strand. Substantial damage occurred on the Nicalon fiber due to the whipping/twisting motion and contact with the wall of the air duct. It was concluded that it would be difficult for the fibril to survive the air vortex spinning process.

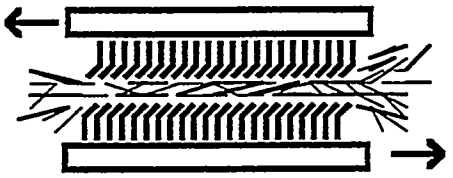

Figure 5. Carding operation.

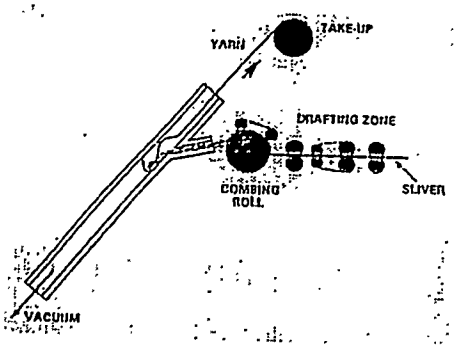

Figure 6. Air vortex spinning.

UNCONVENTIONAL PROCESSES

It was clear from the lessons learned in the unconventional processes that in order to process ultra-high modulus materials such as SiC fibril, one must keep handling to its minimum, the fibrils to fibril contact should be minimized, and the fibrils should be well separated during the gentle/non

twisting alignment process. Out of a list of ten candidate unconventional processing methods, the adhesive tape and the wet-laid processes were selected for further examination.

Adhesive Tape Process

In the adhesive tape method is a direct process wherein separation and alignment would occur while the fibrils were still anchored on the growth plate, through a combing or brushing step. Like hair on a scalp, fibril entanglement is limited to the entanglement which is formed as the fibrils grow together, and can be modified by controlling growth density and fibril growth length. Once oriented, the fibrils can be removed from the plate by applying and removing an adhesive tape, which provides the integration. In this process, an attenuation step does not occur, as the linear weight is dictated by the fibril growth on the plate. (Figure 7.)

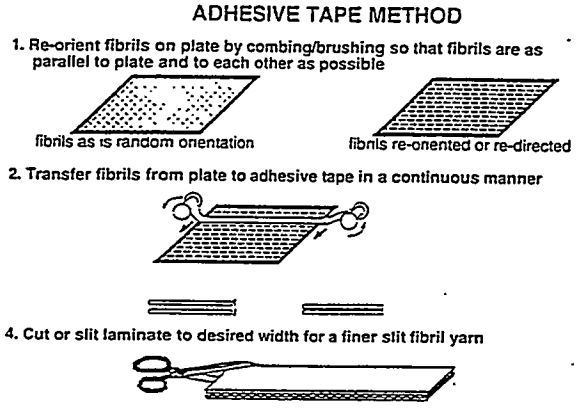

Figure 7. Adhesive tape process.

Wet-Laid Process

The wet-laying process is a gentle process wherein the fibrils can be protected from each other through surface charge modification and orientation is induced by fluid flow. The first operation of wet-laying is the dispersion (or separation) of fibrils in a liquid medium to the degree that the fibrils are *discretely* suspended. Alignment occurs when the liquid medium is allowed to flow in a controlled manner and the dispersed fibrils align in the flow onto a porous screen where the liquid is removed. Attenuation can occur at two points. The first opportunity for attenuation occurs when the fibrils are rinsed of the dispersion medium by a flow of plain water, after which a binder is applied to give the fibrous array enough strength to be lifted from the screen. A second opportunity for attenuation can occur when the still-wet fibrils slide past each other as they are transferred from one surface to another. (Figure 8)

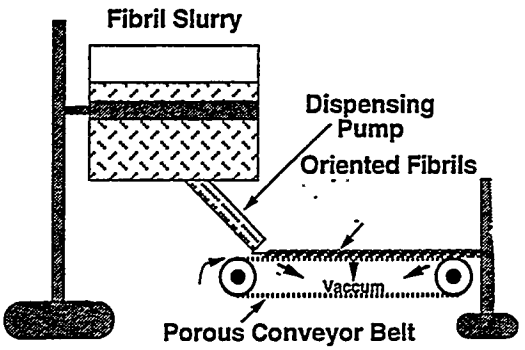

Figure 8. Wet-laid process.

CHARACTERIZATION OF FIBRIL ALIGNMENT

A major objective in the formation of linear fibril assembly is to create high level of fibril alignment. The degree of alignment can be studied by scanning electron microscopic(SEM) observation and X-ray diffractometry by examination of the peak height ratio between (220) and (210) . An examination of the SEM photographs of the adhesive tape and the wet-laid fibrils as shown in Figures 9 and 10 respectively, demonstrated that the wet-laid process produced a well aligned linear assembly whereas fibril assembly produced by the adhesive tape process tends to be random. This difference in alignment was further confirmed by X-ray diffractometry as shown in Figures 11 and 12.

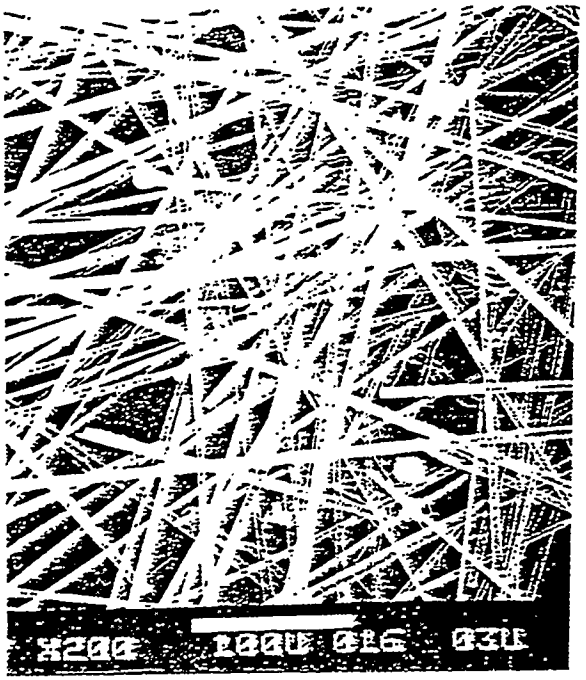

Figure 9. SEM photograph of fibrils aligned by adhesive tape process.

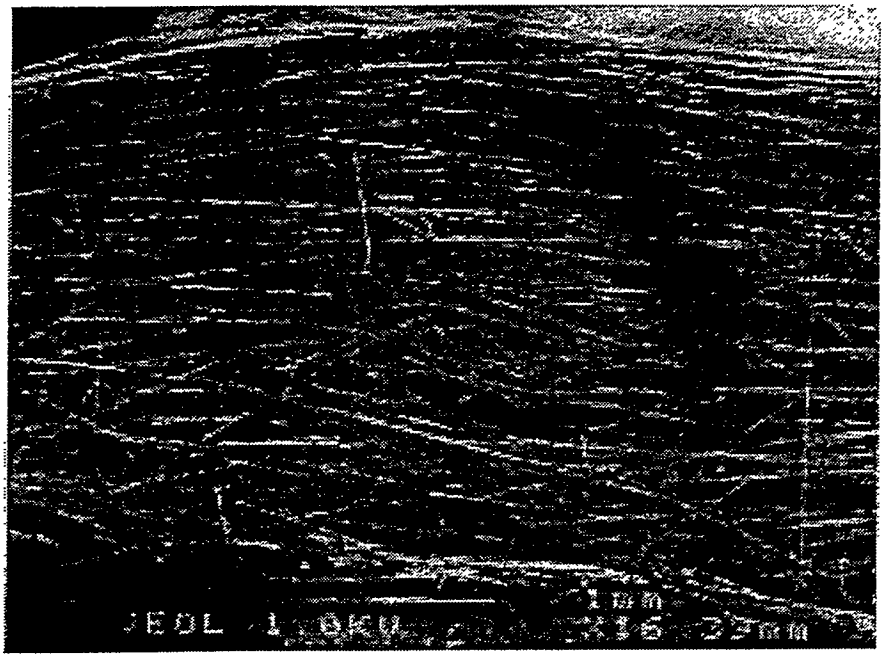

Figure 10. Photograph of fibrils aligned by wet processing.

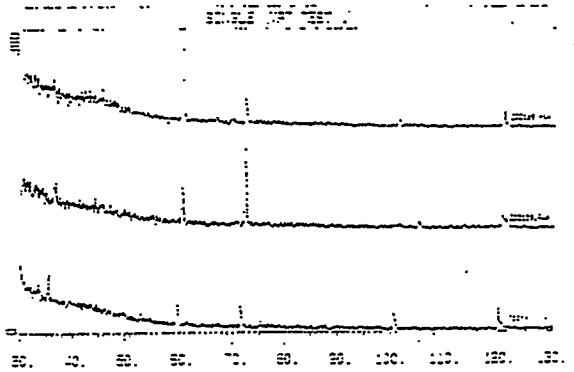

Figure 11. X-Ray diffractometry of fibrils aligned by adhesive tape process.

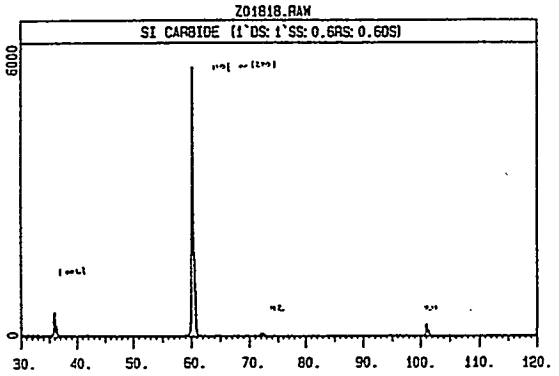

Figure 12. X-Ray diffractometry of fibrils aligned by the wet-laid process.

CONCLUSIONS

This study demonstrated that engineering scale production of SiC fibril is feasible and high level of fibril alignment can be achieved by the wet-laid process. By time-series experiments the critical variables in the growth process of SiC fibril were identified and evaluated. A computer simulation model was established to predict fibril growth rate as a function of process parameters which will facilitate future reactor design and development .With an average growth rate of 0.65 mg/cm^2/hr , the diameter of 99% by weight of the fibril were above 3μm. The tensile strength of the fibril was also confirmed to be consistent with the literature, at the level of 6-9 GPa. In order to maximize the translation of the unique tensile properties to a higher level structure and finally the composite, conventional and unconventional fiber processing methods were examined. It was concluded that conventional methods such as carding and spinning, even with modification, are not applicable to the processing of SiC fibril due to excessive fiber damage and inability to separate and align the high modulus fibers. Of the unconventional processes such as the adhesive tape and the wet-laid method, although substantial simplification can be made with the adhesive tape process the level of fibril alignment and volume fraction are lower than that by the wet-laid process.

This study has established the necessary foundation for a scale up process for the fibril growth, harvesting and conversion into well oriented linear, planar and 3-D assemblies with controlled fibril fractions suitable for the production of ceramic matrix composites. A follow-on program has been planned to optimize the wet-laid process and establish a pilot scale wet-laid production facility capable of near net shape production of fibril preforms for heat exchangers and other CMC products of interest to the DOE Fossil Energy AR & TD Program.

REFERENCES

1. Hollar, W.E. and J. J. Kim, "Review of VLS SiC Whisker Growth Technology," *Ceram. Eng. Sci. Proc..*, 12[7-8], p 979 - 991 (1991).

2. Shalek, P.D., D.E. Christiansen, F.D. Gac. R.E. Honnell, G.F. Hurley, J.D. Katz, W.J. Parkinson, J.J. Petrovice and D.S. Phillips, "Scale-up and Optimization of the VLS Growth Process for Beta-SiC Whiskers for the Period KApSiptember - 1989," DARPA Final Report & DOE/OAR&TD Topical Report, Los Alamos National Laboratory Report #LA12119 (1992).

3. Hollar, W.E., J.J. Kim and W.H. Mills, "The Growth Kinetics of VLS SiC Whiskers," presented at the 16th Annual Conference on Composites and Advanced Ceramics, Cocoa Beach, FL, January 1992.

4. Kim, J.J., W.E. Hollar, S. Chwastiak and W.H. Mills, "Engineering Scale Development of the Vapor-Liquid-Solid (VLS) Process for the Production of Silicon Carbide Whiskers."

5. Morscher, G.N. and J.A. DiCarlo, "A Simple Test for Thermomechanical Evaluation of Ceramic Fibers". *J. Am. Cer. Soc.*, 75 [1], 136 - 140 (1992).

6. Petrovic, J.J., J.V. Milewski, D.L. Rohr and F.D. Gac, "Tensile Mechanical Properties of SiC Whiskers," *J. Mat. Sci.*, 20, 1167 - 1177 (1985).

7. Netravali, A.N., L.T.T. Topoleski, W.H. Sachse and S.L. Phoenix, "An Acoustic Emission Detection Technique for Measuring Fiber Fragment Length Distributions in the Single-Fiber-Composite Test," *Comp. Sci. and Tech.*, 35, 13 - 29 (1989).

8. Srinivasan, G.V. and V. Venkateswaran, "Tensile Strength Evaluation of Polycrystalline SiC Fibers," presented at the 17 Annual Conference on Composites and Advanced Ceramics, Cocoa Beach, FL, January 12, 1993.

9. Ko, F., Preform Fiber Architecture for Ceramic Matrix Composites, Bulletin of American Ceramic Society, Vol. 68 No. 2 1989.

10. NASA Contractor Report CR-795, May 1967.

MECHANICAL PROPERTIES OF CERAMIC COMPOSITE TUBES

W. A. Curtin[1], L. L. Oleksuk[1], K. L. Reifsnider[1], and D. P. Stinton[2]
[1]Materials Response Group, Department of Engineering Science and Mechanics
Virginia Polytechnic Institute and State University, Blacksburg, VA 24061
[2]Oak Ridge National Laboratory, Oak Ridge, TN

ABSTRACT

Results of axial tension tests on SiC/SiC tubular ceramic composite components fabricated by a forced-CVI technique are presented. Axial elastic modulus measurements on a number of tubes show that the Young's modulus varies along the length of the tube, with occasional very stiff or very soft regions. Tests to failure on a few tubes show the initiation of non-linear stress-strain behavior to be in the range of 3-9 ksi, followed by extensive non-linear deformation up to failure. For one tube, the failure stress obtained was 20.1 ksi, but the strains to failure at various axial locations varies from 0.19% to 0.24%. The correlation between modulus and proportional limit is considered within the ACK matrix cracking theory and within a model in which matrix cracking between fiber tows occurs, both modified to account for matrix porosity. The crack size required to cause stress concentrations large enough to cause failure at the observed strength is considered. Predictions for both matrix cracking and strength suggest that the current generation of tubes are controlled by microstructural defects.

I. INTRODUCTION

Two of the major fossil energy technology applications for ceramic matrix composite (CMC) materials are heat exchangers and hot-gas filters. Both of these are tubular components with specific mechanical property requirements. The goal of the present effort is to assess the mechanical properties of tube components, rather than simple flat coupons, and to guide the development of advanced processing techniques used to fabricate such CMC components. In this paper, we will present and discuss results on elastic modulus, microcracking, and tensile failure, and the variations of these properties within a single component.

The CMC tubes studied here are composed of Nicalon™ fibers reinforced by a SiC matrix deposited by a forced-CVI technique[1]. The fiber preform is created by rolling 2d, plain weave mats woven from fiber tows. One set of fiber tows are aligned along the tube axis and the other tows are perpendicular and wind around the circumference. A thin carbon coating is deposited onto the fibrous preform prior to infiltration by CVI-SiC. The final components are 8 inches in length, with approximately 1" i.d. and 1.25" o.d.; the total fiber volume fraction is about 32%, while the porosity is between 10% and 25%, and is predominantly in the form of "interlaminar" pores between the 0° and 90° fiber tow. (Fig. 1).

II. EXPERIMENTAL RESULTS

Tensile testing along the axial direction of the tubes is performed using either an Instron or MTS servohydraulic testing device. Gripping, and prevention of grip failure, by the use of tapered end plugs has been discussed previously[2]. Because of the varying porosity observed qualitatively along the tube length, and the large size of the sample, we have investigated the axial Young's modulus at a number of

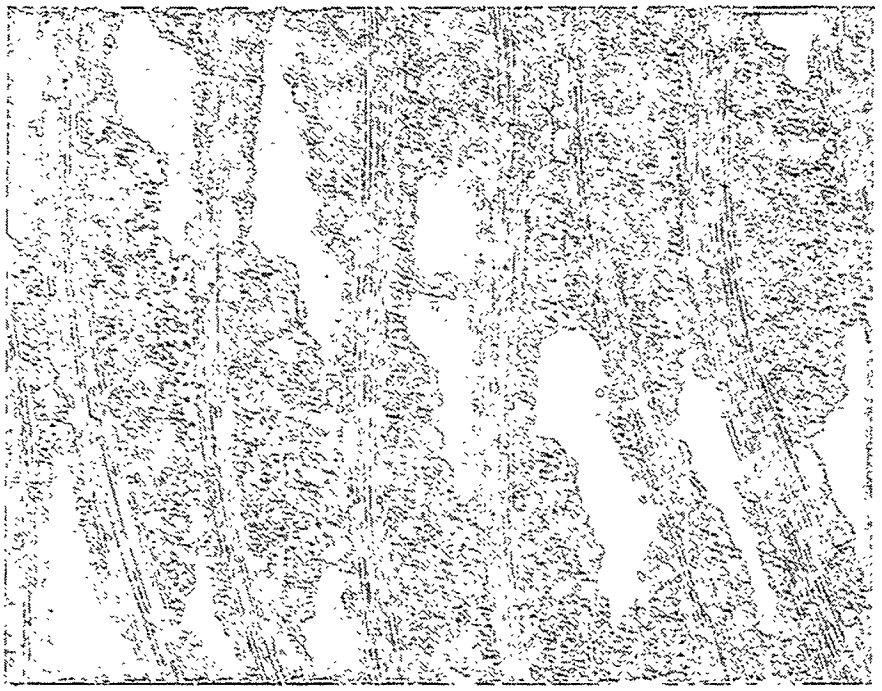

Figure 1. Optical micrograph of a typical tube cross-section. Dark regions are interlaminar porosity. Typical tow dimensions are 1000 μm x 150 μm. Upon matrix and 90° tow failure, "unbridged" regions between the 0° tows have a typical width of about 800 μm.

locations along and around the tube. Strain gauge pairs are equally spaced along the 6" gauge length of each specimen, and pairs at 90° rotation are also used to check angular modulus variations. The modulus measurements are carried out using strains less than 10^{-3} to avoid non-linearities associated with microcracking, and 3 load cycles are run to insure reversability and repeatability. Results on 4 different tubes (each with varying number of strain gauges) are shown in Figure 2. The axial modulus exhibits

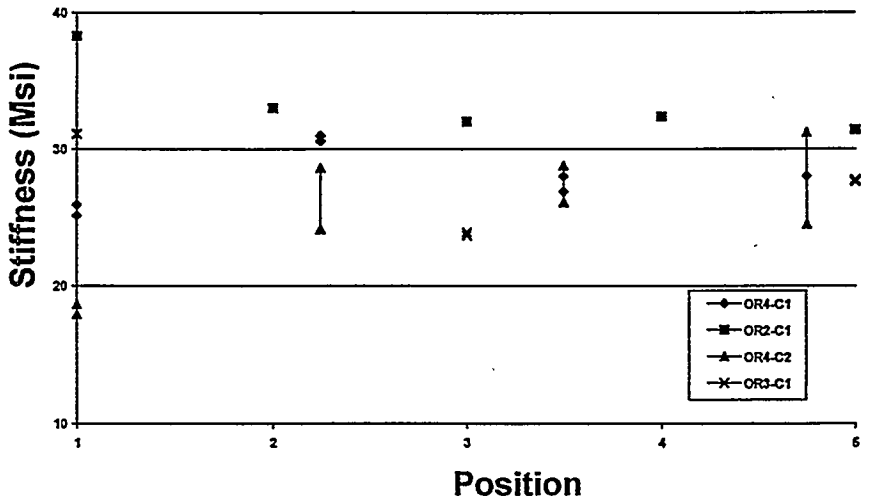

Figure 2. Modulus (Msi) versus axial position along tube, for four different tubes. Angular variations at fixed axial position are shown by multiple symbols.

rather large point-to-point variations along each tube and each tube shows distinct behavior. 3 of the 4 tubes exhibit a modulus which is either high or low (by as much as 50%) at one end of the tube, with mild variations away from the one end. The 4th tube, however, has a low modulus in the middle of the tube. The modulus at any axial location, but for angular locations differing by 90°, shows much smaller variations, indicating angular homogeneity at a fixed axial position

The observed modulus variations are generally attributable to variations in densification along the length, potentially caused by thermal gradients along the tube length during processing. Microscopy of high and low modulus regions indicate "low" and "high" degrees of porosity, respectively. These qualitative results are consistent with a correlation of modulus and density made by Becher et al. on similar F-CVI materials (Fig. 3).[3] Variations observed here, interpreted using Fig. 3, suggest variations in porosity from 10-25% along the length in these tube components.

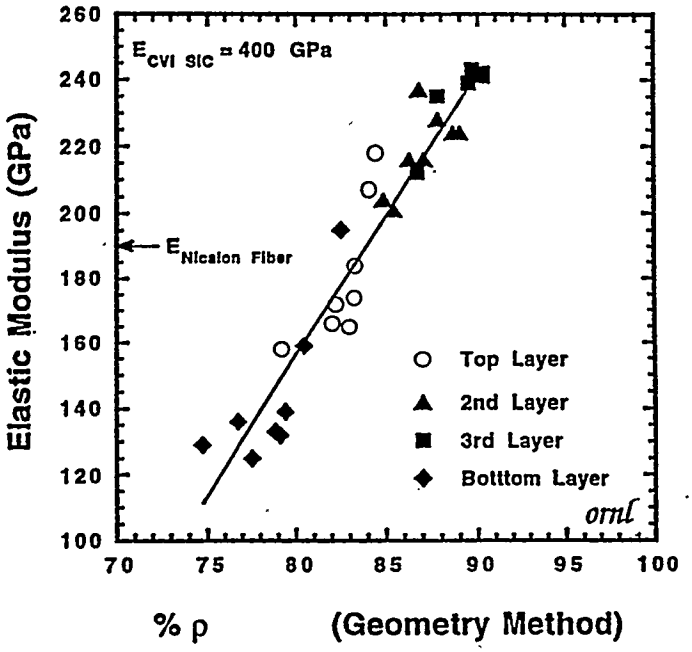

Figure 3. Modulus (Gpa) versus volumetric density (from Becher et al.)

Two tubes have been tested beyond the linear range. The stress-strain curves for the six pairs of strain gauges (two pairs at each of three locations) are shown in Fig. 4 for the one sample which failed in the gauge section at 137 Mpa (20.1 ksi). It is evident that the entire stress-strain response of the material is influenced by the local property variations, and that axial variations are more severe than angular variations. Table I shows the modulus, proportional limit stress and strain, strain at failure, and tangent modulus at failure, for the six pairs of gauges. The lower moduli regions exhibit a slight tendency toward lower proportional limit stresses. The softest region with the lowest σ_{pl} exhibited the largest strains up to failure. At failure, the strains differ by up to 25% from point to point. Near failure the tangent moduli are fairly constant with strain but again vary by 25%, at $\approx 28 \pm 5$ GPa. There is no apparent correlation between initial composite modulus and final tangent modulus, however. This overall behavior suggests that the initial response is controlled by matrix modulus and residual stresses whereas, after extensive cracking and non-linear reponse, the final response is much less dependent on matrix properties and is controlled primarily by the response of the fiber tows. For reference, the response of the 0° fibers alone

suggests a final tangent modulus of ½ $V_f E_f \approx 30$ GPa. Progressive damage to the fibers, followed by fiber slipping against the matrix, can cause the tangent modulus to be below ½ $V_f E_f$ and, in an ideal composite, to approach zero at composite failure. More detailed analysis of these results is presented in the following section.

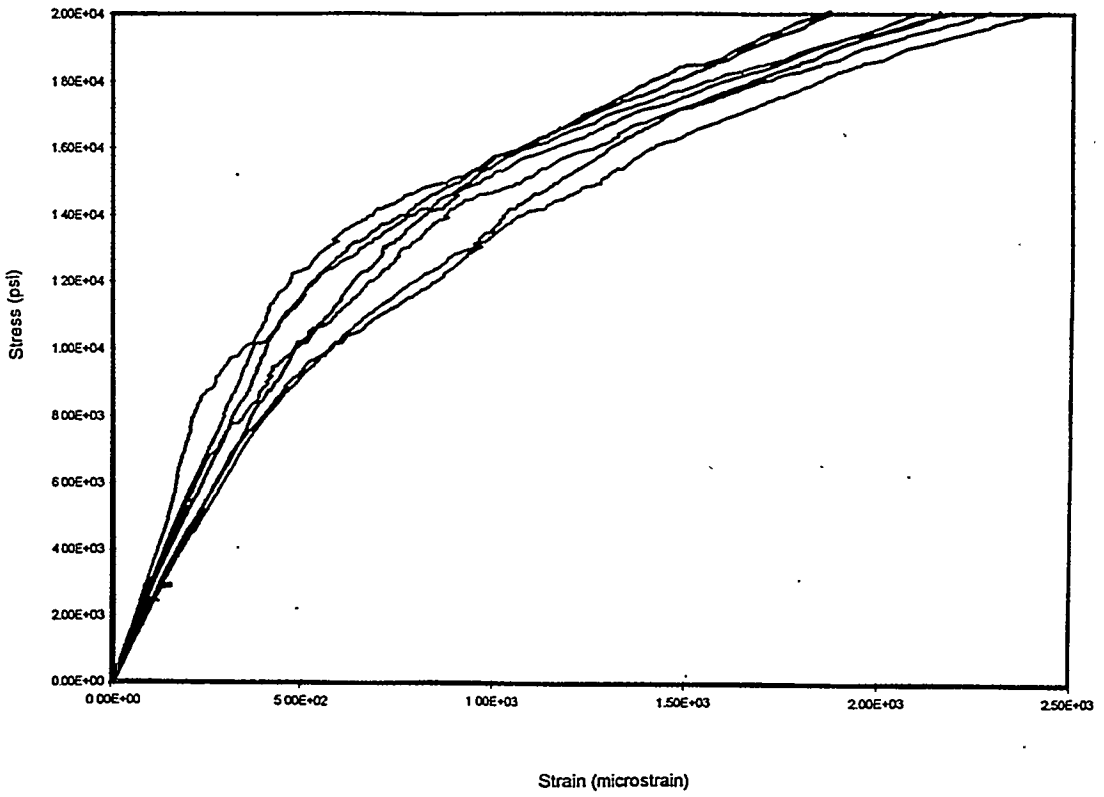

Figure 4. Stress-strain curves for six pairs of strain gauges on sample OR3-C1. Variations in the proportional limit and strain at failure are clearly evident.

Site	E (msi)	σ_{pl} (ksi)	ε_{pl} (microstrain)	$\varepsilon_{failure}$ (microstrain)	E_{final} (msi)
1 - front	29.8	9.1	300	2190	3.4
- back	31.05	5.0	151	2090	4.1
3 - front	23.9	3.1	140	2440	3.9
- back	23.0	6.3	287	2150	4.3
5 - front	27.3	6.9	259	2280	3.7
- back	28.5	4.0	150	1870	4.9

Table I. Initial modulus, porportional limit stress and strain, failure strain, and tangent modulus at failure (from 17.5 ksi to 20 ksi), for six pairs of strain gauges on tube OR3-C1.

III. ANALYSIS

Matrix Cracking

We first consider the observed variations in proportional limit stress, and any correlations with initial modulus. Due to bridging of cracks by the 0° fibers, Aveston, Cooper and Kelly showed that large cracks cannot propagate across the matrix of a uniaxial composite below a "matrix cracking stress" σ_{mc}, which therefore established a minimum proportional limit[4]. σ_{mc} is given by

$$\sigma_{mc} = \left[\frac{6\Gamma f^2 E_f E_c^2 \tau}{(1-f)E_m^2 r}\right]^{1/3} - q\frac{E_c}{E_m}$$

where f = 0° fiber volume fraction, E_f, E_c, E_m are fiber, composite and matrix Young's moduli, r is fiber radius, Γ is the matrix fracture energy, τ is the interfacial sliding resistance between fibers and matrix, and q is the residual tensile stress in the matrix. To utilize the above result in a porous-matrix composite with 90° fibers, the quantities E_m and Γ must be considered properties of an effective homogeneous matrix. We estimate E_m from the known E_f and measured E_c by a simple rule of mixtures:

$$E_c = fE_f + (1\text{-}f)\,E_m$$

where $f = \frac{1}{2} V_f$ in this case. The effective matrix fracture energy is the true matrix energy reduced by i) the porosity in the matrix, which is related to the true porosity as $V_p/(1\text{-}f)$, and ii) the surface area of the 90° fibers, which are assumed to be weakly bonded to the matrix because of the weak carbon interlayer. Hence,

$$\Gamma = \Gamma_{SiC}\left(1 - \frac{V_p + f}{1-f}\right)$$

V_p is obtained from the measured E_c using the correlation of Fig. 3. Predictions for σ_{mc} versus E_c can be made from the above, and here we use E_f = 190 GPa, τ = 25 MPa,[5] V_f = 0.32, $\Gamma^{SiC} = 1.0 \times 10^{-8}$ GPa - m. The result is $\sigma_{mc} \approx 90$ GMa = 13 ksi nearly independent of the matrix porosity or E_c. If residual thermal stresses exist, the proportional limit can be shifted down but q is not expected to vary with porosity, and so the shift does not, in fact, depend on either E_m or E_c. Thus, σ_{mc} can be reduced to smaller values but does not exhibit any strong correlation with E_c.

As an alternative to full matrix cracking, we also consider cracking around the 0° infiltrated fiber tows, with no slip at the tow-matrix interface[6]. This deformation mechanism corresponds to cracking around the tows and through the 90° tows without penetration into the 0° tows, and is analogous to the onset of tunnel cracking in the 90° plies of 0°/90° laminate composites. In this case, the onset of extensive cracking occurs at a stress

$$\sigma_{mc} = \left[\frac{f_T E_T E_c \Gamma \rho}{a E_m}\right]^{1/2}$$

where a is the fiber tow diameter, f_T is now the 0° tow volume fraction, E_T the tow modulus, E_m and Γ the modulus and fracture energy of the effective matrix material outside of the fiber tows and ρ a calculated parameter.[4] Assuming the fiber tows to be 60% fiber and fully densified with 40% SiC matrix, (E_{SiC} = 400 GPa) we have

$$E_T = 0.6\,E_f + 0.4\,E_{SiC}$$

and $f_T = f/0.6$. The remaining "matrix" material has a modulus E_m obtained again from

$$E_c = f_T E_T + (1-f_T) E_m$$

and the effective Γ is

$$\Gamma = \Gamma_{SiC}\left(1-\frac{V_p+f}{1-f_T}\right) .$$

The prediction of this model, with the parameter ρ ranging from 1.7 - 2.0 and a = 220 μm, (effective tow diameter) for the proportional limit versus E_c are also nearly independent of E_c or V_p and are σ_{mc} = 47 Mpa (6.8 ksi) . These values are somewhat lower than the ACK results, but still slightly higher than observed experimentally. Residual stresses could easily be the difference between these predictions and the observed range.

Considering these results, the onset of cracking and non-linear deformation in these materials may thus occur by formation of multiple small matrix cracks which initiate at large pores and grow across 90° tows but do not grow through or around the 0° tows. Normally such microcracks do not contribute substantially to the non-linear strain of the composite. But here the extensively distributed porosity may permit considerable local microcracking at low stresses. The microcracks would then grow into, at higher loads, fully-extended "matrix cracks" in the traditional sense. The initial cracking failure may thus mimic the response of very heterogeneous materials such as cements, and the onset of non-linearity would than be strongly coupled to the extent and size distribution of porosity. If this mechanism prevails, it is not accompanied by cracking of the 0° tows, and the 0° load-bearing fibers are not exposed to deleterious environmental degradation. The low proportional limit may then not be a design limit for long-term durability. This will be investigated in our future work.

Ultimate Strength

Ideally, the UTS is controlled by failure of the fiber bundles. The final tangent moduli shown in Table 1 are close to 1/2 $V_f E_f$ = 30 Gpa, suggesting that the system is controlled by the fiber loading at this point. Under the "Global Load Sharing" assumption widely successful in a number of other CMC materials, the UTS σ_u is predicted to be[7]

$$\sigma_u = \left(\frac{1}{2}V_f\right)\left(\frac{2}{m+2}\right)^{\frac{1}{m+1}}\left(\frac{m+1}{m+2}\right)\sigma_c$$

where σ_c is the in-situ fiber strength at a characteristic gauge length $\delta_c = r\sigma_c/\tau$ and m is the Weibull modulus describing the statistical variability in fiber strength around σ_c . Several recent studies have assessed the in-situ strength of Nicalon in CVI-SiC and found fiber degradation on processing with σ_c = 1.75 ± .25 GPa and m = 5 ± 1.[8] Using the median values suggests predicted strengths in the range of

$$\sigma_u \approx 195 \pm 35 \text{ MPa}$$

and a failure strain of

$$\varepsilon_f \approx \frac{\sigma_c}{E_f}\left(\frac{2}{m+2}\right)^{\frac{1}{m+1}} = 0.75 \pm 0.11\%$$

These values are larger than the observed strength and failure strain, particularly for the failure strain, and prompt us to consider below the strength of these materials in the presence of the unbridged matrix regions, which can cause stress concentrations and "premature" failure.

The stress concentrations on the fibers at the tips of unbridged matrix region (cracks) has recently been investigated by Xia et al.[9] They have found that, including fiber slip controlled by the interfacial τ, the fiber tensile stresses σ_f at the tip of a crack of diameter 2a are enhanced relative to the applied stress σ as

$$\sigma_f = \frac{\sigma}{V_f}\lambda(\eta)$$

where $\lambda(\eta)$ is a computed function of

$$\eta \approx \frac{3\pi V_f^2 E_f E_c}{V_m^2 E_m^2}\frac{a\tau}{r\sigma}$$

For 2-d cross-ply materials that approximate the present woven structure, the function λ is roughly linear. At $V_f = 0.40$, and $E_m = E_f$ (the only case calculated),

$$\lambda(\eta) \approx 2\left(1+\frac{1}{60}\eta\right) \qquad 0 < \eta < 30$$

Since $\sigma\eta$ is independent of σ, the fiber stress is increased by a fixed amount over the "global" load sharing value of $2\sigma/V_f$. To initiate failure, we must then have $\sigma_f \approx \sigma_c$ so that the applied failure stress is

$$\sigma_u = \frac{V_f}{2}\sigma_c - \frac{\sigma\eta}{60}$$

For "typical" intermediate porosity $V_p = 15\%$ and E_f, E_c, E_m, V_f, V_m, τ as given earlier, we find

$$\sigma_u = \frac{V_f}{2}\sigma_c - 0.11a(\mu m)\ \text{MPa}$$

The strength degradation is approximately linearly dependent on the "crack" size a. For 2a = 800 μm, a typical width of the interlaminar pore region (see Fig. 1) we obtain

$$\sigma_u = 236\ \text{Mpa}$$

which is larger than to the global load sharing prediction, suggesting that typical tow spacings/crack sizes

do not degrade strength. For a "high" porosity region with $V_p = 25\%$ ($E_c \approx 125$ Gpa), the stress concentrations increase, and

$$\sigma_u = \frac{V_f}{2}\sigma_c - 0.217a(\mu m)MPa\,.$$

With typical "crack" widths of 2a = 800σm, the predicted strength is

$$\sigma_u = 194 \text{ Mpa},$$

almost identical to the global load sharing result. However, if a width of 2a = 1200 μm (slightly larger than a tow length) occurs,

$$\sigma_u = 150 \text{ Mpa}$$

is predicted, a value approaching the measured value of 139 Mpa. Interestingly, the failure plane of the failed tube is quite close to the low-modulus region (position 3, $E_c = 159$ Gpa), which is consistent with the above estimate. Fluctuations in the microstructure which lead to local regions with both low density/modulus and in which the tow separation is somewhat larger than average could thus be responsible for the observed reduced strength.

The above predictions are only qualitative in the sense that they do not account for the fiber/matrix moduli differences; nor has the influence of multiple matrix cracks been considered, which tends to decrease stress concentrations. Also, uncertainty in the precise values τ and σ_c certainly exists. Further analysis of the fracture surfaces, in-situ fiber strengths, interfacial sliding τ, and microstructural variations will be carried out on the present materials to make these calculations more quantitative.

IV. Summary

The analysis of both σ_{mc} and σ_u indicates that local microstructural variations, such as porosity and tow spacing, can play an important role in determining the mechanical properties of these CMC materials. Such a situation is clearly undesirable in that, although tougher and exhibiting "graceful" failure, this composite tends to be controlled by "defects" as in a monolithic ceramic. In contrast, many other CMC materials exhibit behavior consistent with the theoretical predictions and are far less sensitive to matrix porosity and "damage" in various forms. Improved forced-CVI processing approaches are now being investigated to eliminate thermal gradients and large inter-laminar pores, and to improve the microstructure. Modified preform fabrication to increase fiber volume fraction and improve homogeneity will also improve mechanical performance. Interface manipulation is not clearly necessary at this stage: reducing τ reduces the matrix cracking stresses but can lessen stress concentrations and thereby improve ultimate strength; increasing τ might increase matrix cracking in better-densified materials but could also increase stress concentrations. The initial cracking in the present materials may not, however, expose 0° fibers and the carbon interface to external environments, and so durability at loads somewhat above the initial cracking loads may not be an issue. In any case, if processing defects can be better eliminated, as accomplished in traditional CVI SiC/SiC systems, the initial cracking events will be pushed up to higher stresses and these materials will be suitable for heat exchanges applications at moderate temperatures and loads.

REFERENCES

1. T. M. Besmann, B. W. Sheldon, R. A. Lowden and D. P. Stinton, "Vapor-Phase Fabrication and Properties of Continuous-Filament Ceramic Composites," Science, Vol. 253, 1104-1109 (1991).

2. W. A. Curtin, K. L. Reifsnider, L. L. S. Oleksuk and W. W. Stinchcomb, "Investigation of Properties and Performance of Ceramic Composite Components: Final Report on Phase II." Oak Ridge National Laboratory, October 31, 1994.

3. P. F. Becher and H. T. Lin, CFCC Program Bimonthly Progress Report, Feb.-Mar. 1994, pg. 37.

4. M. Sutcu and W. B. Hillig, "The Effect of Fiber-Matrix Debond Energy on the Matrix Cracking Strength and the Debond Shear Strength," *Acta metall. mater.* Vol. 38, 2653 (1990); B. Budiansky, J. W. Hutchinson and A. G. Evans, "Matrix Fracture in Fiber-Reinforced Ceramics," *J. Mech. Phys. Solids*, Vol. 34, 167, (1986).

5. E. Lara-Curzio, M. K. Ferber and R. A. Lowden, "The Effect of Fiber Coating Thickness on the Interfacial Properties of a Continuous Fiber Ceramic Matrix Composite," *Ceram. Eng. Sci. Proc., Vol.*15, 989 (1994).

6. This is analogous to the no-slip condition at the fiber-matrix interfaces, as discussed in Ref. 4.

7. W. A. Curtin, "Theory of Mechanical Properties of Ceramic-Matrix Composites," Journal of the American Ceramic Society, Vol. 74, 2837 (1991).

8. A. G. Evans, and F. W. Zok, "Review: The Physics and Mechanics of Fibre-Reinforced Brittle Matrix Composites." Journal of Materials Science, 29, 3857 (1994); D. Singh, J. P. Singh, M. J. Wheeler, "Mechanical Behavior of Sic(f)/SiC Composites and Correlation to In-Situ Fiber Strength at Room and Elevated Temperatures," Submitted to the Journal of the American Ceramic Society, January 1995.

9. Z. C. Xia, J. W. Hutchinson, A. G. Evans and B. Budiansky, "On Large Scale Sliding in Fiber-Reinforced Composites," in press (1993).

JOINING OF SiC CERAMICS AND SiC/SiC COMPOSITES

B. H. Rabin

Idaho National Engineering Laboratory
P.O. Box 1625
Idaho Falls, ID 83415-2218

ABSTRACT

This project has successfully developed a practical and reliable method for fabricating SiC ceramic-ceramic joints. This joining method has the potential to facilitate the use of SiC-based ceramics in a variety of elevated temperature fossil energy applications. The technique is based on a reaction bonding approach that provides joint interlayers compatible with SiC, and excellent joint mechanical properties at temperatures exceeding 1000°C. Recent efforts have focused on transferring the joining technology to industry. Several industrial partners have been identified and collaborative research projects are in progress. Investigations are focusing on applying the joining method to sintered α-SiC and fiber-reinforced SiC/SiC composites for use in applications such as heat exchangers, radiant burners and gas turbine components.

INTRODUCTION

SiC ceramics have considerable potential as elevated temperature structural materials in fossil energy applications. Ceramic-to-ceramic joining methods are needed to allow the fabrication of large or complex shaped parts, and ceramic-to-metal joining methods are needed to allow integration of ceramic components into existing engineering systems. Although considerable efforts have been devoted to understanding the processing, microstructures and properties of SiC-based structural materials, joining remains largely an unresolved issue, particularly with respect to elevated temperature applications. Ideally, joined components should exhibit mechanical properties (including reliability), elevated temperature capabilities and environmental resistance comparable to the base material. Furthermore, the joining method should be practical, cost effective and applicable to different types of SiC ceramics, including SiC fiber-reinforced composites.

This project has successfully developed a reaction processing method for fabricating SiC ceramic-to-ceramic joints [1,2]. The processing method involves tape casting thin sheet SiC+C interlayer precursors, clamping the tape between the SiC parts, and infiltrating the joint with molten Si to form a reaction bonded silicon carbide (RBSC) joint interlayer. This method is attractive since the interlayer material is compatible with SiC, and excellent room and elevated temperature mechanical properties can be achieved.

In addition, as with brazing, external pressure is not required, thus making the process inexpensive and practical compared to alternative joining methods. Details of the joining procedure as well microstructural and mechanical property characterization results have been described previously [1,2]. This paper reports on the status of technology transfer efforts involving a number of industrial partners.

PROGRESS STATUS

Laboratory Joining Studies

Recently, efforts have been made to demonstrate the applicability of the joining method to different joint geometries and materials. Figure 1 shows examples of several joined structures that were fabricated from sintered α-SiC using the laboratory scale localized induction heating apparatus at INEL. Of particular interest is the ability to fabricate tube-to-tube butt joints, since long ceramic tube structures are required in applications such as heat exchangers and radiant burners.

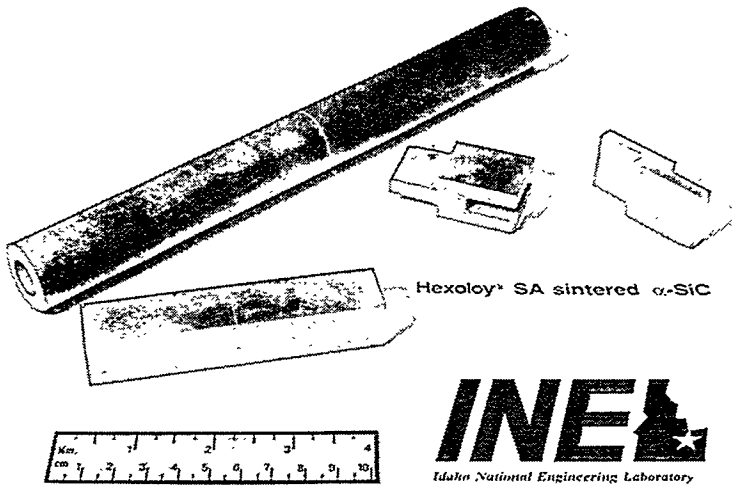

Figure 1. Examples of joined α-SiC structures produced using the reaction processing method developed under this project.

Technology Transfer Activities

Several industry contacts have been made and detailed discussions have taken place regarding industrial needs for the SiC joining methods in general, and the potential uses of the method developed under this program in particular. Table 1 lists the various industry contacts and the associated applications being explored. As a result of these discussions, several technology transfer activities are now in progress, as discussed below.

contact	material	applications
DuPont Lanxide Composites, Inc.	CVI SiC/SiC	gas turbines, radiant burners
Allied-Signal Aerospace	α-SiC	heat exchangers
Hague International	α-SiC, RBSC, SiC/$MoSi_2$	heat exchangers
Stone & Webster	α-SiC, SiC/SiC	reformers
Amercom, Inc.	SiC/SiC	heat exchangers, radiant burners, gas turbines
Textron Specialty Materials, Inc.	NBSC	heat exchangers, radiant burners, reformers
Dow Corning	SiC/SiCN	gas turbines, chemical pump

Table 1. Potential Industrial Uses for SiC Joining Technology

Cooperative work with DuPont Lanxide has been initiated under funding from the DOE Continuous Fiber Ceramic Composites (CFCC) Program. In this work, the joining method is being applied to CVI SiC/SiC composite materials for potential use in a variety of energy conversion devices including gas turbine components. These studies are examining the suitability of different joint configurations, and joint microstructures and properties are being studied at both INEL and DuPont Lanxide.

In another effort, a Phase I Joint Development Program is being carried out in collaboration with Allied Signal Aerospace Corp., a subcontractor to Foster Wheeler Development Corp., involved in the development of the Ceramic Air Heater for the DOE High Temperature Advanced Furnace. This work is being conducted under funding from

the DOE-PETC High Performance Power Systems Program. This work will apply the joining technique to sintered SiC, and specifically includes the fabrication and elevated temperature high pressure testing of tube-to-tube structures. A CRADA involving Allied-Signal and Carborundum is currently being negotiated.

A CRADA is also being negotiated with Hague International to investigate the fabrication of tube-to-tube joints for use in ceramic heat exchangers. This work will involve a variety of SiC-based materials, and seeks to improve the elevated temperature mechanical properties and corrosion resistance of the joints.

SUMMARY

Reaction processing methods have been developed for fabricating SiC-to-SiC joints for potential use at elevated temperatures. Technology transfer activities are in progress.

REFERENCES

1. B. H. Rabin and G. A. Moore, "Joining of SiC Ceramics and SiC/SiC Composites," ORNL/FMP-93/1, Oak Ridge National Laboratory, July 1993, pp. 33-42.

2. B. H. Rabin and G. A. Moore, "Reaction Processing and Properties of SiC-to-SiC Joints," Mat. Res. Soc. Symp. Proc., Vol. 314, 1993, pp. 197-203.

COMPARISON OF HIGH TEMPERATURE MECHANICAL PROPERTIES OF TWO MONOLITHIC SiC CERAMICS AND AN Al_2O_3 / SiC COMPOSITE

Kristin Breder

Oak Ridge National Laboratory
High Temperature Materials Laboratory
Oak Ridge, TN 37831-6069

ABSTRACT

Fast fracture strength, slow crack growth, and creep properties have been evaluated for three ceramics in air at room temperature and two elevated temperatures. The ceramics are candidate materials for heat exchangers in fossil energy systems, therefore, retained strength after coal ash exposure was also measured. At 1100°C the ceramics had acceptable mechanical properties, but two of them exhibited strength loss due to coal ash corrosion. At 1400°C creep and slow crack growth were observed in two of the materials, and the material which exhibited best resistance to coal ash showed unacceptably high creep rates.

INTRODUCTION

The purpose of this project is to compare structural ceramic materials proposed for use in the air heater of a coal fired high temperature advanced furnace (HITAF) for power generation. This work will provide necessary initial structural ceramic parameters for design of a prototype system. Two teams are currently funded by Pittsburgh Energy Technology Center (PETC) under the Combustion 2000, Phase 1, program to develop such a system. One team is led by the United Technologies Research Center, and the other team is led by Foster Wheeler Development Corporation[1, 2] Proposals for Phase 2 and 3 of the Combustion 2000 are currently under evaluation by DOE. Phase 2 will be engineering development and testing, consisting of subsystem and materials testing, and Phase 3 will consist of the detailed design, construction, operation, and evaluation of a prototype plant. The work presented here consists of evaluation of the mechanical properties of three structural

ceramics at high temperatures in air and a preliminary evaluation of mechanical properties of these structural ceramics after exposure to coal ash.

MATERIALS AND EXPERIMENTAL PROCEDURE

The following properties were measured for use as base line data: (1) Fast fracture strength at room temperature, 1100, and 1400°C; (2) Statistical analysis in the form of a Weibull analysis; (3) Necessary fractography; (4) Slow crack growth properties evaluated by the dynamic fatigue method; and (5) Creep/creep-rupture effects measured through interrupted static fatigue experiments. Initial corrosion experiments were performed in cooperation with the University of North Dakota Energy and Environmental Research Center (UNDEERC), where ORNL performed fast fracture measurements of corroded specimens.

For the mechanical properties measurements three materials have been compared. These are β-SiC from Coors Ceramics Company, NT230 siliconized SiC from Saint-Gobain/Norton and Lanxide DIMOX $SiC_{particulate}/Al_2O_3$ from DuPont Lanxide Composites. β-SiC is sintered silicon carbide with a fine grain structure and high density. NT230 SiC is siliconized silicon carbide and contains free silicon alloy (8 vol%) and some residual porosity. The SiC_p/Al_2O_3 which is manufactured by the Lanxide Direct Oxidation process (DIMOX) contains 48 vol% SiC_p, 38 vol% Al_2O_3 and 13 vol% Al-alloy, and some residual porosity. The SiC ceramics were tested as machined while the Lanxide DIMOX was reoxidized by the manufacturer after machining. For the corrosion studies the β-SiC was replaced (due to limited availability) by an α-SiC from the Carborundum Company, and an experimental grade of the Lanxide DIMOX material which was not reoxidized before the test was included.

The fracture strength of ceramic materials is most commonly measured in four-point flexure.[3] In this test, a specimen of 4x3x50 mm is subjected to bending in a fixture providing an inner span of 20 mm and an outer span of 40 mm. The specimen is loaded to fracture while load and deflection are monitored, and the flexure strength is calculated according to standard beam theory. The high temperature fixtures were SiC fixtures with pins that were free to rotate. The experiments were carried out in the flexure test system (FTS) which is a hydraulic system with SiC push rods in load control. The flexure method offers the possibility of testing a large number of samples at a reasonable cost, and, since the load train arrangement is relatively simple, three specimens may be tested simultaneously in the furnace.

Weibull analysis is the statistical tool most commonly used to analyze fracture data for structural ceramics.[4] Due to the brittle nature of ceramic materials, the fracture strength of a set of specimens may vary as much as 100% from the average strength,

necessitating a statistical analysis of the data. The Weibull modulus, m, and the Weibull scaling factor, σ_0, were obtained by the maximum likelihood method.[5,6]

The term "fatigue" as used for structural ceramics is different from that commonly used for metals. For ceramics the term fatigue is often used to describe the decrease in strength due to the combined action of *static* stress and degrading environment. The mechanism which causes this is known as slow crack growth (SCG) and is the growth of small preexisting cracks or voids at stress levels less than those needed to cause catastrophic failure. This happens because the individual atomic bond strength is decreased by exposure to certain environments. Eventually, a small crack will grow to a size large enough to cause catastrophic failure at a given stress level. In order to predict the lifetime for components in a given environment, the velocity at which cracks grow under a given stress and specific environment must be known.[7, 8]

Flexure creep tests were carried out in four-point bending in fixtures as described above. Two types of tests have been done; static tests at a fixed load for 300 hours and stepped loads of 100 h duration each. The static tests were performed at 1400°C, i.e. the temperature at which creep was observed in the dynamic fatigue experiments, and the loads were chosen such as to correspond to 25% and 70% of the fast fracture strength at that particular temperature. The stepped tests were carried out at 1200, 1300 and 1400°C at loads corresponding to stress levels of 50 MPa, 100 MPa, 150 MPa and so on up to 250 MPa (i.e. 500 h) or to failure. For these tests two of the three stations were loaded with fixtures and specimens while the third station was loaded with a dummy fixture only.

As a first approximation and for comparison between the materials and with previous experiments[9,10] the analysis by Hollenberg et al.[11] was used.

RESULTS AND DISCUSSION

Fast fracture of the unexposed materials as a function of temperature is shown in Fig. 1. The Weibull distributions of the three materials are shown in Figs. 2, 3, and 4 for room temperature, 1100, and 1400°C, respectively. The measured strengths as a function of stressing rate are shown in Figs. 5 and 6 for the three materials at 1100°C and 1400°C, respectively.

NT230 at 1400°C was the only material-temperature combination which showed any strength degradation over time and the SCG parameter n was calculated to be equal to 15.5[12] The Lanxide DIMOX material could only be tested up to stressing rates of 0.01 MPa/s at 1400°C because at the slower stressing rates creep became so pronounced that the four-point flexure fixtures could no longer accommodate the specimens. Also, at the 0.01 MPa/s stressing rate the creep was measurable, so the strength values calculated according to beam theory overestimate the strength of Lanxide DIMOX at this condition.

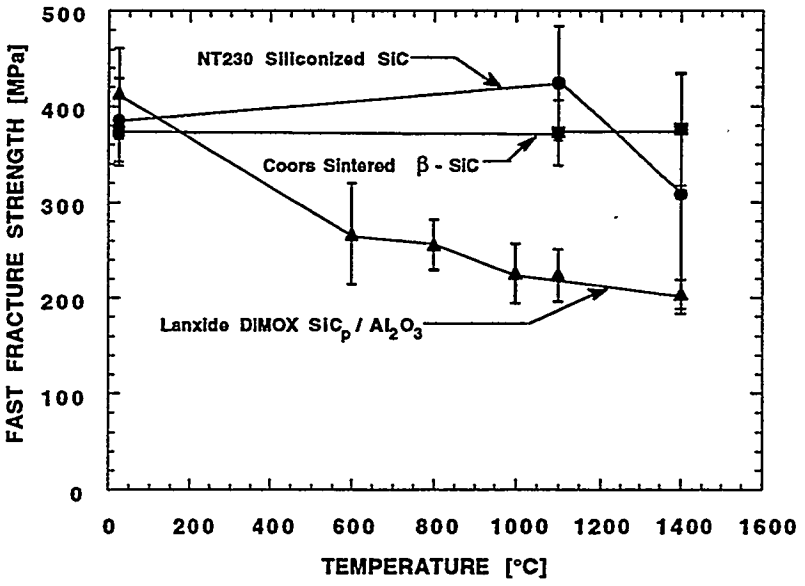

Figure 1. Fast fracture strength as a function of temperature for NT230 SiSiC, sintered β-SiC and Lanxide DIMOX.

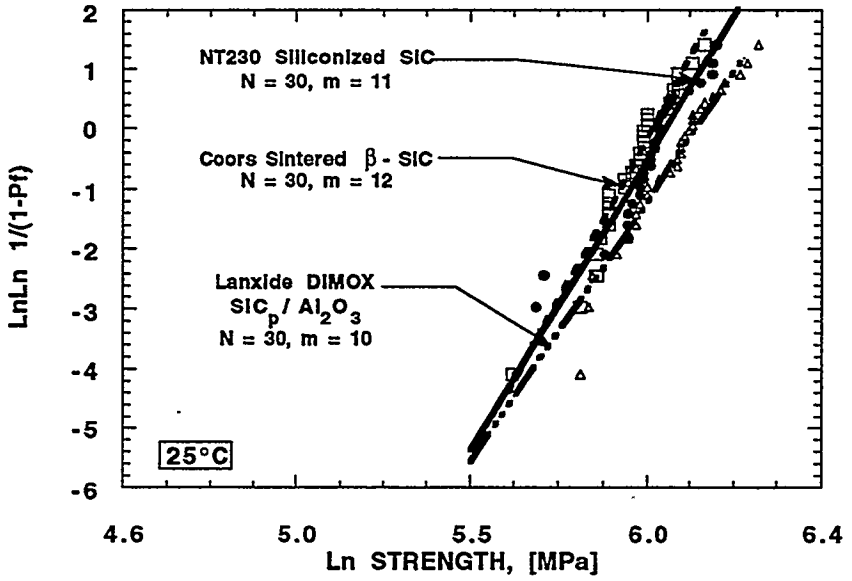

Figure 2. Weibull distribution of the room temperature fast fracture strength for NT230 SiSiC, sintered β-SiC and Lanxide DIMOX.

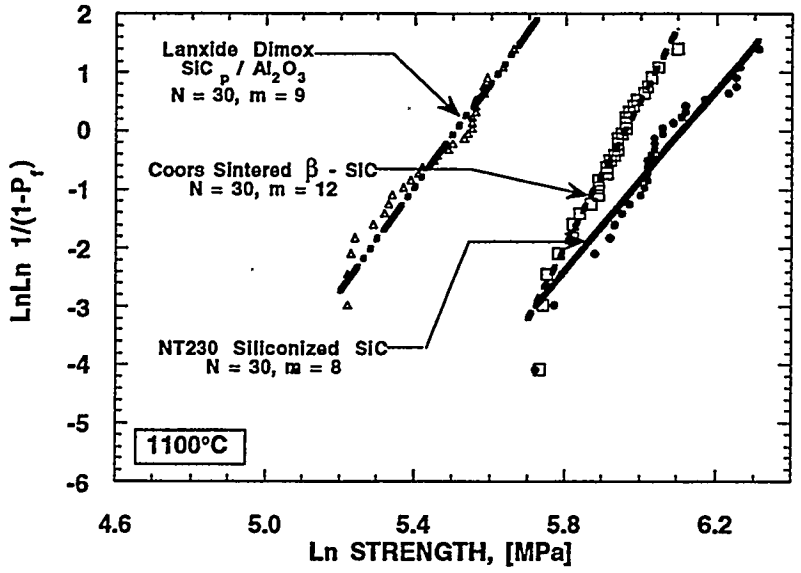

Figure 3. Weibull distribution of the 1100°C fast fracture strength for NT230 SiSiC, sintered β-SiC and Lanxide DIMOX.

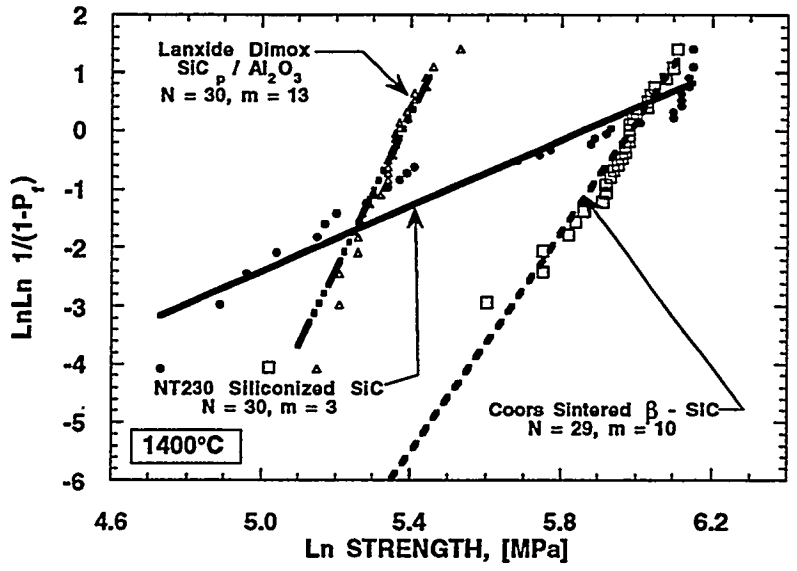

Figure 4. Weibull distribution of the 1400°C fast fracture strength for NT230 SiSiC, sintered β-SiC and Lanxide DIMOX.

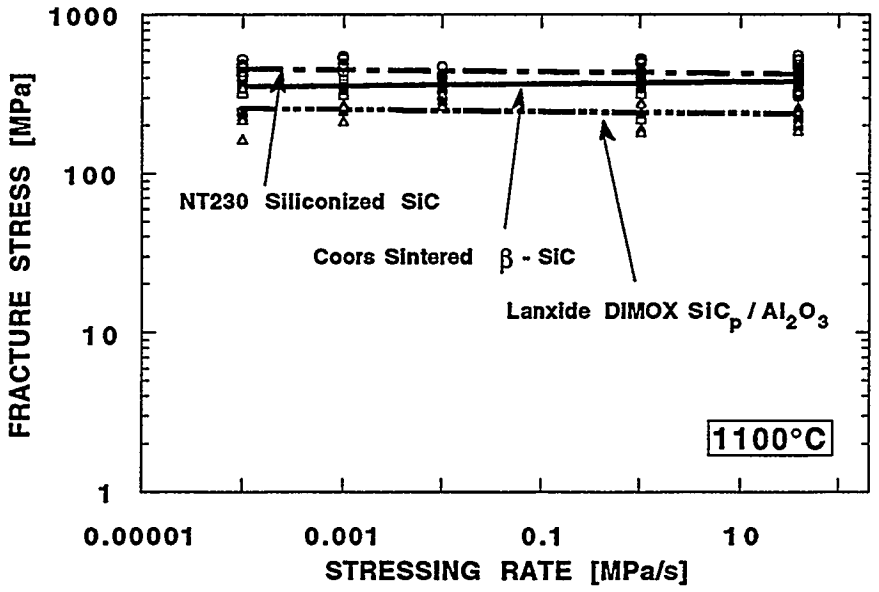

Figure 5. Strength as a function of stressing rate at 1100°C for NT230 SiSiC, sintered β-SiC and Lanxide DIMOX.

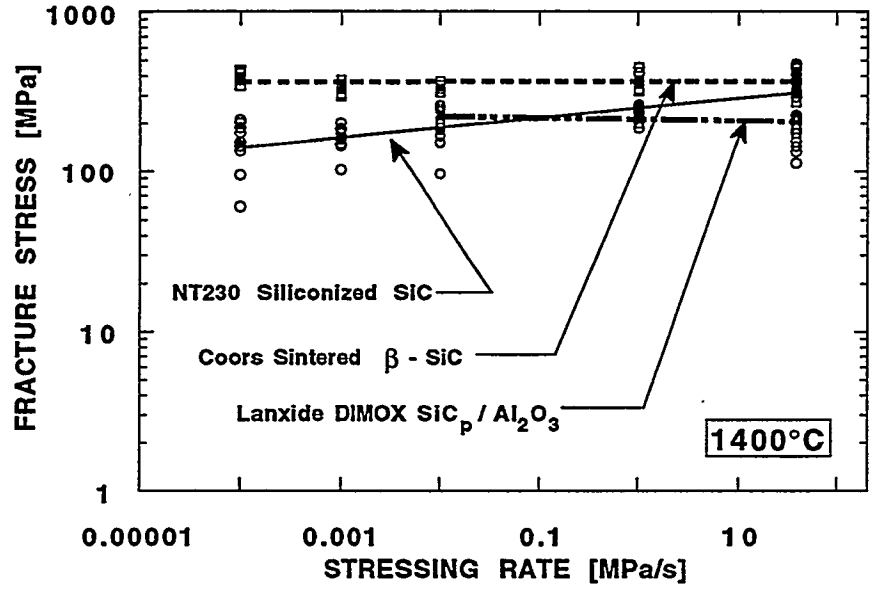

Figure 6. Strength as a function of stressing rate at 1400°C for NT230 SiSiC, sintered β-SiC and Lanxide DIMOX.

The fractography results confirmed the dynamic fatigue results. In general the failure mode for Coors β-SiC was fast fracture from pores in the microstructure, and this did not change as a function of stressing rate or temperature. Lanxide DIMOX failed in general from metal rich areas, but at 1400°C at the slower stressing rates creep became pronounced and the specimens failed due to accumulated creep damage. NT230 was delivered to ORNL in two batches, probably with a slight difference in Si - alloy content or composition. At room temperature and at 1100°C the failure modes for both batches were similar; fast fracture from pores in the microstructure. At 1400°C there was a clear difference between the two batches in the fast fracture test; one batch failing from a combination of pores and metal-rich inclusions, the other failing from pores as was observed at the lower temperatures. At the slower stressing rates where strength degradation was observed, the specimens failed from pore-like cracks (often containing metal-rich inclusions) that had grown in size during the test, and the batch difference became insignificant.

The base line strength of the three ceramics under consideration as a function of temperature was as expected. The Coors β-SiC showed no strength reduction at the temperatures under consideration, while the two other materials exhibit a drop in strength at the temperatures where the metal in these materials softens and melts. The Weibull analyses of the three ceramics reveal some important differences. At room temperature both the Weibull modulus and characteristic strength are comparable for the three materials, as can be seen in Fig. 2. At the elevated temperatures, however, it is seen that the Weibull modulus stays relatively unchanged for Lanxide DIMOX and Coors β-SiC, while for NT230 a gradual reduction of the Weibull modulus is seen. At 1400°C the Weibull modulus was m = 2.8, an unacceptably low value for a structural material. The lower Weibull modulus at 1100 and 1400°C for NT230 is due to the variability in the size of pores in the material and due to the fact that the NT230 was delivered in two batches with slight difference in Si-alloy content or composition. This effect is most pronounced at 1400°C as seen in the fast fracture results. Microstructural and fractographic investigations revealed differences in fracture initiating flaws between the batches, see ref. 12.

The dynamic fatigue experiments, shown in Figs. 3 and 4, show that there is no strength reduction with time at 1100°C for any of the ceramics. At 1400°C a pronounced strength reduction is seen for NT230. This strength reduction is due to the subcritical growth of pore-like cracks, often containing metal rich inclusions.

The stepped load deflection data typically look as shown in Fig. 7, where the load point deflection data corrected for the deflection in the dummy fixture are shown as a function of time for Lanxide DIMOX at 1400°C. As can be seen the creep does not reach a constant rate during the 100 hours, and as can be seen from Fig. 8 a steady state creep rate is not achieved even after 300 h at a constant stress. The deflection rates at the various stress levels were therefore obtained as the slope of the deflection curve towards the end of the 100 h test interval. A thorough description of the creep measurements will be reported elsewhere.[13]

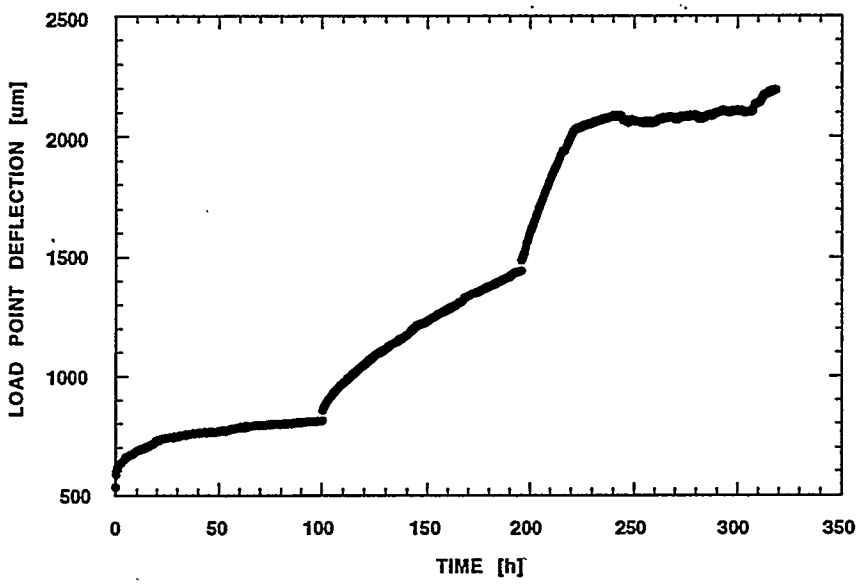

Figure 7. Load point deflection for a Lanxide DIMOX flexure bar stressed for 100 h each in increments of 50 MPa at 1400°C. The flattening out of the curve after approximately 220 h indicates that the specimen reached the bottom of the fixture.

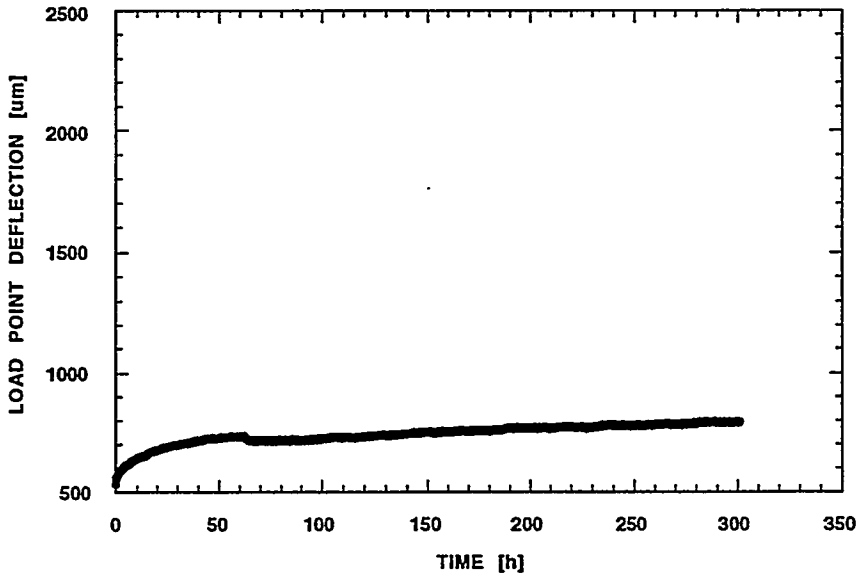

Figure 8. Load point deflection for a Lanxide DIMOX flexure bar stressed at 50 MPa for 300 h at 1400°C.

The materials exposed to coal ash at UNDEERC were fractured at room temperature in four point flexure. The resulting fracture strengths are shown in Fig. 9. The coal ash exposure experiments show several important features. The present experiments were intended as an initial set of conditions to compare several materials, coal slags and temperatures. By exposing the ceramics to static coal slag in a muffle furnace, significantly different levels of corrosion attack were observed, and reduction in strength values was observed for some of the combinations of ceramics, coal ash and temperature. The subsequent fractography showed that the materials which experienced a strength reduction also had a change in failure mode and that the coal ash in some cases produces severe corrosion pits. The material which had strengths that were unaffected by the exposure (Lanxide DIMOX) failed in a similar manner before and after exposure. A thorough discussion of the strength degradation and coal ash corrosion mechanisms can be found elsewhere.[14,15 16]

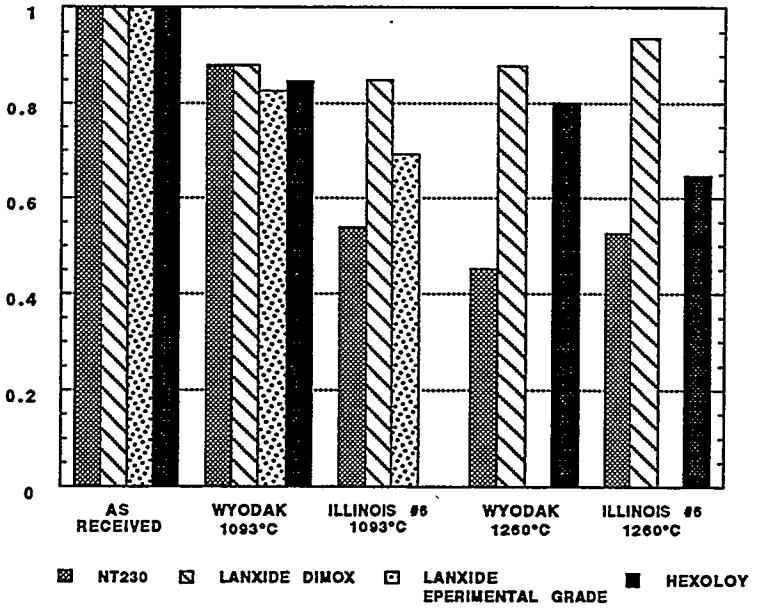

Figure 9. Retained fast fracture flexure strength in percent of the as received strength for specimens tested after exposure to Wyodak and Illinos #6 coal ash at 1093°C and 1260°C.

SUMMARY

The results show that the unexposed Coors β-SiC had good mechanical properties at the two temperatures considered. No SCG was observed during testing

times up to 1000 h at 1400°C. This material was, however, not tested for coal ash corrosion, but the very similar α-SiC showed strength degradation after coal ash exposure. The unexposed Lanxide DIMOX material showed loss of strength at 600°C, and considerable creep was observed at 1400°C. At 1100°C, the material showed no SCG or creep during the dynamic fatigue experiment. The Lanxide DIMOX withstood the corrosive coal ash environment well, and experienced only insignificant loss of strength after 300 h of coal ash exposure. Unexposed NT230 had good mechanical properties at 1100°C with a reasonable strength and no SCG. At 1400°C, however, the ceramic showed loss of strength and SCG. This ceramic was attacked by both coal ashes at both experimental temperatures.

The present results have implications for the proposed application, i.e. high temperature heat exchangers. The creep rates for Lanxide DIMOX at 1400°C are quite high, and in a design where even moderate localized stresses will occur, the components may be out of tolerance in an unacceptably short time. However, at 1200°C both the magnitude of the strain rates and the creep exponent are considerably lower, and this temperature may constitute a possible design temperature for this material. However, in order to ensure a reliable estimation of the life-time of components at this temperature, further measurements will be needed. Creep in tension and compression should be performed, as well as time to failure experiments in tension. It is further necessary to investigate the creep and long time failure mechanisms for the temperatures under consideration. The NT230 SiSiC exhibited improved creep properties compared to similar siliconized silicon carbides.[17,18] Especially at 1200 and 1300°C the material exhibited very little creep. At 1400°C some creep was measured, and further measurements in tension might be warranted also for this material. It is, however, important to keep in mind that the NT230 exhibited SCG at 1400°C, and strength degradation after coal ash exposure. The result may be an unacceptable short lifetime at 1400°C because of this.

Future research needs to concentrate on establishing the properties of the materials under a combined action of stress and environment. The various coal ashes have different viscosities at different temperatures, and temperature regimes must be established in which the combination of mechanical properties and corrosion resistance will give the specific ceramic under consideration an appropriate lifetime.

ACKNOWLEDGMENTS

Research sponsored by the U.S. Department of Energy, Office of Fossil Energy, Pittsburgh Energy Technology Center, Advanced Combustion Technology Program, DOE/FE AA 20 10 00 0, and Advanced Research and Technology Development Materials Program, [DOE/FE AA 15 10 10 0, Work Breakdown Structure Element

ORNL-1(G)] under contract DE-AC05-84OR21400 with Martin Marietta Energy Systems, Inc.

REFERENCES

1. D. J. Seery et al., "Engineering Development of Coal-Fired High -Performance Power Generation Systems," pp 188-195 in Proceedings of the Eighth Annual Coal Preparation, Utilization, and Environmental Control Contractors Conference, U.S. DOE, Pittsburgh Energy Technology Center, Pittsburgh, PA, 1992.

2. J. Shenker, "Development of a High-Performance Coal-Fired Power Generating System with a Pyrolysis Gas and Char-Fired High Temperature Furnace," pp. 183-187 in Proceedings of the Eighth Annual Coal Preparation, Utilization, and Environmental Control Contractors Conference, U.S. DOE, Pittsburgh Energy Technology Center, Pittsburgh, PA, 1992.

3. ASTM C 1161, "Standard Test Method for Flexural Strength of Advanced Ceramics at Ambient Temperature."

4. W. A. Weibull, "A Statistical Theory of the Strength of Materials," Ingeniørsvetenskapsakademien Handlingar, No. 151, Stockholm, Sweden, 1939.

5. W. Nelson, Applied Life Data Analysis, J. Wiley & Son, New York, NY, 1982.

6. K. Breder and V. J. Tennery, "Comparison of the Dynamic Fatigue Behavior of Two Monolithic SiC Ceramics and an Al_2O_3/SiC Composite," to be published in Ceramic Engineering Science Proceedings, **15** [4] 23-31, 1994.

7. S. M Wiederhorn, "Subcritical Crack Growth in Ceramics'" pp. 613-646 in Fracture Mechanics of Ceramics, Vol. 2, R. C. Bradt, D. P. H. Hasselman and F. F. Lange, Eds., Plenum Press, New York, NY, 1974.

8. J. E. Ritter, "Engineering Design and Fatigue Failure of Brittle Materials'" pp. 667-687 in Fracture Mechanics of Ceramics, Vol. 4, R. C. Bradt, D. P. H. Hasselman and F. F. Lange, Eds., Plenum Press, New York, NY, 1978.

9. H. T. Lin and P. F. Becher, "Creep behavior of a SiC-Whisker-Reinforced Alumina," *J. Am. Cer. Soc.* **73** [5] 1398-81 (1990).

10. H. T. Lin and P. F. Becher, "High-Temperature Creep Deformation of Alumina-SiC-Whisker Composites," *J. Am. Cer. Soc.* **74** [8] 1886-93 (1991).

11. G. W. Hollenberg, G. R. Terwilliger, and R. S. Gordon, "Calculation of Stress and Strain in Four-Point Bending creep Tests," *J. Am. Cer. Soc.* **54** [4] 196-99 (1971).

12. K. Breder, "Time-Dependent Strength Degradation of a Siliconized Silicon Carbide Determined by Dynamic Fatigue," accepted for publication in Journal of the American Ceramic Society, 1995.

13. K. Breder and H. T. Lin, "Creep Deformation of an Alumina-Silicon Carbide-Particulate Composite," manuscript in preparation, 1995.

14. T. M. Strobel, J. H. Hurley, "Coal-Slag Corrosion of SiC-Based Ceramics in a Combustion Environment," published in the Proceedings from the Am. Cer. Soc. PAC RIM Meeting, Nov. 1993.

15. T. M. Strobel, J. P. Hurley, K. Breder and J. E. Holowczak, "Coal-Slag Corrosion and Strength Degradation of Silicon Carbide-Alumina Composites," to be published in Ceramic Engineering Science Proceedings, 1994.

16. K. Breder, J. P. Hurley, T. M. Strobel and J. E. Holowczak, "Strength Degradation of Monolithic SiC and Al_2O_3 / SiC Composites After Exposure to Coal Slag," submitted to the Journal of the American Ceramic Society, 1995.

17. T-J. Chuang and S. M. Wiederhorn, "Damage-Enhanced Creep in a Siliconized Silicon Carbide: Mechanics of Deformation," *J. Am. Cer. Soc.* **71** [7] 595-601 (1988).

18. S. M. Wiederhorn, D. E. Roberts, T-J. Chuang, and L Chuck, "Damage-Enhanced Creep in a Siliconized Silicon Carbide: Phenomenology," *J. Am. Cer. Soc.* **71** [7] 602-608 (1988).

FACTORS AFFECTING THE CORROSION RATES OF CERAMICS IN COAL COMBUSTION SYSTEMS

John P. Hurley
Energy & Environmental Research Center
University of North Dakota
PO Box 9018
Grand Forks, ND 58202-9018

ABSTRACT

The concentrations of approximately a dozen elements in the products of coal combustion affect the corrosion rates of ceramics used to construct the combustion system. The elements, including H, O, Na, Mg, Al, Si, P, S, Cl, K, Ca, and Fe, affect corrosion rates in three ways: as primary corrodants of the materials, as secondary corrodants that affect the activities of the primary corrodants, and by affecting the mass transport rate of the primary corrodants. A full factorial study of corrosion rates performed by varying the concentrations of these elements would involve X^n tests, where X is the number of variations of each element and n is the number of different elements. For three variations (low, medium, and high concentrations) of each of 12 elements, the number of tests is 531,441 for a single temperature and pressure condition. The numbers can be reduced with the use of a fractional factorial test matrix, but the most effective way to perform corrosion tests is to base them on realistic system conditions. In this paper, the effects of the composition and physical state of the products of coal combustion on ceramic corrosion rates are given along with suggestions of appropriate test conditions for specific system components.

INTRODUCTION

To increase national energy self-sufficiency for the near future, energy systems will be required to fire low-grade fuels and use more efficient energy cycles than those available today. The coal-fired steam cycle used at present is limited to a maximum steam temperature of 550°C and, thus, a conversion efficiency of 35%. Higher working-fluid temperatures are required to boost efficiency. This means that subsystems will be exposed to much more corrosive environments than those currently used. Problems of special concern are corrosion and fatigue of directly fired turbine blades, corrosion and blinding of hot-gas cleanup filters, and catastrophic failure of high temperature heat exchangers. To prevent those structures from failing will require the use of advanced materials, particularly ceramics, for construction.

Silicon- and alumina-based ceramics are most often considered for the construction of large subsystems because of their relatively low cost and familiarity. However, only a few studies have been performed with the materials in actual coal combustion environments.[1] Testing is made especially difficult because of the complexity of a coal combustion environments and the great variability in coal composition.

In this paper, we describe fuel and operational factors that affect the corrosion rates of structural ceramics in coal-fired combustor systems, with examples of the corrosion of silicon carbide-based materials. We focus in particular on two subsystems, hot-gas particulate filtration and high-temperature heat exchangers. The objective of the paper is not to present specific data on rate factors, but to help the experimentalist measuring these factors to better design their tests.

FACTORS AFFECTING THE COMPOSITION OF ASH DEPOSITS

All surfaces of a coal-fired combustor upstream of particulate removal systems are quickly covered with ash. The composition of the ash deposits depends on the composition of the coal, the mechanisms of ash deposition, and the temperature of the deposits.

Coal-Related Factors

Coal is composed primarily of carbon, lesser amounts of heteroatoms such as hydrogen, oxygen, sulfur, and nitrogen, and ash-forming constituents such as mineral matter and organically associated alkali and alkaline-earth cations. The quantity and form of the major elements in the coal are determined by the depositional environment of the original coal-forming plants, and the interaction of the buried material with groundwater both before and after coalification.

Coals from the eastern United States are typically high-rank coals that form ash from microscopically observable mineral grains. The most prevalent minerals in U.S. coals are quartz (SiO_2), kaolinite ($Al_2Si_2O_5[OH]_4$) and other aluminosilicate clays such as montmorillonite ($[Al,Mg]_8[Si_4O_{10}]_3[OH]_{10}\cdot 12H_2O$) and illite ($KAl_5Si_7O_{20}[OH]_4$), and pyrite ($FeS_2$). These minerals are rich in silicon, aluminum, and iron, so the coal ashes are alkaline. Coals from the western United States also contain these minerals, but they are primarily lower-rank coals that have undergone less lithification than the eastern coals and so contain much more oxygen in their organic structures. The oxygen is commonly present in carboxylic acid functional groups. During interaction with groundwater, these acids can undergo ion exchange to fix sodium, potassium, magnesium, and calcium in an atomically disbursed form within the organic structure. The addition of the alkali metal and alkaline-earth elements to the ash make it much more alkaline than eastern coal ash.

Because of the large range of depositional environments, degrees of coalification, and interactions with groundwater, U.S. coal ashes have a wide range of compositions. Table 1 shows the range as given in a standard text on coal-fired energy systems[2]. This wide range of coal ash compositions requires the materials experimentalist to consider specific coals that may be used in the energy system of interest.

Table 1. Coal-Ash Chemical Composition Ranges

Oxide Component	Percentage
SiO_2	10–70
Al_2O_3	8–38
Fe_2O_3	2–50
CaO	0.5–30
MgO	0.3–8
Na_2O	0.1–8
K_2O	0.1–3
SO_3	0.1–30

Factors Related to Ash Deposition Mechanisms

In addition to the type of coal that may be used in the energy system, the experimentalist must consider which fractions of the ash will come in contact with the ceramic. This information is best obtained experimentally, although approximations can be made based on extensive testing performed at utility boilers. During combustion of the coal, the minerals can vaporize, fragment, or coalesce depending on the initial association of the mineral with the coal, on the temperature and gas composition of the local combustion environment, and on the morphology of the original mineral grains. In general, mineral grains that are included within coal particles will experience temperatures 200°–300°C higher and much more reducing environments than the excluded mineral grains that were separated from the carbonaceous particles during processing. The included minerals commonly fuse with other mineral grains in the particle to form larger, much more compositionally complex ash particles. The excluded mineral grains are much less likely to interact with other mineral grains and will experience lower temperatures and more oxidizing atmospheres than the included mineral grains. In such situations, they may be much more likely to fragment to form smaller ash particles than the original mineral.

In contrast to the mineral grains, the organically associated elements vaporize during combustion and become extremely reactive. The alkaline-earth elements rapidly oxidize to form submicron ash particles on the surface of the burning char particle. These can be shed as oxide particles or coalesce with quartz- and clay-derived ash to form complex aluminosilicates[3,4]. In contrast, the vaporized alkali metals exist as gaseous sulfates, hydroxides, and chlorides that can condense far downstream of the fireball. The vaporization and subsequent condensation of the organically associated elements causes them to concentrate in smaller ash particles.

The size and composition interdependence in the ash means that the composition of the ash depositing on and possibly corroding the material of interest depends on the local gas flow

conditions. If the object of interest is a tube placed directly in the gas flow, then larger ash particles will separate from the gas flow and strike the tube as they diverge around it, while the smaller ash will stay entrained with the gas. Figure 1 illustrates this concept. It compares the compositions of an ash deposit formed at 2100°F on the upstream side of a steam tube with four aerodynamic size-ranges of particulate ash collected from the boiler at the same location as the deposit. The boiler was firing a high-calcium subbituminous coal at the time. The bulk composition of deposit shows that it is formed primarily from particles with aerodynamic diameters of over 10 μm. The most striking variations in elemental concentration versus ash particle size occur for silicon and calcium. The average concentration of silicon in the ash particles is directly related to particle size whereas the average concentration of calcium is inversely related. This characteristic of the ash is typical of most high-calcium U.S. coals.

Figure 2 shows the compositions of another type of ash deposit along with aerodynamically sized ash collected in the vicinity. This type of deposit also forms on the upstream sides of steam tubes when firing high-calcium coals but forms at temperatures below approximately 1700°F. A comparison of the compositions shows that these deposits form predominantly from particles with aerodynamic diameters below 3 μm and so are much enriched in calcium and depleted in silicon. Materials prone to calcium corrosion would be much more severely attacked by this type of deposit than by the first. In addition, Figure 2 shows that the deposit contains a high level of sulfur, and that the sulfur condenses after ash deposition. The sulfur also can be quite corrosive, especially to alloys.

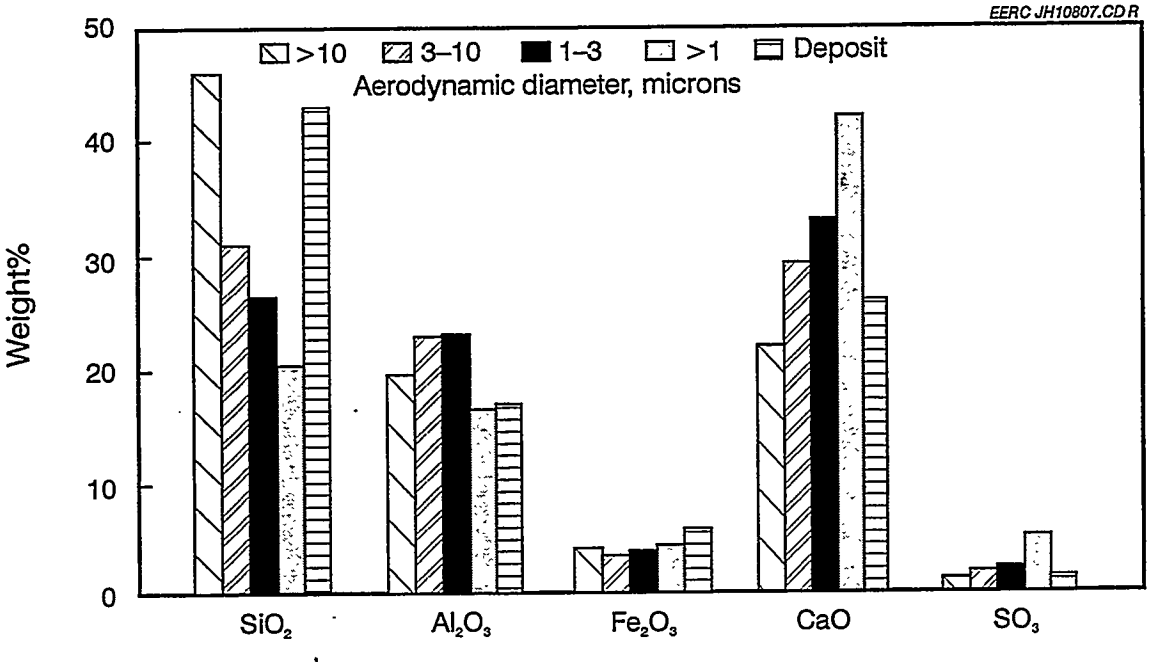

Fig. 1. Comparison of the compositions (SO_3-free) of the aerodynamically sized entrained ash particles and a conventional fouling deposit.

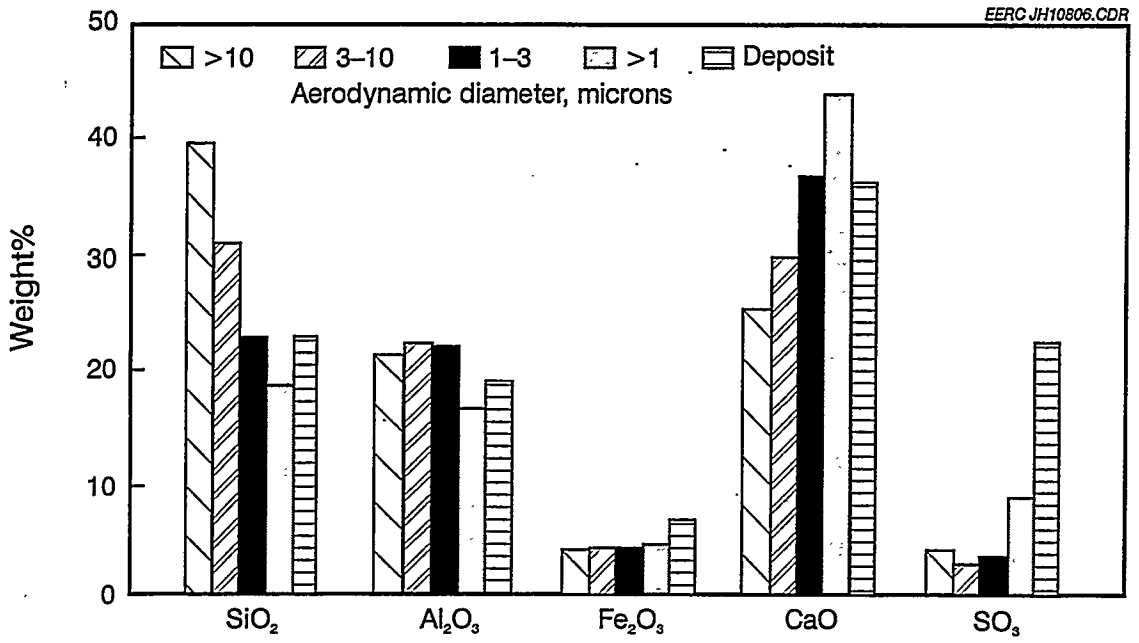

Fig. 2. Comparison of the compositions (SO_3-free) of the aerodynamically sized entrained ash particles and an upstream enamel deposit.

Factors Related to the Temperature of the Material

The temperature of the subsystem of interest affects both the composition of the ash deposit on its surface and the physical nature of the deposit. Figure 3 shows the concentrations of silicon, calcium, and sulfur in ash deposits collected from steam tubes in a boiler firing a high-calcium coal. It shows that the sulfur concentration in the deposits increases dramatically at temperatures below 2000°F. Laboratory experiments show that the mechanism of increase is chemical vapor deposition caused by the conversion of calcium in aluminosilicates to calcium sulfate below 1900°F. Figure 4 shows the concentrations of sodium, potassium, and phosphorus in the same deposits. They also increase significantly, but not as much as that of the sulfur. The sodium concentration increases primarily through physical vapor deposition, or condensation, of sodium sulfate. This indicates that materials cooled to below approximately 1900°F will be especially subjected to alkali sulfate corrosion. This situation may be especially prevalent for heat exchangers operating at gas temperatures above 1900°F but surface temperatures below that; however, depending on the local gas flow characteristics, the material can be rapidly covered with ash and, thus, protected from this type of corrosion. Hot-gas cleanup filters may also experience this type of corrosion if most of the larger ash is efficiently removed by upstream cyclones. Heat exchangers producing working fluids with temperatures above 1900°F would not be expected to experience this type of corrosion.

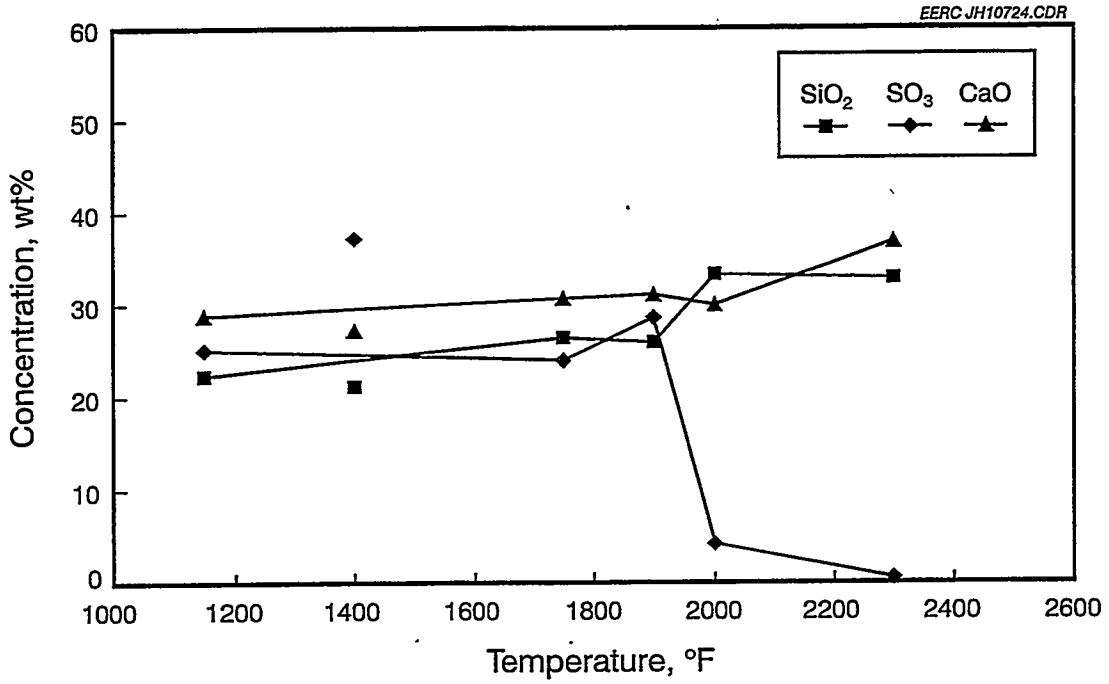

Fig. 3. Temperature-dependent concentrations of silicon, sulfur, and calcium (reported as oxides) in deposits collected from the convective pass of a pulverized coal-fired utility boiler burning a subbituminous coal from the western United States.

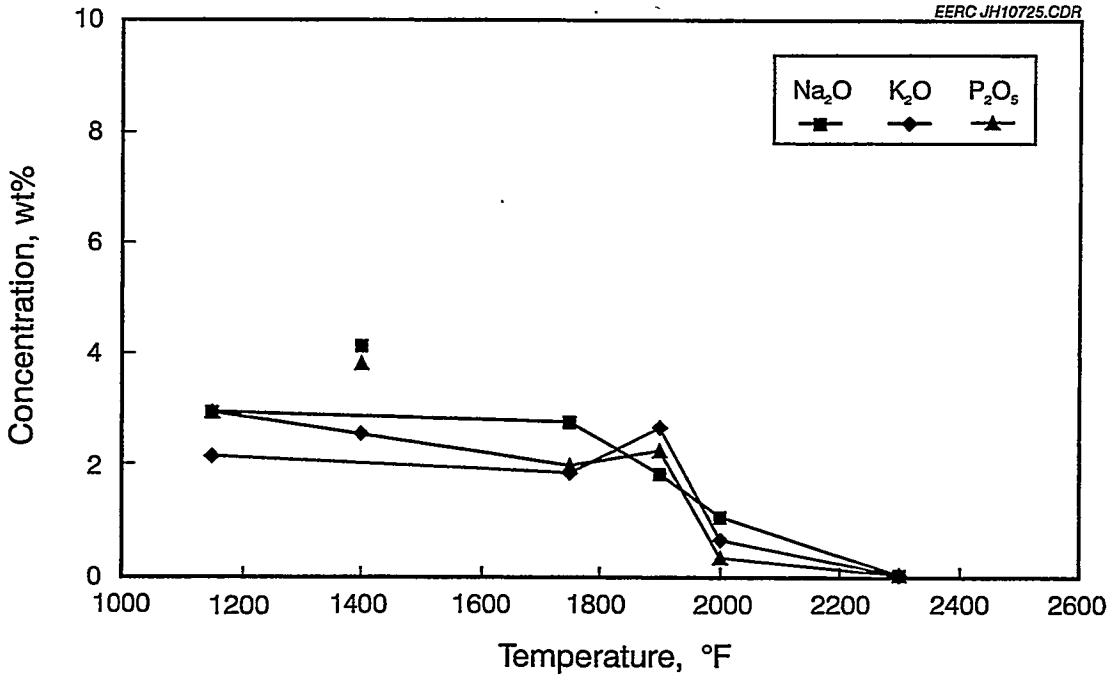

Fig. 4. Temperature-dependent concentrations of sodium, potassium and phosphorus (reported as oxides) in deposits collected from the convective pass of a pulverized coal-fired utility boiler burning a subbituminous coal from the western United States.

In addition to affecting the composition of the deposits, temperature will affect the physical nature of the deposits. Figure 5 shows a viscosity-versus-temperature plot for fused slag formed in a boiler burning Illinois No. 6 bituminous coal to which limestone has been added to reduce the viscosity of the slag. The measurements were made in air and in a reducing environment in the presence of 10% water vapor. It shows that, at temperatures above 2500°F, the slag has a viscosity below 250 poise and will flow well and can, therefore, be very erosive as well as corrosive. However, the flow of the slag is expected to result in a uniform recession rate of the surface, instead of pitts. Other measurements have shown that this type of slag can be liquid down to at least 2300°F[5]. Although much less erosive than the higher-temperature slags, these liquid slags are still able to dissolve the protective oxide scale on most ceramic materials, causing the corrosion rate to be linear rather than parabolic with time.

Figure 6 is a scanning electron micrograph of a cross section of Hexoloy SA silicon carbide exposed to a nonlimestone-doped Illinois No. 6 slag at 2300°F in a static slag corrosion test performed in air[5]. The bright spheres are composed of iron silicide that are often found near pits in the silicon carbide. In such cases, the protective silica layer is dissolved into the slag, and the pitting may weaken the material, although the recession rate is reduced as compared to higher-temperature slag corrosion. At still lower temperatures, the ash may sinter but does not dissolve the protective oxide layer. Figure 7 is a scanning electron micrograph of the interface between

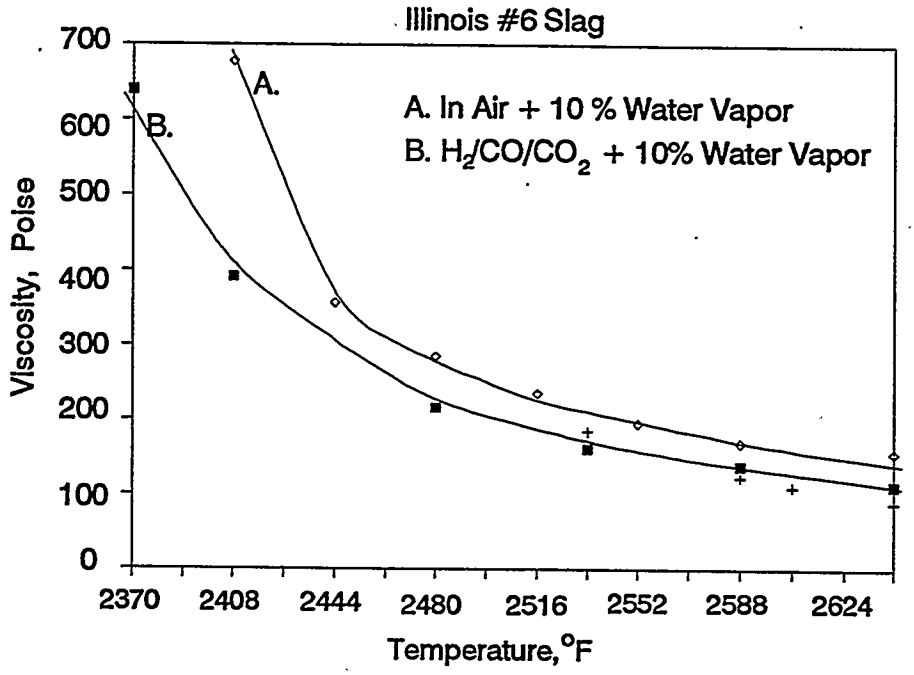

Fig. 5. Viscosity-versus-temperature plot for a slag produced in a boiler firing Illinois No. 6 bituminous coal to which limestone had been added to reduce slag viscosity.

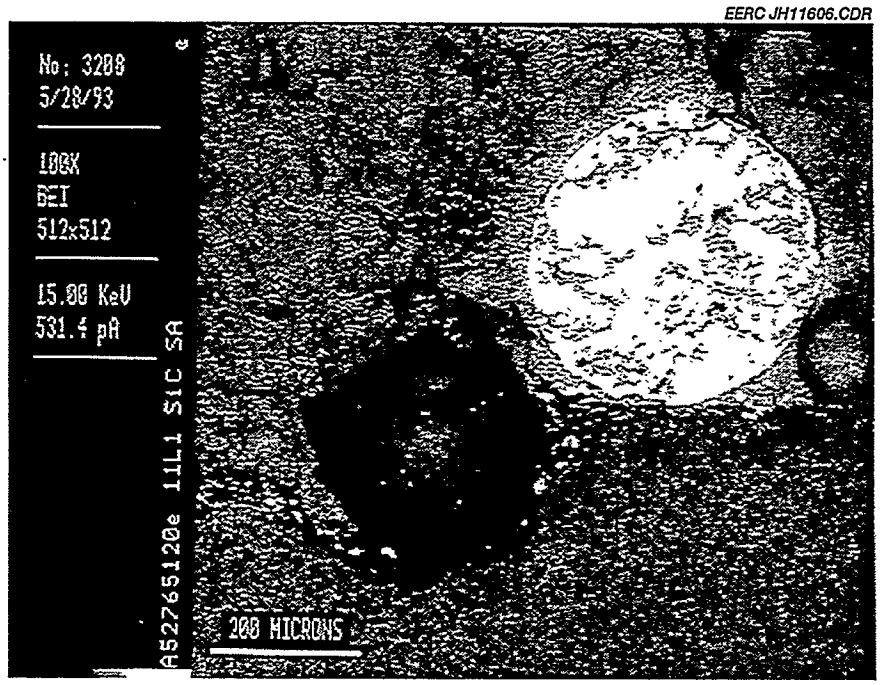

Fig. 6. Scanning electron micrograph of a cross section of Hexoloy SA silicon carbide (bottom) exposed to Illinois No. 6 slag at (top) 2300°F in a static slag corrosion test in air.

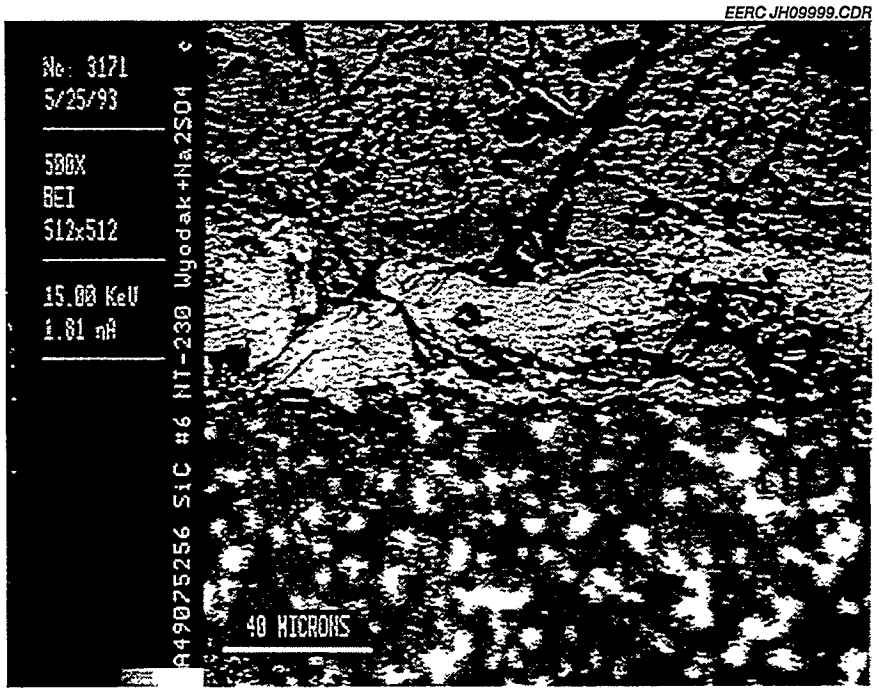

Fig. 7. Scanning electron micrograph of the interface between siliconized silicon carbide (bottom) and a high-calcium ash doped with excess sodium sulfate (top) reacted at 1790°F.

siliconized silicon carbide and a high-calcium ash doped with excess sodium sulfate reacted at 1790°F. These conditions simulate a situation in which a heat exchanger may be protected from the bulk of ash deposition by a slag screen but still exposed to fine ash and sodium sulfate condensation[6]. SEM analyses show that the scale is composed of calcium and magnesium silicate. Only very low levels of sodium could be measured in the scale, but similar experiments made without the condensed sodium sulfate (but with the vapor) show that the oxidation rate of the material is greatly increased by the presence of the sodium. Sodium silicate does not form extensively, because it is not stable as a silicate in the presence of aluminosilicate ash.

THE EFFECTS OF SPECIFIC ELEMENTS IN THE CORROSION OF SILICON-BASED CERAMICS

Approximately a dozen inorganic elements in the products of coal combustion affect the corrosion rates of silicon-based ceramics used to construct subsystems. The elements, including H, O, Na, Mg, Al, Si, P, S, Cl, K, Ca, and Fe, affect corrosion rates in three main ways: as primary corrodants that form reaction products with the material; as secondary corrodants that affect the activity of the primary corrodants; or by affecting the rate of mass transfer of the primary corrodants. Although many of the elements participate as more than one type of corrodant, they are listed here under what we believe is the most active role.

The primary corrodants of silicon-based ceramics in coal-fired combustion systems include O, Mg, Ca, and Fe. These elements form silicates or silicides that are stable in the presence of the other constituents of the ash in contact with the ceramic surface. Examples of their corrosion products are shown in Figures 6 and 7. When ash is not present, such as the interior or down stream of a particulate removal device like a filter, a vapor-phase sodium can also be a primary corrodant of silicate ceramics, forming a sodium silicate reaction layer through which oxygen can more rapidly diffuse than through a pure silica layer[7].

In contrast to the primary corrodants, the secondary corrodants have not been observed in EERC tests to form corrosion products with silica- or alumina-based ceramics in the presence of coal ash. They are known, however, to affect the activities of some of the primary corrodants. The elements mainly having this role are H, Al, S, and Cl. Hydrogen, along with the carbonaceous part of the fuel, is most important in gasification conditions because it affects the concentration of O, and in combustion conditions, it helps to form volatile hydroxides such as $Si(OH)_4$ or NaOH which will affect corrosion rates when no other ash is present. Similarly, S and Cl affect the vapor-phase concentrations of Na_2SO_4 and NaCl, which will affect corrosion rates when ash is not present.[8] In addition, Al affects the activity of Na, Mg, and Ca. Since these elements are more stable in an aluminosilicate condensed phase than in a silicate corrosion product, they are less corrosive to silicate ceramics when aluminum is present in the ash.

Finally, the major role of several other major elements is in their effects on the rate of transport of the primary corrodants. These elements include Na, Si, P, and K. They are most important in their effect on the viscosity of a melt, as well as on the rate of ion diffusion in a glass. They have not been observed to form corrosion products except in minor roles.

Because the concentrations of many of these elements affect the activities of the primary corrodants, the surest experimental design to determine all of the interdependencies is the full factorial matrix, where the concentration of each element in the system is varied dependently on the others. However, the number of tests in such a matrix would involve X^n tests, where X is the number of variations of each element, and n is the number of different elements. For three variations (low, medium, and high concentrations) of each of 12 elements, the number of tests is 531,441 for a single temperature and pressure condition. The numbers can be partially reduced with the use of a fractional factorial test matrix, but the most cost-effective way to perform corrosion tests is to base them on realistic system conditions.

The best method to obtain appropriate test conditions is to expose the material in an operating combustor system. This can be expensive as a 100-hour pilot-scale combustor test may cost $50,000. As the scale of the test is reduced, so are the costs, but the accuracy of the conditions may also be compromised. To improve the accuracy of laboratory-scale test conditions, the EERC has been funded under a project entitled "Support Services for Ceramic Fiber-Ceramic Matrix Composites," administered under the Advanced Research and Technology Development (AR&TD) Materials Program at Oak Ridge National Laboratory, to assemble 55-gallon drums of coal ash and slag from four utility power plants. Quantities of each of these ashes will be supplied to any materials researcher for their testing at no charge to the researcher.

The samples were gathered by utility plant workers from areas of the power systems where they best simulate the state of the ash in contact with two types of possible ceramic subsystems. For testing of materials used in hot-gas filter systems, ash was provided by the American Electric Power Company Tidd plant from the Westinghouse Advanced Particle Filter while firing a Pittsburgh No. 8 coal and using a dolomite sorbent. Suggested conditions for such testing are 1650°F (although many other researchers do not use temperatures above 1550°F) in 15% CO_2, 15% H_2O, 3% O_2, 0.5% SO_2, 0.05% HCl, and 10 ppm NaCl, with a balance of N_2. The concentrations of HCl, SO_2, and NaCl were chosen to approximate high-end partial pressures for pressurized fluidized-bed reactors[9,10]. The correct partial pressures of the other gases cannot be produced in an atmospheric test, so we use the approximate relative concentrations of those species. This ash can also be used to test heat-exchanger materials that will operate in a pressurized fluidized-bed combustor downstream of a particulate removal device at temperatures below the sulfation temperature of the ash (approximately 1900°F), although it may be necessary to condition the ash to more appropriate gas concentrations before the start of the exposure.

To simulate the type of ash that will strike a high-temperature heat exchanger upstream of ash removal devices, slags were gathered from the taps of three cyclone-fired boilers. Subbituminous coal slag was provided by the Northern States Power Company Riverside plant, which was burning a coal from the Powder River Basin in Wyoming. Illinois No. 6 bituminous coal slag was provided by the Central Illinois Public Service Coffeen plant. Our analyses showed abnormally high calcium concentrations in this slag due to limestone additions to the coal to reduce slag viscosity. Therefore, another drum of Illinois No. 6 slag was provided by the Illinois Power Company Baldwin plant. Suggested initial conditions for slag testing are 1090°C for sintered ash conditions, 1260°C for viscous molten ash, and 1430°C for runny molten ash. We have run all of our tests in air, although viscosity tests show that water vapor may significantly affect slag viscosity and perhaps should be included at a level of about 15%. We are still investigating this

effect. The slag layer thickness should be approximately 3–5 millimeters to ensure appropriate oxygen transport. The compositions of the ashes are shown in Table 2.

SUMMARY

For a given temperature, the rate of corrosion of ceramic materials in advanced coal-fired energy systems is affected by the composition of the gas and condensed species in contact with the material. These compositions are dependent on the fuel (and sorbent in a fluidized-bed system) which determines that species will be present, the temperature of the material which determines whether vaporized species will have condensed and whether the ash is molten, and the local gas flow conditions which determine the size range of ash depositing and, therefore, the composition of the ash. Approximately 12 elements affect the corrosion rates of silicon-based ceramics. Oxygen, Mg, Ca, Fe, and Na (when no ash is present) are primary corrodants in that they have been observed to form corrosion products with silicon carbides. Secondary corrodants—H, Al, S, and Cl—have not been observed to form primary corrosion products under coal combustion conditions but do affect the activity of the primary corrodants. The other major elements, including Na, Si, P, and K, affect the rate of transport of the primary corrodants by affecting slag viscosity and ion mobility.

To improve the accuracy of laboratory-scale test conditions, the EERC has assembled 55-gallon drums of coal ash and slag from four utility power plants, which will be provided free of charge to investigators. The samples were gathered by utility plant workers from areas of the power systems where they best simulate the state of the ash in contact with two types of possible ceramic subsystems. For testing of materials used in hot-gas filter systems, ash from such a system is available. Suggested conditions for such testing are 1650°F (although many other researchers do not use temperatures above 1550°F) in 15% CO_2, 15% H_2O, 3% O_2, 0.5% SO_2, 0.05% HCl, and 10 ppm NaCl, with a balance of N_2.

Table 2. Chemical Compositions of Standard Ashes

Oxide, wt%	Tidd	Riverside	Coffeen	Baldwin
SiO_2	24.1	47.0	52.5	53.4
Al_2O_3	7.7	18.6	16.3	18.6
Fe_2O_3	6.4	5.3	13.5	17.6
TiO_2	0.3	1.4	0.7	0.7
P_2O_5	0.2	0.6	0.2	0.0
CaO	28.8	19.7	13.1	7.1
MgO	16.2	5.7	1.2	0.9
Na_2O	0.2	0.9	0.8	0.0
K_2O	0.8	0.3	1.6	1.7
SO_3	15.2	0.3	0.1	0.0

To simulate the type of ash that will strike a high-temperature heat exchanger upstream of ash removal devices, slags are available from three cyclone-fired boilers. Suggested initial conditions for slag testing are for sintered ash conditions, 2300°F for viscous molten ash, and 2600°F for runny molten ash. We have run all of our tests in air, although viscosity tests show that water vapor may significantly affect slag viscosity and perhaps should be included at a level of about 15%. The slag layer thickness should be approximately 3–5 millimeters to assure appropriate oxygen transport.

REFERENCES

1. Ferber, M.K.; Tennery, V.J. "Behavior of Tubular Ceramic Heat Exchanger Materials in Acidic Coal Ash from Coal–Oil Mixture Combustion," *Ceram. Bull.* **1983**, *62* (2), 236–243.

2. Ferber, M.K.; Tennery, V.J. "Behavior of Tubular Ceramic Heat Exchanger Materials in Basic Coal Ash from Coal–Oil Mixture Combustion," *Ceram. Bull.* **1984**, *63* (7), 898–904.

3. Combustion Engineering Inc. *Combustion*, 3rd ed.; Rand McNally: Chicago, 1981; pp 35–57.

4. Hurley, J.P.; Schobert, H.H. "Ash Formation During Pulverized Subbituminous Coal Combustion, 1. Characterization of Coals and Inorganic Transformations During Early Stages of Burnout," *Energy & Fuels* **1992**, *6* (1), 47–58.

5. Hurley, J.P.; Schobert, H.H. "Ash Formation During Pulverized Subbituminous Coal Combustion, 2. Inorganic Transformations During Middle and Late Stages of Burnout," *Energy & Fuels* **1993**, *7*, 542–553.

6. Walsh, P.M.; Sayre, A.N.; Loehden, D.O.; Monroe, L.S.; Beér, J.M.; Sarofim, A.F. *Prog. Energy Combust. Sci.* **1990**, *16*, 327–346.

7. Benson, S.A.; Jones, M.L.; Harb, J.H. "Ash Formation and Deposition," In *Fundamentals of Coal Combustion for Clean and Efficient Use*; Smoot D., Ed.; Elsevier: Amsterdam, 1993; 299.

8. Baxter, L.L.; DeSollar, R.W. *Fuel* **1993**, *72*, 1411.

9. Wibberley, L.J.; Wall, T.F. *Fuel* **1982**, *61*, 93–99.

10. Hurley, J.P.; Benson, S.A.; Erickson, T.A.; Allan, S.E.; Bieber, J. *Project Calcium Final Report*, DOE/MC/10637-3292, 1995.

11. Strobel, T.M.; Hurley, J.P.; Senior, C.L.; Holowczak, J.E. "Coal Slag Corrosion of Silicon Carbide-Based Ceramics in a Combustion Environment," *In* Proceedings of the Symposium on Silicon Carbide-Based Structural Ceramics; American Ceramic Society PAC RIM Meeting, Honolulu, HI, Nov. 7–10, 1993, pp 327–334.

12. Strobel, T.M.; Hurley, J.P.; Breder, K.; Holowczak, J.E. "Coal Slag Corrosion and Strength Degradation of Silicon Carbide–Alumina Composites," *Ceramics Engineering & Science Proceedings* **1994**, *15*(4), 579–586.

13. Senior, C.L.; Moniz, G.A.; Hurley, J.P.; Strobel, T.M. "Corrosion of Silicon Carbides by Ash and Vapor in a Coal Combustion Environment," *In* Proceedings of the Symposium on Silicon Carbide-Based Structural Ceramics; American Ceramic Society PAC RIM Meeting, Honolulu, HI, Nov. 7–10, 1993, pp 335–342.

14. Zheng, Z., Tressler, R.E.; Spear, K.E. "A Comparison of the Oxidation of Sodium Implanted CVD Si_3N_4 With the Oxidation of Sodium-Implanted SiC Crystals" *Corrosion Science* **1992**, *33* (4), 569–580.

15. Mann, M.D.; Swanson, M.L.; Yagla, S.L. "Characterization of Alkali and Sulfur Sorbents for Pressurized Fluidized-Bed Combustion" *In* Proceedings of the 13th International Fluid Bed Conference, ASME, 1995.

CORROSION PERFORMANCE OF MATERIALS FOR ADVANCED COMBUSTION SYSTEMS*

K. Natesan
Argonne National Laboratory
Argonne, IL 60439

and

M. Freeman and M. Mathur
Pittsburgh Energy Technology Center
Pittsburgh, PA 15236

ABSTRACT

Conceptual designs of advanced combustion systems that utilize coal as a feedstock require high-temperature furnaces and heat transfer surfaces capable of operating at much higher temperatures than those in current coal-fired power plants. The combination of elevated temperatures and hostile combustion environments requires development and application of advanced ceramic materials for heat exchangers in these designs. This paper characterizes the chemistry of coal-fired combustion environments over the wide temperature range of interest in these systems and discusses some of the experimental results for several materials obtained from laboratory tests and from exposures in a pilot-scale facility.

INTRODUCTION

Coal is a complex and relatively dirty fuel that contains varying amounts of sulfur and a substantial fraction of noncombustible mineral constituents, commonly called ash. Recently, the U.S. Department of Energy has embarked on programs to develop coal-fired boilers with advanced steam cycles, fluidized-bed combustion cogeneration systems, high-performance power system (HIPPS), and a low-emission boiler system (LEBS). Conceptual designs of advanced combustion systems that utilize coal as a feedstock require high-temperature furnaces and heat transfer surfaces capable of operating at higher temperatures than those used in current coal-fired power plants. The combination of elevated temperatures and hostile combustion environments necessitates the use of ceramic materials at least in the first few passes of the heat exchangers in these designs.

The HIPPS would employ a combined cycle that uses a gas turbine driven by a working fluid (air) that is separately heated in a high-temperature advanced furnace, in addition to conventional steam turbines.[1] The ultimate goal is to produce electricity from coal with an overall thermal efficiency of 47% or higher (compared with ≈35% for current systems) and to reduce CO_2 emissions by 25 to 30%. The targeted requirements for an HIPPS system are:

---

*Work supported by the U.S. Department of Energy, Office of Fossil Energy, Advanced Research and Technology Development Materials Program, Work Breakdown Structure Element ANL–4, under Contract W–31–109–Eng–38.

- A minimum conversion efficiency of 47%.
- NO_X < 0.06 lb (as NO_2) per million Btu of fuel input.
- SO_X < 0.06 lb (as SO_2) per million Btu of fuel input.
- Particulates < 0.003 lb per million Btu of fuel input.
- All solid waste streams must be benign.
- Initially, fuels will be coal and natural gas, with coal providing at least 65% of heat input and ultimately increasing to 95%.
- The commercial plant will have a 65% annual capacity factor and generate electricity at a 10% lower (than present) cost.

The pulverized-coal high-temperature advanced furnace (HITAF) in the HIPPS concept will heat air to an intermediate temperature of ≈1000°C and burn supplemental clean fuel to boost the temperature of air to the turbine inlet temperature of ≥1300°C. Use of supplemental fuel can be reduced as the HITAF technology evolves to permit air to be heated to higher temperatures in the furnace. HITAF represents a major departure from conventional pulverized-coal-fired boilers in which only steam is raised to a maximum of 530-620°C. The purpose of the HITAF is to heat the clean working fluid – air – to the required turbine inlet temperatures. At the elevated temperatures of the HITAF, transfer of heat from the combustion gases to the working fluid will be dominated by radiative heat transfer, and the design of the heat transfer surface will be critical for success of the system. Several concepts are under development for the design of the heat transfer surfaces in the HITAF system. The concept proposed by the Foster Wheeler Development Corporation uses a pyrolysis process to convert the coal into low-Btu fuel gas and char.[2] The cleaned fuel gas is burned in areas of the HITAF where ash deposition could be a problem. The concept proposed by the United Technologies Research Center uses a combustor with a controlled fuel distribution/long axial flame in which the heat release is stretched out, allowing for progressive heat removal.[3] The compressed air is heated to 700°C in a convective air heater and then to 1000°C in a radiative air heater. A protective refractory layer on the fire side of the radiant air heater prevents corrosion of air passages by ash and slag, which inevitably will be deposited on the heat transfer surface. This concept also involves heating of the air with supplemental natural gas firing to achieve a 1300°C turbine inlet temperature.

Irrespective of which of these (or any other) concepts becomes viable for a commercial-scale HIPPS, it is evident that the heat transfer surfaces will be exposed to much higher temperatures than are prevalent in conventional coal-fired steam-turbine systems. For temperatures in the range of 1000-1300°C, conventional metallic materials do not possess adequate strength properties and/or corrosion resistance for long-term service. In addition, an important difference between the conventional boiler system and the HIPPS is seen in the chemical and physical characteristics of the ash layers that can deposit on the heat transfer surfaces. The deposits are likely to be dominated by alkali sulfates and coal slags in HIPPS rather than by pyrosulfates or alkali-iron-trisulfates (which are prevalent in conventional pulverized coal-fired boilers) and by the increased mobility of corrosion-accelerating agents in the deposit layers due to the much higher temperature of the heat transfer surfaces in HIPPS. A major challenge is to develop methods to combat severe deposition, erosion,

and corrosion (DEC) of heat transfer surfaces exposed to higher-than-normal temperatures. These methods could include fuel selection, cleaning of aggressive contaminants from coal, fine grinding of coal, use of additives, and selection of advanced corrosion-resistant ceramic materials, coatings, and advanced alloys for vulnerable heat transfer sections.

The objectives of the present program are to evaluate (a) the chemistry of gaseous and condensed products that arise in combustion of coal and (b) candidate materials for application in the combustion environments. Chemistry calculations determine the types and amounts of combustion products over the wide temperature range of 700-1700°C and at 1 atm pressure. The experimental program on heat exchanger materials will develop mechanistic information on the roles of material composition, ash constituents, combustion deposits, chlorine, alkali sulfates, and sulfur sorbents in the corrosion process. The program emphasizes corrosion evaluation of materials in air, salt, and coal/ash environments at temperatures between 1000 and 1400°C, as well as measurement of residual fracture properties of the materials after corrosion. Coal/ash chemistries synthesized on the basis of thermodynamic/kinetic calculations, together with slags from actual combustors, are used in the program. The paper will present selected results on several materials exposed in both laboratory tests and in the Combustion and Environmental Research Facility (CERF) at DOE's Pittsburgh Energy Technology Center.

Thermodynamic calculations were used to evaluate the chemistries of gaseous and condensed phases that occur during combustion of an Illinois bituminous coal. The computer program used for the calculations is based on calculating the equilibrium concentrations of various species by minimizing the free energy of the system. Details of the calculations are presented in Ref.4. Calculated results for the chemistry of condensed phases and the gaseous phase at the combustion air:coal stoichiometric ratio of 1.3 showed that coal combustion results in a liquid phase that is essentially a silica-saturated silicate and/or sulfate condensate, with the components made up largely of SiO_2, Al_2O_3, CaO, Fe_2O_3, Na_2SO_4, and NaCl (see Fig. 1). At temperatures below 1180°C, the partial pressures of NaCl(g), HCl(g), NaOH(g), and Na(g) change abruptly; a complex sodium aluminosilicate, $Na_2O{:}Al_2O_3{\cdot}6SiO_2(s)$, tends to form; and the liquid silicate-sulfate condensate disappears. Formation of the complex silicate requires intimate contact among several gaseous and condensed phases, the probability of which is expected to be low in real systems. Under nonequilibrium conditions, where such reactions are constrained, stability of the liquid sulfate–silicate condensate extends to temperatures as low as 890°C.

Above 1330°C, the solution consists mostly of $Al_2O_3{\cdot}SiO_2$, $CaO{\cdot}SiO_2$, $Na_2O{\cdot}SiO_2$, and $FeO{\cdot}SiO_2$, as well as traces of Na_2SO_4. As the temperature decreases, the concentration of $FeO{\cdot}SiO_2$ decreases and that of Na_2SO_4 increases. At 1130°C, Na_2SO_4 concentration may be relatively high (about 12 mol% for high-sulfur coal) and may increase very rapidly with a decrease in temperature. Under nonequilibrium conditions, the solution phase is rich in Na_2SO_4. For high-sulfur coal at temperatures below 930°C, the solution phase consists of more than 90 mol% sulfate. A solution phase consisting of sodium, magnesium, and calcium sulfates is stable below 880°C. The transition from silicate sulfate to sulfates occurs within the temperature range of 1130-980°C.

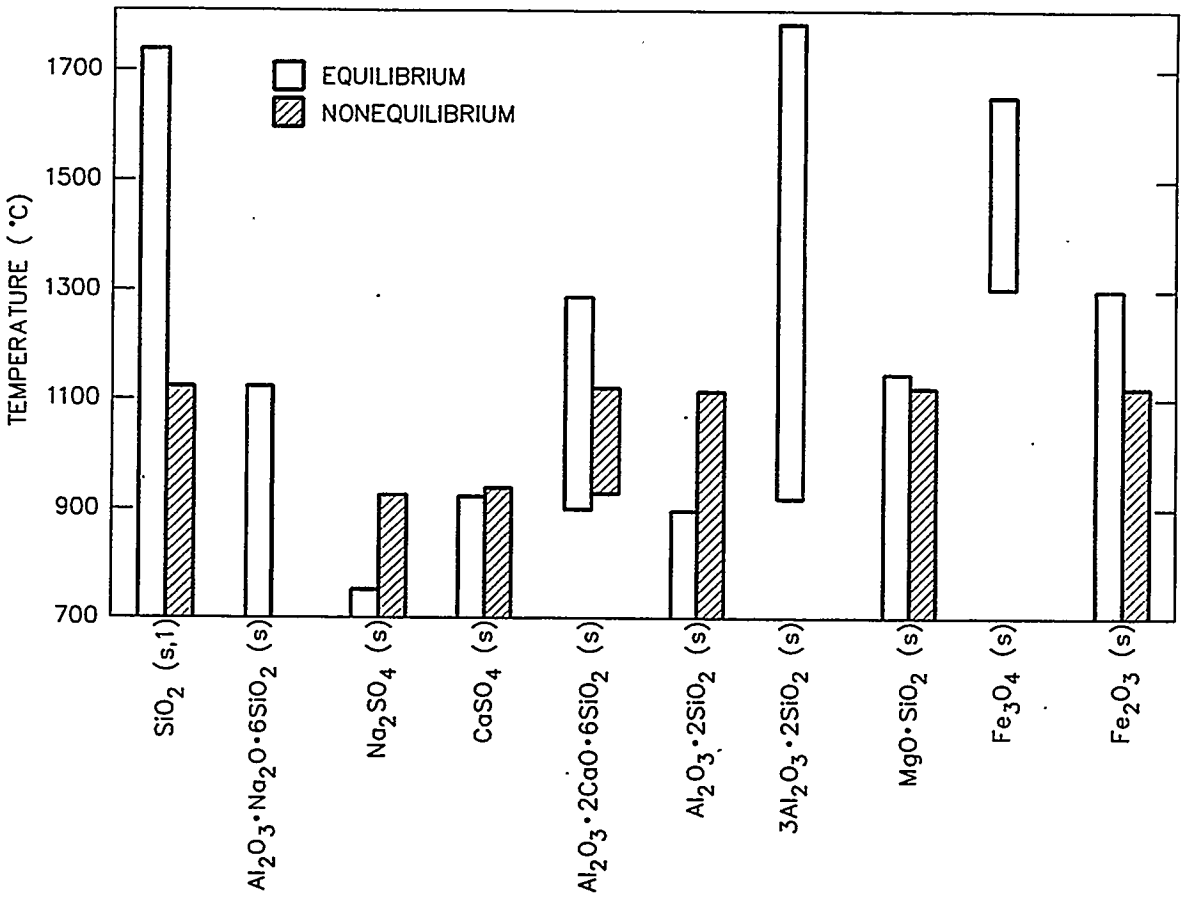

Fig. 1. Approximate temperature ranges for stability of condensed phases during combustion of high-sulfur coal with 30% excess oxygen.

Based on the results of these calculations, the general behavior of the solution phase under oxidizing conditions can be described as follows. A liquid solution phase, consisting mostly of silicates of aluminum, calcium, sodium, magnesium, and iron, is present at 1730°C. The mole fraction of Na_2SO_4 phase in the liquid is <0.01 above 1280°C. The concentration of Na_2SO_4 rises rapidly as the temperature decreases and becomes a major component of the solution at 980°C. The mole fraction of Na_2SO_4 may increase to 0.9 or more at 980°C. These compositional changes can have implications for the corrosive behavior of the liquid condensates. In the temperature range of interest in HIPPS, the predominant deposits are either mullite or Ca-rich aluminosilicates. The silicate liquid may be even more corrosive and have worse fouling tendencies than sulfates because of (a) high temperature conditions, (b) adhesive behavior of the silicates, and (c) solubility of ceramic materials, which are probably higher in silicate than in sulfate melts.

EXPERIMENTAL PROCEDURE

Laboratory Experiments. The materials selected for the laboratory experimental program include advanced metallic alloys, monolithic ceramic materials, and ceramic-matrix ceramic composites; they are listed

in Table 1, together with their manufacturers. Coupon specimens measuring 2 cm x 2 cm x 2-3 mm were prepared from several of the above–listed materials for salt- and slag-exposure experiments. Dimensions and initial weights of the specimens were measured prior to exposure. Salt tests were conducted at 1000 and 1200°C in the presence of Na_2SO_4 or a mixture of Na_2SO_4 and NaCl for 168 h. Tests in the presence of three different slags were conducted at 1200°C for a test time of 200 h. Table 2 lists the compositions of slags and the coals that were combusted to obtain these slags. Analysis shows that the slag obtained from Illinois #6 coal was richer in Fe_2O_3 and leaner in CaO and MgO, while the reverse is seen for slag from the Rochelle coal. Slags #43 and XX typify the slags derived from coals in the eastern U.S. while the slag #47 is typical of that derived from western coals.

Combustor Experiments. High-temperature materials were tested by exposing samples of several ceramic materials in the CERF at the Pittsburgh Energy Technology Center. The CERF is a state-of-the-art, 0.5 millionBtu/h pilot-scale combustion facility designed to achieve similarity with full-scale utility and industrial boilers. The CERF is designed to closely duplicate typical full-scale specifications for:

- Solid fuel fineness or liquid fuel atomization quality.
- Burner relative mass flow (fuel and air) and velocities.
- Furnace temperature distributions.
- Radiant furnace residence time.
- Convective section gas velocity.

Table 1. Materials selected for corrosion tests

Material	Manufacturer
Alumina	Coors Ceramics
Hexoloy SA	Carborundum
SiC (I) particulate in alumina	Lanxide/Du Pont
Siliconized SiC (NT230)	Norton/TRW
Silicon Nitride (NT154)	Norton/TRW
SiC fibers in SiC matrix	Du Pont
SiC fibers in Si_3N_4 matrix	ORNL

Table 2. Compositions of slags for laboratory study

Compound	Slag 43/ Illinois #6	Slag 47/ Rochelle	Slag XX/ Illinois #6
SiO_2	52.9	47.1	53.3
Al_2O_3	16.6	18.8	18.6
Fe_2O_3	12.9	5.2	17.6
CaO	13.0	19.6	7.2
MgO	1.3	5.8	1.0
Na_2O	0.8	0.9	0
K_2O	1.6	0.3	1.7
SO_3	0.1	0.3	0

Materials exposures in CERF are being conducted in a piggyback mode, whereby normal CERF testing would proceed in terms of evaluating combustion of various coals and coal blends. Figure 2 is a cross section of the radiant and convective portions of CERF, showing locations where samples are being exposed for corrosion evaluation. With this approach, comparative assessments of many materials at different locations could be made economically before pursuing dedicated-materials CERF tests that would require continuous operation of the facility for 1000 h or more. To minimize thermal stresses during exposure, samples were placed in the CERF prior to the start of each test and removed after the CERF was cooled to room temperature. Coupon samples of several of the ceramic materials (see list in Table 1) were mounted on a water-cooled, high-temperature materials testing probe that uses welded clips and pins to hold the samples, as shown in Fig. 3.

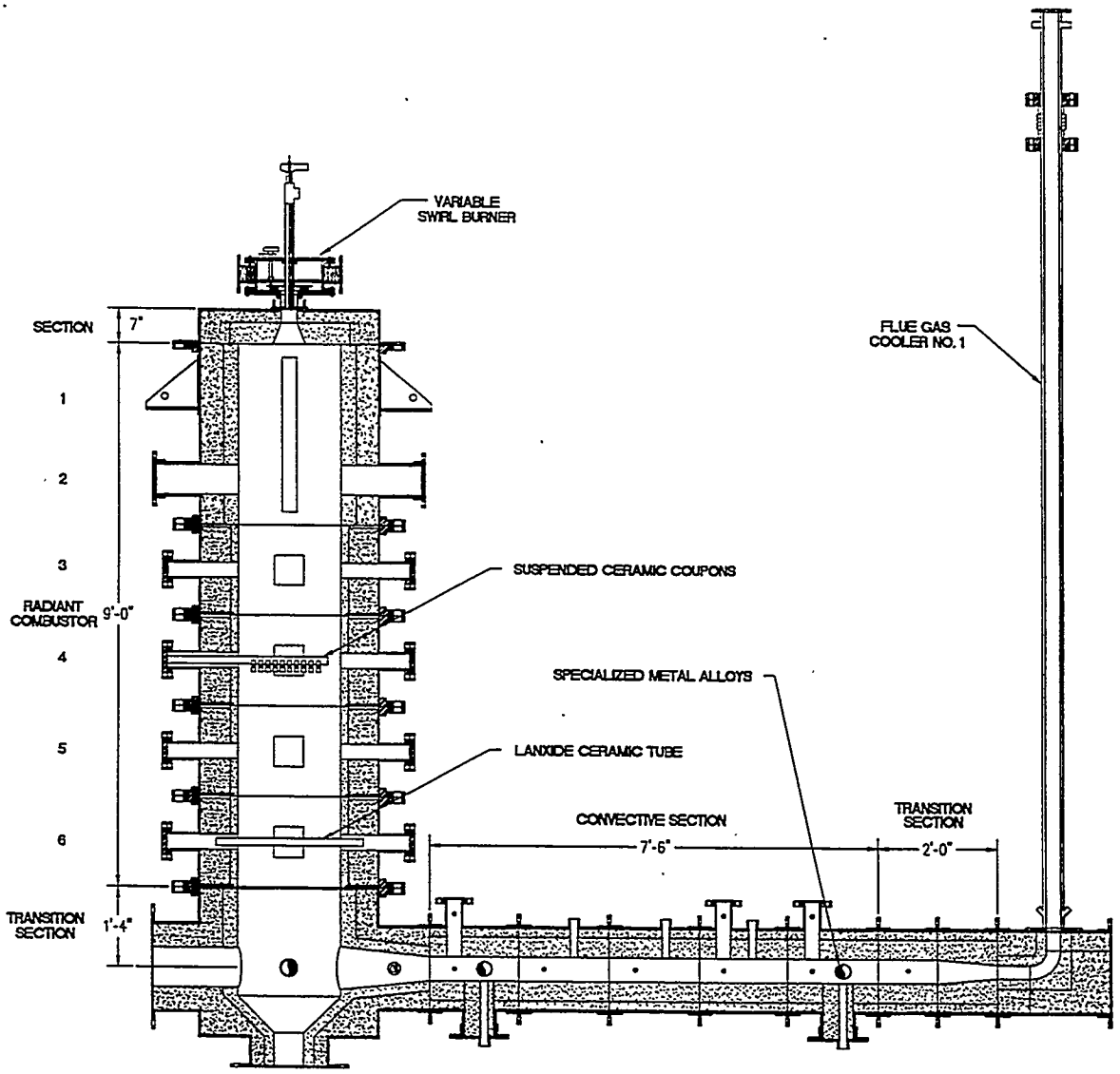

Fig. 2. CERF cross section of radiant and convective section and high-temperature materials test locations.

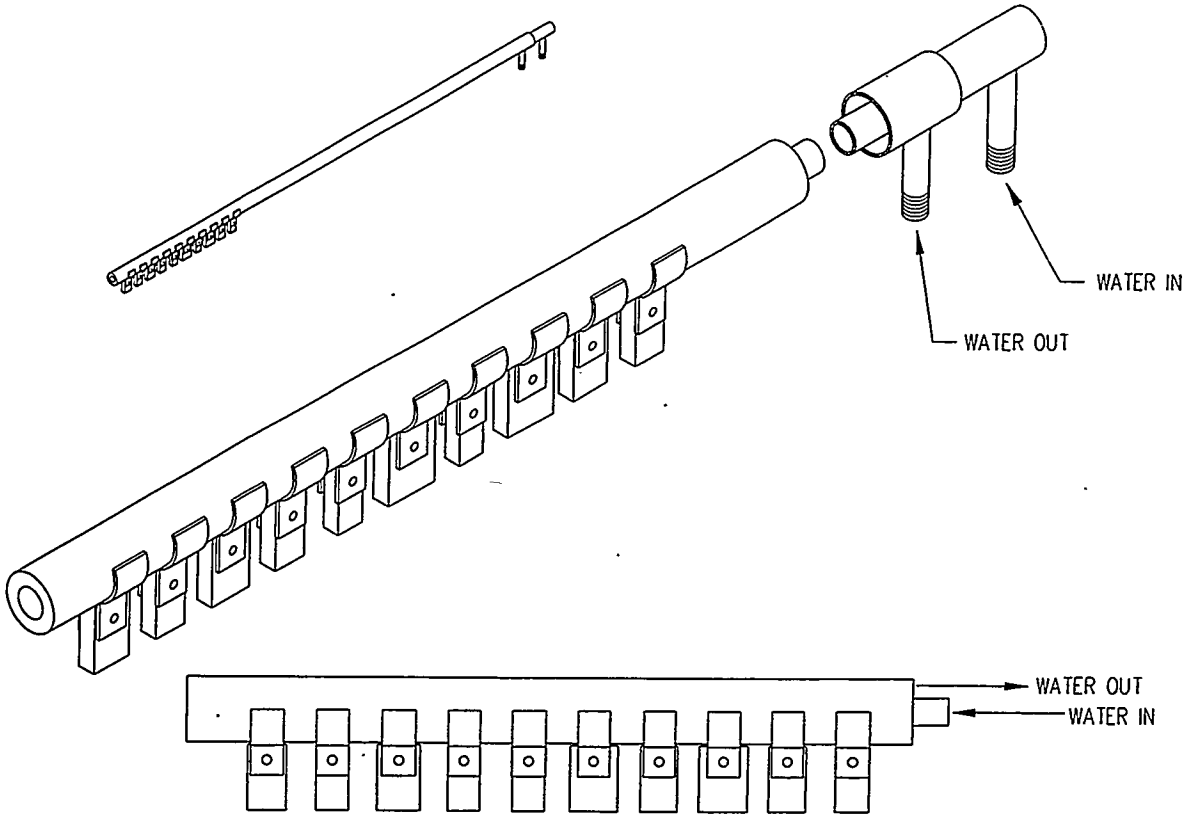

Fig. 3. Materials test probe for exposure of small coupons in CERF.

Table 3. Compositions (in wt.%) of coal ash

Compound	Ash 43/ Illinois #6	Ash 47/ Rochelle	Ash XX/ Illinois #6	Ash 1/ Pittsburgh	Ash 2/ Alaskan
SiO_2	56.5	32.1	51.6	41.5	43.1
Al_2O_3	20.8	18.0	19.2	21.5	17.0
Fe_2O_3	9.6	4.9	17.4	17.9	8.7
CaO	3.0	23.1	3.2	8.5	20.6
MgO	1.1	9.9	1.0	0.8	2.6
Na_2O	1.7	1.5	0.9	0.6	0.6
K_2O	2.5	0.3	2.4	1.3	1.2
SO_3	1.8	8.0	2.3	4.0	5.6
Ash Fluidity Temperature (°C)	1405	NA	1400	1388	1288

Ceramic specimens were exposed during two 100-h runs in which Pittsburgh coal and a blend of Alaskan/Russian coal were burned. Table 3 shows compositions of coals used in CERF runs, along with coals that generated slags for the laboratory test program.

EXPERIMENTAL RESULTS

Hexoloy SA: This material is a sintered form of alpha silicon carbide with >98% of theoretical density. It has a very fine grain structure (8 μm) for excellent wear resistance, contains no free silicon, and has been reported to be chemically resistant in both oxidizing and reducing environments. In air tests, the Hexoloy SA oxidized to form a silica layer, as evidenced by the oxygen content of the surface regions of the air-exposed specimens. At 1400°C, all of the carbon in the surface region was reacted and oxygen enrichment was substantial. The material exhibited passive oxidation of SiC to SiO_2.

In the salt tests at 1200°C, the specimen melted, indicating formation of a low-melting compound (i.e., melting point <1200°C) by reaction of salt and silicon. Based on the Na_2O-SiO_2 phase diagram, additions of even a small amount of Na_2O to silica can lead to $Na_2O{\cdot}xSiO_2$ with melting temperature decreasing as Na_2O content increases. Because pure Na_2SO_4 will establish a fairly high Na_2O activity, especially at 1200°C, formation of the low-melting (Si,Na,O) compound is most likely. In a 50:50 mixture of salt and slag, oxidation of silicon carbide to silicon oxide was virtually complete in 168 h of exposure. At longer exposure times, the reaction between silicon oxide and sodium oxide will occur, resulting in a low-melting (Si,Na) compound observed in pure salt tests.

In laboratory slag tests, the materials behaved differently than in salt tests. The specimen showed significant surface cracking but the slag itself didn't seem to penetrate the sample, as evidenced by energy-dispersive X-ray (EDX) analysis of specimen cross sections. Because Na_2O activity in the slag is relatively low, the deposit did not melt, but significant bubbling of the slag was noted, probably due to formation of SiO vapor in a reducing condition established locally by entrapped carbon in slag. All three slags exhibited similar appearance after the test and also all three specimens exposed to different slags appeared similar, indicating that coal slag chemistry has little influence in these short exposures. Figure 4 shows SEM photomicrographs of specimen cross sections after exposure in the three slags. In the first CERF exposure conducted with Pittsburgh coal, the specimen exhibited a thin layer of deposit after ≈100 h of testing. X-ray diffraction analysis of the deposit indicated predominantly mullite ($3Al_2O_3{\cdot}2SiO_2$) with some ordered albite [(Na,Ca)Al(Si,Al)$_3O_8$] along with traces of hematite. No significant degradation of the sample was observed in scanning electron microscopy (SEM) and EDX analysis. The sample from the second run, in which a blend of Alaskan and Russian coals was combusted, was lost even though the pin and the clip holding the sample were intact. This may qualitatively indicate that the material may be susceptible to cracking at elevated temperatures by particle impingement.

SiC (p) in Al_2O_3: This material was fabricated by Du Pont-Lanxide by a direct metal oxidation process and has an Al_2O_3 matrix with SiC particulates dispersed throughout the matrix. The surface regions of the samples exposed to either salt or slag were devoid of SiC particulates, based on EDX analysis. Reactions between alumina, silica, and sodium oxide in salt experiments can lead to corrosion products with several possible compositions, but microscopic observations of the reacted layers indicate that no liquid phase formed and that the Na_2O activity is low enough to form higher-melting compounds enriched in alumina and silica. Coupons of this material tested in laboratory slag tests also showed SiC conversion to silica, but corrosion or internal penetration of the material was negligible. Moreover, CERF tests showed that the

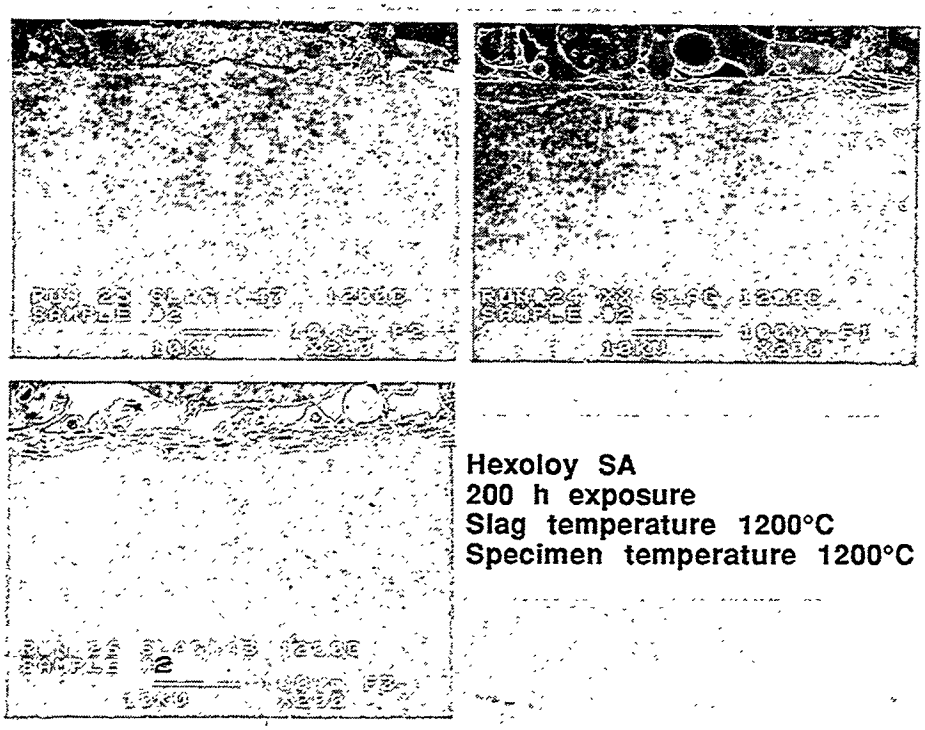

Fig. 4. SEM photomicrographs and EDX analysis of cross sections of Hexoloy SA specimens after exposure in CERF during combustion of Pittsburgh coal.

compositions of the deposit layers were somewhat different between the two runs. In the run with Pittsburgh coal, the deposit contained significant iron oxide, while the run with Alaskan blend exhibited a high concentration of CaO. The deposit composition seems to have a significant effect on stickiness and subsequent accumulation on the specimen surface. The deposit in CERF run 2 was at least twice as thick as in run 1 for the nominal operating conditions and same time of exposure. Figures 5 and 6 show the SEM photomicrographs of specimen cross sections and deposits obtained in the two runs. Also shown is the EDX elemental distribution for several elements of interest from the corrosion standpoint.

Siliconized SiC: This material (identified as NT 230) made by Norton/TRW was tested in salt and slag environments in the laboratory and in CERF. In the salt experiments, the surface regions of the specimens lost carbon, but from the standpoint of corrosion the material was virtually unaffected. In the slag experiments at 1200°C, the specimens exhibited surface cracks (similar to Hexoloy SA) but corrosion degradation was minimal or nonexistent. In CERF tests, the material developed a silica-rich region but from the corrosion standpoint, the material was virtually unaffected (similar to Hexoloy SA).

SiC Fiber/SiC Matrix: This material is made by Du Pont with a chemical vapor infiltration process. It is recommended for service requiring high strength, high-temperature properties, and light weight. The material exhibits creep deformation at temperatures >1200°C, contrary to behavior of Hexoloy SA and NT 230, in which creep was virtually absent.

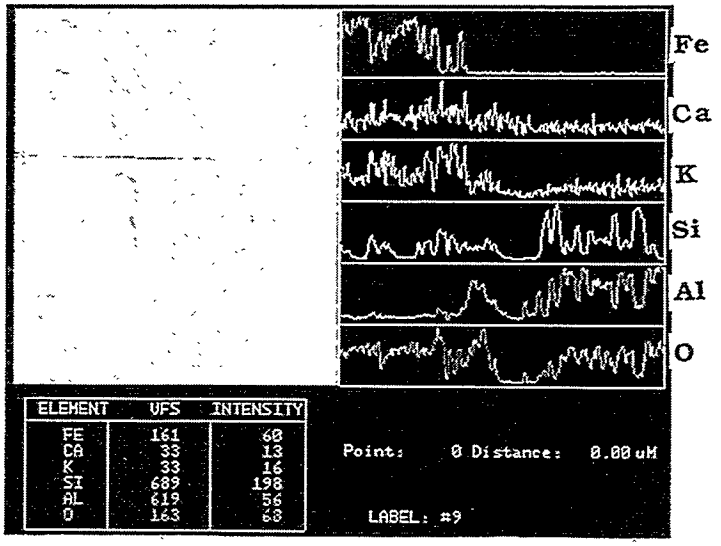

Fig. 5. SEM photomicrographs and EDX analysis of cross sections of SiC(p)/Al_2O_3 specimens after exposure in CERF during combustion of Pittsburgh coal.

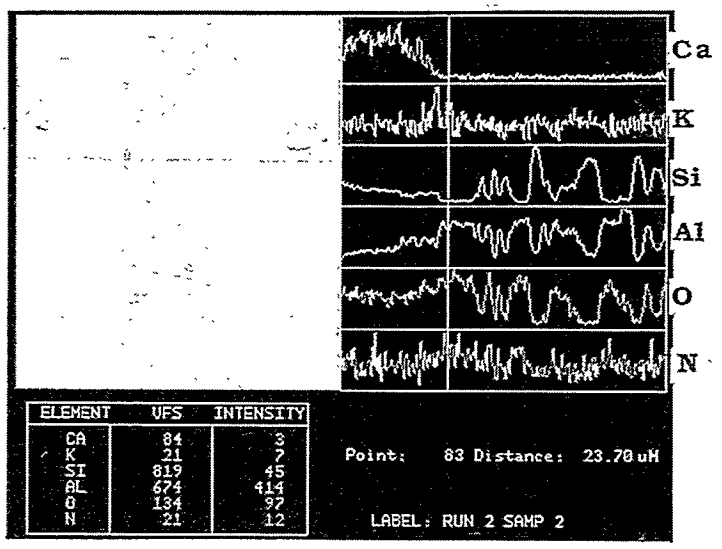

Fig. 6. SEM photographs and EDX analysis of cross sections of SiC(p)/Al_2O_3 specimens after exposure in CERF during combustion of Alaskan/Russian blend coal.

In salt exposures conducted in the laboratory, the material behaved similarly to monolithic SiC from the reaction standpoint. Surface regions were devoid of SiC, while the interior was unaffected by the salt during 168 h of exposure. In slag experiments at 1200°C, the material developed only a solid reaction product and the reaction was confined to the surface regions of the specimens. The behavior of the material in CERF exposures was similar to those of monolithic SiC such as Hexoloy SA and NT 230.

DISCUSSION

Corrosion of ceramic heat exchanger surfaces in coal-fired systems can occur via three different mechanisms dictated by the material composition and exposure environment (which includes temperature, gas chemistry, and deposit chemistry). The gas and deposit chemistries, in turn, will be dictated by the coal and ash chemistry, combustion conditions, and gas and particulate flow conditions determined by furnace design. The first mode of degradation of ceramic materials such as monolithic and composite SiC, Si_3N_4, and SiC-dispersed Al_2O_3 is by oxidation of SiC and Si_3N_4 in air. Oxidation can occur via either the passive mode in which a solid SiO_2 phase forms and can offer protection against further oxidation, or via active oxidation in which the SiO phase forms and can volatilize, resulting in accelerated oxidation of the material. The air oxidation experiments conducted with these materials at temperatures in the range 1000-1400°C in dry air environment showed that the materials undergo passive oxidation. However, the effect of water vapor on oxidation needs further evaluation.

The second mode of degradation of these materials involves reactions between the ceramic materials and alkali sulfates such as Na_2SO_4 and K_2SO_4 and alkali chlorides such as NaCl and KCl. In the combustion gas environment, the concentrations of oxygen and of sulfur as SO_2 and SO_3 determine the sodium oxide activity via the reaction $Na_2SO_4 = Na_2O + SO_3$. Subsequently, the silica phase that forms on the ceramic materials can react with Na_2O to form compounds such as $Na_2O{\cdot}XSiO_2$, where X can be 0.5, 1, 2, or 4. These sodium silicates have melting temperatures in the range of 875-1110°C. This mode of degradation of ceramic materials requires that Na_2O activity be sufficiently high and is usually possible in gas turbine systems where slag constituents are virtually absent. In such instances, the liquid phase can dissolve the protective SiO_2 scale and also result in penetration of the liquid reaction products into the substrate ceramic material, thereby mechanically weakening the material. In coal-fired combustion systems, the presence of slag constituents determine the thermodynamic activity of various deposit constituents, and alkali-sulfate-induced corrosion is generally not dominant.

The third mode of degradation of ceramic materials in coal-fired combustion systems is via reactions with coal ash. This type of degradation depends on material composition, slag chemistry (acidic or basic), and gas-phase environment (either oxidizing or reducing). The slag generally contain phases such as SiO_2, Al_2O_3, CaO, Fe_2O_3, Na_2O, a combination of these phases, and other ash constituents depending on the coal feedstock. X-ray diffraction data for the deposits, obtained in a CERF run with combustion of Pittsburgh coal, showed the dominant phases to be mullite ($3Al_2O_3{\cdot}2SiO_2$), ordered calcian albite [(Na,Ca) Al (Si,Al)$_3O_8$], and hematite (Fe_2O_3). The melting temperatures of these phases are >1400°C (see Table 4 for a listing of melting temperatures of various compounds); reactions between these compounds and the ceramic materials occur primarily in the solid state, and little or no penetration of the ceramics occurs by liquid phase

Table 4. Melting temperatures of coal slag components

Compound	Melting Temperature (°C)
Al_2O_3	2020
SiO_2	1610-1723
Fe_2O_3	1594
CaO	2614
$Na_2O{\cdot}SiO_2$	1089
$Na_2O{\cdot}2SiO_2$	874
$Na_2O{\cdot}4SiO_2$	1112
$2Na_2O{\cdot}SiO_2$	1018
$3Al_2O_3{\cdot}2SiO_2$	1850
$Na_2O{\cdot}Al_2O_3{\cdot}2SiO_2$	1526
$Na_2O{\cdot}Al_2O_3{\cdot}4SiO_2$	1138
$Na_2O{\cdot}Al_2O_3{\cdot}6SiO_2$	1118
$Na_2O{\cdot}Fe_2O_3{\cdot}4SiO_2$	1310
$CaO{\cdot}SiO_2$	1544
$2CaO{\cdot}SiO_2$	2130
$CaO{\cdot}Al_2O_3{\cdot}2SiO_2$	1553
Na_2SO_4	884

from coal combustion environment. Similarly, X-ray diffraction data for the deposits, obtained in a CERF run with combustion of Alaskan/Russian blend coal, showed the dominant phases to be anorthite ($CaO{\cdot}Al_2O_3{\cdot}2SiO_2$), calcium aluminum silicate ($CaO{\cdot}Al_2O_3{\cdot}SiO_2$), and ordered sodium anorthite (Ca,Na)$(Al,Si)_2\ Si_2O_8$. These Ca-rich silicates also have melting temperatures >1400°C (see Table 4), and reactions between the coal ash deposit and the ceramics occur predominantly in the solid state. The experimental results also indicate that Na_2O activities in the deposits (with combustion of coals containing Fe_2O_3 and CaO) are sufficiently low to form liquid sodium silicates of various types in coal-fired systems. At present, long-term experiments are in progress in the laboratory and in CERF to evaluate the corrosion performance of several ceramic and advanced metallic materials and to assess their residual mechanical properties.

SUMMARY

Thermodynamic calculations were performed to evaluate the chemistries of gaseous and condensed phases that arise during combustion of an Illinois bituminous coal. Coal combustion results in a liquid phase that is essentially a silica-saturated silicate-sulfate condensate, with the components being largely $CaO{\cdot}SiO_2$, $Na_2O{\cdot}2SiO_2$, $FeO{\cdot}SiO_2$, $MgO{\cdot}SiO_2$, Na_2SO_4, and NaCl. At temperatures below 1180°C, the partial pressures of NaCl(g), HCl(g), NaOH(g), and Na(g) change abruptly; a complex sodium aluminosilicate, $Na_2{\cdot}Al_2O_3{\cdot}6SiO_2$(s), tends to form; and the liquid silicate-sulfate condensate disappears. Formation of the complex silicate requires intimate contacts among several gaseous and condensed phases, the probability of which is expected to be low in real systems. Under nonequilibrium conditions, where such reactions are constrained, stability of the liquid sulfate–silicate condensate extends to temperatures as low as 890°C. Calculations also indicate that the silicate phases such as mullite and calcium aluminum silicate will dominate the deposit composition and that alkali-sulfate-induced corrosion, prevalent in gas turbine systems that use coal-derived gases, may not be of concern for heat exchangers in HIPPS.

An experimental program has been initiated to evaluate materials for advanced combustion systems. Several candidate materials are being examined in a laboratory test program to assess their performance in the presence of salt and slag environments. The candidates included advanced metallic alloys, monolithic ceramics, ceramic particulate/ceramic matrix composites, ceramic fiber/ceramic matrix composites, and ceramic whisker/ceramic matrix composites. In addition, materials are being exposed in CERF at the Pittsburgh Energy Technology Center to assess their performance in a pilot-scale system that simulates combustion and flow/temperature conditions of a full-scale boiler. Extensive microstructural analyses are conducted on the exposed specimens to evaluate the corrosion performance of the materials for service in air and fireside environments of advanced coal–fired boilers.

ACKNOWLEDGMENTS

The authors thank the ceramics manufacturers for supplying specimen materials. D. L. Rink assisted in the corrosion tests and microstructural analysis of exposed specimens.

REFERENCES

1. L. A. Ruth, "Combustion 2000," PETC Review, Issue 4, p. 4, Fall 1991.

2. J. Shenker, "Development of a High-Performance Coal-Fired Power Generating System with a Pyrolysis Gas and Char-Fired High Temperature Furnace," Proc. 9th Annual Coal Preparation, Utilization, and Environmental Control Contractors' Conf., July 19-22, 1993.

3. D. J. Seery, J. J. Sangiovanni, F. L. Robson, W. M. Proscia, J. E. Holowczak, M. Bak, J. D. Freihaut, M. Heap, D. W. Pershing, and P. J. Smith, "Combustion 2000: Burning Coal in the Twenty-First Century," ibid., p. 356.

4. K. Natesan, M. Yanez-Herrero, and C. Fornasieri, "Corrosion Performance of Materials for Advanced Combustion Systems," Argonne National Laboratory Report ANL/FE-93/1, Dec. 1993.

MULLITE COATINGS FOR CORROSION PROTECTION OF SILICON CARBIDE

R. Mulpuri, and V.K. Sarin

Boston University
Department of Manufacturing Engineering
Boston, MA 02215

ABSTRACT

SiC based ceramics have been identified as the leading candidate materials for elevated temperature applications in harsh oxidation/corrosion environments. It has been established that a protective coating can be effectively used to avoid problems with excessive oxidation and hot corrosion. However, to date, no coating configuration has been developed that can satisfy the stringent requirements imposed by such applications. Chemical Vapor Deposited (CVD) mullite coatings due to their desirable properties of toughness, corrosion resistance, and a good coefficient of thermal expansion match with SiC are being investigated as a potential candidate. Since mullite has never been successfully grown via CVD, the thermodynamics and kinetics of its formation were initially established and used as a guideline in determining the initial process conditions. Process optimization was carried out using an iterative process of theoretical analysis and experimental work coupled with characterization and testing. The results of theoretical analysis and the CVD formation characteristics of mullite are presented.

INTRODUCTION

SiC and SiC based ceramics are leading candidate materials for high temperature applications due to their unique combination of high strength and thermal conductivity, low thermal expansion, high temperature stability and oxidation resistance. The presence of impurities in the environment or a gas stream can considerably increase the rate of passive oxidation by modifying the transport rate of oxygen through the protective scale, causing active oxidation via formation of SiO. This can accelerate the degradation process, and

depending on gaseous impurities produce compounds such as Na_2SiO_3 which chemically attack the ceramic resulting in accelerated corrosion. Studies have shown that substantial improvements can be made by the application of thin protective coatings. [1] It is of course imperative that these coatings be adherent, oxidation/corrosion, and thermal shock resistant in order to withstand the stringent conditions and protect the ceramic components. None of the coating configurations that have been developed so far are capable of withstanding, for extensive periods, the conditions imposed by such applications. Most coating configurations to date have failed mainly due to poor adhesion. A large mismatch in coefficient of thermal expansion (CTE) between the coating and the substrate is often a major contributing factor to this problem. Mullite ($3Al_2O_3 \cdot 2SiO_2$) is an excellent candidate for a coating material by virtue of its CTE match with SiC and its excellent high temperature stability and strength as well as oxidation and corrosion resistance characteristics.[2]

Mullite is a solid solution of Al_2O_3 and SiO_2 and is the only stable crystalline compound in the $Al_2O_3.SiO_2$ system under normal atmospheric pressure. It has a chemical composition of approximately $3Al_2O_3.2SiO_2$ (71.8 wt% Al_2O_3) and crystallizes in the orthorhombic system. [3] In spite of years of research on bulk mullite, controversy still exists regarding the solid solubility range of mullite and the exact phase diagram of the SiO_2-Al_2O_3 system. Variation in solid solubility (70 to 82% Al_2O_3) has been reported to be dependent on the method of synthesis.[4] In light of this uncertainty and the technical challenges of growing CVD mullite, two approaches were investigated; (i) Laminated structures: Formation of mullite via diffusion across multi-layers of Al_2O_3 and SiO_2, and (ii) Co-deposition: Simultaneous formation of Al_2O_3 and SiO_2 in appropriate ratios.

MULTI-LAYERED COATINGS

Multilayers of α-Al_2O_3 and vitreous SiO_2 were grown on SiC substrates by chemical vapor deposition (CVD). Equilibrium thermodynamic analysis was performed in order to establish theoretical trends and aid in determining the initial process conditions. CVD formation of individual Al_2O_3 and SiO_2 coatings is well studied. The CVD reactor was modified so that the alternating layers could be deposited using the same fixturing without interruption between layers. The thickness of the layers was adjusted such that the overall composition of the coating was that of theoretical stoichiometric mullite.

SiO_2 was deposited by pyrolysis of Tetraethoxysilane ($Si[OC_2H_5]_4$) which resulted in amorphous coatings. The deposition reaction was carried out at 800 °C and 50 torr pressure. The projected chemical reaction is as follows [5]:

$$(Si[OC_2H_5]_4) \longrightarrow \mathbf{SiO_2} + 2CO + 2CH_4 + 2C_2H_4 + 2H_2$$

Al_2O_3 was formed from $AlCl_3$ by a hydrolysis reaction. $AlCl_3$ can be formed in-situ by flowing Cl_2 or HCl with a carrier gas such as H_2 through Aluminum chips maintained at a constant temperature. H_2 and CO_2 were used to obtain the water-gas-shift reaction and form H_2O in-situ in the CVD reactor. The reaction was carried out at 950 °C and 75 torr pressure. The resulting alumina coatings had a corundum (α) structure. The chemical reactions are as follows

Source: $2Al + 3Cl_2 \longrightarrow \mathbf{2AlCl_3}$

Water-gas-shift: $CO_2 + H_2 \longrightarrow \mathbf{H_2O} + CO$

Deposition: $2AlCl_3 + 3H_2O \longrightarrow \mathbf{Al_2O_3} + 6HCl$

As deposited, the multi-layers had definite interfaces with abrupt changes in composition, which resulted in large levels of residual stresses in the coating, and in some cases crack formation. The multilayered coatings were annealed at different temperatures to facilitate the formation of mullite via interfacial reactions. Figure 1 is a TEM micrograph of an Al_2O_3-SiO_2 interface after a 2 hour anneal at 1200 °C, showing the presence of a 50 nm reaction zone. Chemical analysis of this reaction layer in the STEM using a 1 nm electron probe showed the formation of a compound in which the Al:Si atomic ratio was measured to be 65:35 (see EDS spectra in Figure 1) which is close to the theoretical ratio in stoichiometric mullite. This coating exhibited no visible signs of cracking on cooling.

In order to widen the diffusion zone, the temperature of the post deposition anneal was increased to 1350 °C. This treatment resulted in the delamination of the Al_2O_3 layer. TEM micrograph (Figure 2) of this sample shows partial transformation of the amorphous SiO_2 layer immediately next to the Al_2O_3 coating into crystalline silica. Cracks were observed at the crystalline SiO_2 layer and Al_2O_3 interface indicating that phase transformation may be responsible for coating delamination. It is felt that for any coating configuration to maintain